# Observations of Fine Scale Vertical Shear and Strain in the Upper Ocean
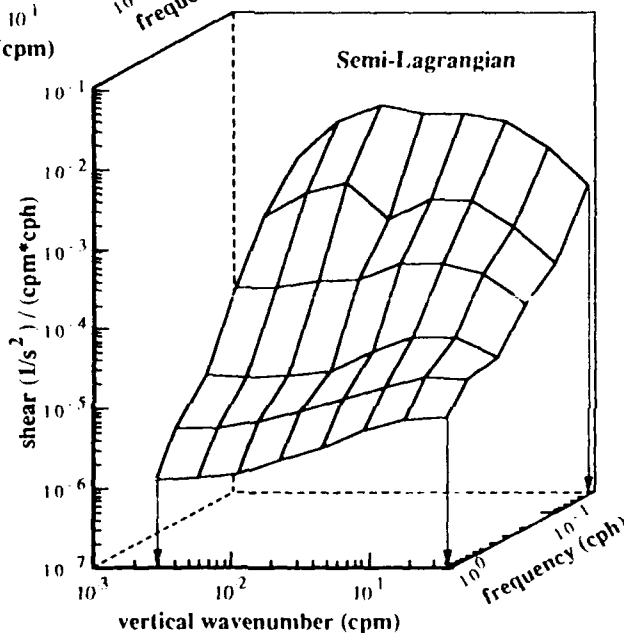
### Jeffrey T. Sherman

### SIO Reference 89-11

Eulerian



Semi-Lagrangian

**Marine Physical Laboratory**
**Scripps Institution of Oceanography**
University of California, San Diego
San Diego, California 92152

MPL-U-49/89
June 1989

89 11 21 050

# REPORT DOCUMENTATION PAGE

| 1a. REPORT SECURITY CLASSIFICATION<br>UNCLASSIFIED | | 1b. RESTRICTIVE MARKINGS | |
|---|---|---|---|
| 2a. SECURITY CLASSIFICATION AUTHORITY | | 3. DISTRIBUTION / AVAILABILITY OF REPORT<br>Approved for public release; distribution unlimited. | |
| 2b. DECLASSIFICATION / DOWNGRADING SCHEDULE | | | |
| 4. PERFORMING ORGANIZATION REPORT NUMBER(S)<br>SIO REFERENCE 89-11    [MPL-U-49/89] | | 5. MONITORING ORGANIZATION REPORT NUMBER(S) | |

| 6a. NAME OF PERFORMING ORGANIZATION<br>Marine Physical Laboratory | 6b. OFFICE SYMBOL<br>(If applicable)<br>MPL | 7a. NAME OF MONITORING ORGANIZATION<br>Office of Naval Research<br>Department of the Navy |
|---|---|---|
| 6c. ADDRESS (City, State, and ZIP Code)<br>University of California, San Diego<br>Scripps Institution of Oceanography<br>San Diego, CA  92152 | | 7b. ADDRESS (City, State, and ZIP Code)<br>800 North Quincy Street<br>Arlington, VA  22217-5000 |

| 8a. NAME OF FUNDING / SPONSORING ORGANIZATION<br>Office of Naval Research | 8b. OFFICE SYMBOL<br>(If applicable)<br>ONR | 9. PROCUREMENT INSTRUMENT IDENTIFICATION NUMBER<br>N00014-79-C-0472; N00014-87-K-0010 |
|---|---|---|

| 8c. ADDRESS (City, State, and ZIP Code)<br>Department of the Navy<br>800 North Quincy Street<br>Arlington, VA  22217-5000 | 10. SOURCE OF FUNDING NUMBERS | | | |
|---|---|---|---|---|
| | PROGRAM ELEMENT NO. | PROJECT NO. | TASK NO | WORK UNIT ACCESSION NO. |
| | | | | |

**11. TITLE (Include Security Classification)**

OBSERVATIONS OF FINE SCALE VERTICAL SHEAR AND STRAIN IN THE UPPER OCEAN

**12. PERSONAL AUTHOR(S)**
Jeffrey T. Sherman

| 13a. TYPE OF REPORT<br>sio reference | 13b. TIME COVERED<br>FROM _____ TO _____ | 14. DATE OF REPORT (Year, Month, Day)<br>June 1989 | 15. PAGE COUNT<br>124 |
|---|---|---|---|

**16. SUPPLEMENTARY NOTATION**

| 17. | COSATI CODES | | 18. SUBJECT TERMS (Continue on reverse if necessary and identify by block number) |
|---|---|---|---|
| FIELD | GROUP | SUB-GROUP | vertical strain spectrum, shear spectrum, Doppler sonar, |
| | | | |

**19. ABSTRACT (Continue on reverse if necessary and identify by block number)**

A statistical analysis of vertical shear ($pu/pz$, $pv/pz$) and vertical strain ($p\eta/pz$, $\eta \equiv$ isopycnal displacement) is performed. Data were obtained during the PATCHEX experiment (Oct., 1986), located in the eastern North Pacific (34° N, 127° W). Strain is estimated from two profiling CTD's, covering the top 560 m of the water column. The shear field is obtained using two different Doppler sonars. A pulse-to-pulse incoherent (long-range) sonar provides large-scale information (over 600 m in depth, with independent estimates every 18 m). A pulse-to-pulse coherent (short-range) sonar yields fine-scale shear structure (30 m depth coverage, with 1.5 m vertical resolution).

The design and performance characteristics of the short-range sonar is presented, including a discussion on the effects of zooplankton distribution on velocity precision.

Cross-sections in wavenumber of the vertical wavenumber-frequency ($mz,\omega$) shear spectrum exhibit a decrease in slope from $\omega^{-3}$ to $\omega^0$ as $mz$ varies from 1/512 to 1/3 cpm. Cross-sections in frequency display a band-limited behavior, which narrows with higher frequencies. All frequency bands roll off with a $mz^{-1-2}$ slope for $mz > 0.1$ cpm, with slope dependent upon noise correction scheme. The frequency-integrated shear spectrum shows agreement with the Gargett et al.(81) spectral model ($mz^0$ slope for $mz < 0.1$ cpm, $mz^{-1}$ for $mz > 0.1$ cpm).

| 20. DISTRIBUTION / AVAILABILITY OF ABSTRACT<br>☐ UNCLASSIFIED/UNLIMITED  ☒ SAME AS RPT.  ☐ DTIC USERS | 21. ABSTRACT SECURITY CLASSIFICATION<br>UNCLASSIFIED | |
|---|---|---|
| 22a. NAME OF RESPONSIBLE INDIVIDUAL<br>Robert Pinkel | 22b. TELEPHONE (Include Area Code)<br>(619) 534-2056 | 22c. OFFICE SYMBOL<br>MPL |

**DD FORM 1473, 84 MAR** — 83 APR edition may be used until exhausted.
All other editions are obsolete
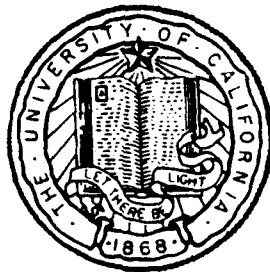
☆ U.S. Government Printing Office: 1986—607-044

The $(mz,\omega)$ vertical strain spectrum has been computed for both Eulerian (fixed-depth) and semi-Lagrangian (isopycnal-following) reference frames. The Eulerian strain spectral shape is reminiscent of the measured shear spectrum. However, the semi-Lagrangian strain spectrum displays an $\omega^{-2-1}$ frequency dependency at high wavenumbers (instead of $\omega^0$). The interpretation is that the Eulerian spectrum at high wavenumbers has been contaminated due to vertical advection causing Doppler-shifting of the true signal.

A semi-Lagrangian shear spectrum is estimated by using linear internal wave theory and the measured semi-Lagrangian strain spectrum. The resulting shape has $\omega^{-2-1}$ slope for all $mz$. The frequency dependence of the high-wavenumber spectral rolloff appears to be proportional to $\omega^{1/2}$. The Eulerian high-wavenumber, near-inertial shear variance contributes only 10% of the total variance, while the semi-Lagrangian spectrum shows half of the high-wavenumber variance originating from near-inertial motions.

# Observations of Fine Scale Vertical Shear and Strain in the Upper Ocean

Jeffrey T. Sherman

## SIO Reference 89-11

**Marine Physical Laboratory**
**Scripps Institution of Oceanography**
University of California, San Diego
San Diego, California 92152

# Table of Contents

# List of Figures and Tables

## Appendix A

## Appendix C

## Appendix D

# ACKNOWLEDGMENTS

I would like to express my gratitude to Dr. Robert Pinkel for allowing me to play a major role in the development of the coherent sonar. Also, his support and guidance on the scientific analysis of the data set have made a major contribution to the quality of this thesis.

I would like to thank the members of my committee, who have provided many useful comments and advice.

I had the pleasure of developing the coherent sonar with three highly-qualified engineers: Mike Goldin, Lloyd Green, and Eric Slater. I not only learned a tremendous amount from these three, but had a very enjoyable, although sometimes a bit hectic, time in the process. Steve Beck provided many useful services, including managing the computer system used for analyzing the data.

The development of the coherent sonar has necessitated several cruises on the research platform FLIP, which was always professionally operated by Dewitt Efird and crew.

Many fellow students have provided stimulating discussion and encouragement during the course of this work. I would like to especially thank Al Plueddemann and Robin Williams, who gave me support during my earlier years at Scripps.

I would like to thank Dr. Eric D'Asaro for various suggestions, including the idea that vertical advection might lead to a false sense of rotation of an inertial wave.

Jo Griffith assisted with the illustrations, and gave much-needed advice on preparation of figures.

# ABSTRACT OF THE DISSERTATION

Observations of Fine-Scale Vertical Shear and Strain in the Upper Ocean

by

Jeffrey Thomas Sherman
Doctor of Philosophy in Oceanography
University of California, San Diego, 1989
Professor Robert Pinkel, Chairman

A statistical analysis of vertical shear ($\partial u/\partial z$, $\partial v/\partial z$) and vertical strain ($\partial \eta/\partial z$, $\eta \equiv$ isopycnal displacement) is performed. Data were obtained during the PATCHEX experiment (Oct., 1986), located in the eastern North Pacific ($34°$ N, $127°$ W). Strain is estimated from two profiling CTD's, covering the top 560 m of the water column. The shear field is obtained using two different Doppler sonars. A pulse-to-pulse incoherent (long-range) sonar provides large-scale information (over 600 m in depth, with independent estimates every 18 m). A pulse-to-pulse coherent (short-range) sonar yields fine-scale shear structure (30 m depth coverage, with 1.5 m vertical resolution).

The design and performance characteristics of the short-range sonar is presented, including a discussion on the effects of zooplankton distribution on velocity precision.

Cross-sections in wavenumber of the vertical wavenumber-frequency ($m,\omega$) shear spectrum exhibit a decrease in slope from $\omega^{-3}$ to $\omega^0$ as $m$ varies from 1/512 to 1/3 cpm. Cross-sections in frequency display a band-limited behavior, which narrows with higher frequencies. All frequency bands roll off with a $m^{-1-2}$ slope for $m>0.1$ cpm, with slope dependent upon noise correction scheme. The frequency-integrated shear spectrum shows agreement with the Gargett et al.(81) spectral model ($m^0$ slope for $m<0.1$ cpm, $m^{-1}$ for $m>0.1$ cpm).

The ($m,\omega$) vertical strain spectrum has been computed for both Eulerian (fixed-depth) and semi-Lagrangian (isopycnal-following) reference frames. The Eulerian strain spectral shape is reminiscent of the measured shear spectrum. However, the semi-Lagrangian strain spectrum displays an $\omega^{-2-1}$ frequency dependency at high wavenumbers (instead of $\omega^0$). The interpretation is that the Eulerian spectrum at high wavenumbers has been contaminated due to vertical advection causing Doppler-shifting of the true signal.

A semi-Lagrangian shear spectrum is estimated by using linear internal wave theory and the measured semi-Lagrangian strain spectrum. The resulting shape has $\omega^{-2-1}$ slope for all $m$. The frequency dependence of the high-wavenumber spectral rolloff appears to be proportional to $\omega^{\nmid}$. The Eulerian high-wavenumber, near-inertial shear variance contributes only 10% of the total variance, while the semi-Lagrangian spectrum shows half of the high-wavenumber variance originating from near-inertial motions.

# CHAPTER I

## Synopsis

### 1.1 Introduction

This thesis addresses the vertical wavenumber-frequency $(m,\omega)$ distribution of vertical shear and strain in the upper ocean. Part of the data set includes measurements from a newly-developed pulse-to-pulse coherent sonar. Chapter 2 discusses its design and performance. Chapter 3 investigates the effects of zooplankton distribution on Doppler sonars which use small ensonified volumes. A secondary data set of isopycnal vertical displacement $(\eta)$ was collected with a profiling CTD system. Vertical shear $(\partial u/\partial z, \partial v/\partial z)$ and vertical strain $(\partial \eta/\partial z)$ data are analyzed in Chapter 4.

### 1.2 Motivation

The fine-scale oceanic shear is thought to be a key link in the process of energy dissipation in the internal wave field, and a contributor to microscale mixing in the sea. Yet, little is known about the space-time variability of the shear. What frequencies play an important role at high wavenumbers, and thus determine the temporal characteristics of low Richardson number $(\equiv Ri)$ events? How does the frequency distribution change from low wavenumbers, where motions are considered to behave as linear internal waves, to high wavenumbers, where strong non-linearities are expected? In the past, mod⟨'ers have used the Garrett-Munk (GM) spectrum to estimate statistics of mixing events (i.e. Desaubies and Smith(82)). The GM model is based upon a variety of one-dimensional spectral measurements, which are pieced together by assuming that the spectrum is separable: all frequencies share the same wavenumber dependence. Is this a reasonable assumption?

Partial information on vertical shear distribution has been available from the Gargett et al.(81) spectral model (Fig. 1.1). They hypothesize an $m^0$ slope at low wavenumbers, with a depth-independent rolloff to a $m^{-1}$ slope at $m_c \approx 0.1$ cpm. Following the work of Munk(81), Gargett et al. suggest that the rolloff occurs when the Inverse Richardson Function (IRF) reaches a value of 1, where

$$IRF(m) = \frac{1}{N^2} \int_0^m \phi(m)dm,$$

N is the Vaisala frequency, and $\phi(m)$ is the shear vertical wavenumber spectrum. Based on the energy level of the GM model, Munk(81) predicts $IRF(m_c) = 0.5$.

The Gargett et al. model is based on measurements from slow-profiling instruments. No sense of the time evolution of the fine scale shear was obtained. The GM spectrum (i.e. Munk(81)) assumes that the wavenumber spectral shape is independent of frequency. All frequency components of the shear spectrum should replicate the Gargett et al. model. However, the only published measurement of $(\omega,m)$ shear spectrum (Pinkel(85), Fig. 1.2) shows that the wavenumber spectral shape depends strongly on frequency, out to wavenumbers of 0.03 cpm. Should modelers use the Garrett-Munk or Pinkel spectrum? If the Pinkel spectrum is really

correct, what happens in frequency at the $m_c$ rolloff? Is $m_c$ really determined by $IRF(m_c) = 1$?

## 1.3 Experimental Approach

During the PATCHEX experiment in October, 1986 (located at 34° N, 127° W), a seven day data set was collected from a long-range pulse-to-pulse incoherent Doppler sonar, and a short-range pulse-to-pulse coherent Doppler sonar. The combined measurements allow a statistical analysis of the shear field from 3-600 m vertical scales. The calculated $(\omega, m)$ spectrum is shown in Fig. 1.3a. No WKB scaling has been applied (although Ch. 4 does explore the effects of various WKB-scaling). Spectral levels from the long-range sonar have been adjusted downwards by 40% to provide the most optimal fit with the short-range sonar spectrum (also discussed in Ch. 4). The spectral shape that emerges is very reminiscent of Pinkel's spectrum in Fig. 1.2. It is now seen that there is a slight shift of $m_c$ to higher wavenumbers with higher frequency bands. High frequencies appear more band-limited in nature. All frequency bands converge to the same energy level at high wavenumbers, such that high wavenumber motions appear 'white' in frequency. Poor agreement is seen with the GM spectrum. The GM assumption of separability appears to be strongly violated. However, when the PATCHEX wavenumber spectrum is integrated over all frequencies (Fig. 1.3d), good agreement is seen with the Gargett et al. model.

The above shear spectrum is based on Eulerian (fixed-depth) measurements. This is 'contaminated' in the frequency domain due to vertical advection (by the internal wave field itself), causing a fixed-depth sensor to see a Doppler-shifted frequency of the true signal. What would the 'uncontaminated' spectrum look like? During PATCHEX, two rapid-profiling CTDs (three-minute cycling period) were operational over a three week period (over 20,000 profiles recorded), giving density information down to 560 m depth. The measurement technique only allows the vertical strain component of vertical displacement to be resolved $(\partial \eta / \partial z)$. Vertical strain can be measured in two different reference frames: Eulerian (for comparison to the shear data) and semi-Lagrangian, where strain is measured while following isopycnals (removing the effect of vertical advection).

The $(\omega, m)$ spectra for both the Eulerian and semi-Lagrangian vertical strain are shown in Figs. 1.4 and 1.5. The Eulerian strain spectrum is similar to the shear spectrum: a shift of $m_c$ with frequency, a narrowing of the wavenumber bandwidth at higher frequencies, and all frequencies converging to the same spectral level at high wavenumber. The cumulative strain spectrum also looks very similar.

The semi-Lagrangian vertical strain spectrum has quite different characteristics. The frequency spectrum appears red in nature at high wavenumbers. The rolloff wavenumber $m_c$ occurs at even higher values, with the highest frequency band not yet rolling off at the 0.3 cpm resolution. However, when the semi-Lagrangian spectrum is integrated across frequencies, the resulting cumulative spectrum is similar to the Eulerian version. The implication is that the 'red' frequency distribution seen in the semi-Lagrangian spectrum at high wavenumbers has been Doppler-shifted across all frequencies in the Eulerian spectrum, resulting in a 'white' frequency distribution.

By comparing the Eulerian shear and strain fields, what can be said about the nature of these motions, and the possible effect of vertical advection? Linear internal wave theory leads to a frequency-dependent relation between the vertical strain/shear variance ratio:

$$\frac{N^2 \eta_z^2}{U_z^2} = \frac{(\omega^2 - f^2)}{(\omega^2 + f^2)} \frac{N^2}{(N^2 - \omega^2)} ,$$

where f = Coriolis frequency, and $U_z^2 = (\partial u/\partial z)^2 + (\partial v/\partial z)^2$. Near-inertial waves have low strain-to-shear variance, while near-N frequencies have high strain-to-shear values. Comparison of linear theory to the measured ratio (Fig. 1.6) shows fair agreement at low wavenumbers ($m < .01$ cpm). The inertial band shows slightly too much strain at all wavenumbers, perhaps indicating high-strain, high-frequency waves Doppler-shifted to near-inertial encounter frequencies. All other frequency bands exhibit too much shear variance at high wavenumbers to agree with linear theory. This could either indicate near-inertial waves (high-shear, low-strain) which have been Doppler-shifted to higher frequencies, and/or nonlinearities taking over at higher wavenumbers.

If, as suggested by comparison of semi-Lagrangian and Eulerian vertical strain spectra, the Eulerian shear is contaminated in frequency at high wavenumbers, how would the semi-Lagrangian shear appear? One approach is to assume that the linear strain/shear variance ratio is valid (even though nonlinearities are expected at high wavenumbers). The semi-Lagrangian shear spectrum can be estimated by simply dividing the strain spectrum by the linear ratio. Since vertical strain approaches zero at near-inertial frequencies, and thus is prone to contamination from Doppler-shifted, higher frequency motions, the estimated shear may also suffer contamination in the near-inertial band. The resulting spectrum (Fig. 1.7a) is very similar to the semi-Lagrangian strain spectrum. When viewed in the frequency domain (Fig. 1.7b), it is seen that most of the wavenumber bands exhibit an $\omega^{-2}$ slope in frequency, with only the highest wavenumber band (1/4-1/2 cpm) showing disagreement. The rolloff wavenumber ($m_c$) appears to be proportional to $\omega^{\frac{1}{2}}$.

What are the overall implications of the Eulerian and semi-Lagrangian shear spectra to the temporal scales of low Ri events? The Inverse Richardson Function, now also a function of $\omega$ (as in Pinkel(85)), was computed from both viewpoints, and is shown in Fig. 1.8. The Eulerian IRF estimates most of the high wavenumber variance resulting from high frequency motions, with near-inertial, high wavenumber waves contributing little to the overall variance. In comparison, the semi-Lagrangian IRF predicts that half of the shear variance comes from near-inertial motions. The implication is that measurements from a fixed-depth sensor would estimate that high-frequency motions provide most of the shear at high wavenumbers, such that the near-inertial field would appear to have little influence on causing instabilities. However, a sensor following an isopycnal would see half of the total shear variance resulting from near-inertial motions, and so indicate near-inertial waves playing an important role in low Ri events.

1.4

## Conclusions

Vertical strain frequency-wavenumber spectra suggest that the Eulerian (fixed-depth) reference frame has been contaminated in frequency due to vertical advection of fine-scale strain, caused by the internal wave field. This effect is strongest at high wavenumbers.

The Garrett-Munk spectrum is an inappropriate description of the oceanic shear and strain fields when viewed from an Eulerian reference frame. However,

the semi-Lagrangian (isopycnal-following) measurements show much better agreement with the GM model. The high wavenumber rolloff ($m_c$) is frequency-dependent, appearing to be proportional to $\omega^{\frac{1}{2}}$.

The Gargett et al.(81) wavenumber spectral model is an appropriate description of the PATCHEX data set. The measured $m_c$ value (1/16 cpm) is slightly lower than their 0.1 cpm. Additionally, a low-wavenumber rolloff should perhaps also be included, suggesting a spectral shape which is band-limited between $m = 0.01$-$0.1$ cpm. Gargett et al. suggest IRF($m_c$) = 1, while the PATCHEX data set has IRF($m_c$) $\approx$ 0.3. This is in closer agreement with Munk's(81) value of IRF($m_c$) = 0.5.

The interpretation of the Inverse Richardson Function is quite different for the two frames of reference. The Eulerian IRF suggests that high-frequency motions are responsible for low Ri events, while the semi-Lagrangian IRF has near-inertial waves contributing half of the overall variance. The semi-Lagrangian spectrum is most probably closer to the truth, and thus Desaubies and Smith's(82) analysis of K-H instabilities, which used the GM spectral model, is still a valid description.

Ideas for the future include measuring shear from an isopycnal-following reference frame for intercomparison with the semi-Lagrangian strain. For instance, when does the semi-Lagrangian strain/shear ratio begin to differ with linear theory? Are high wavenumber waves best dynamically described in a Lagrangian frame? What does the GM spectrum (in a Lagrangian reference frame) look like to an Eulerian observer? The issue of why the shear spectrum rolls off at high wavenumbers remains unresolved.
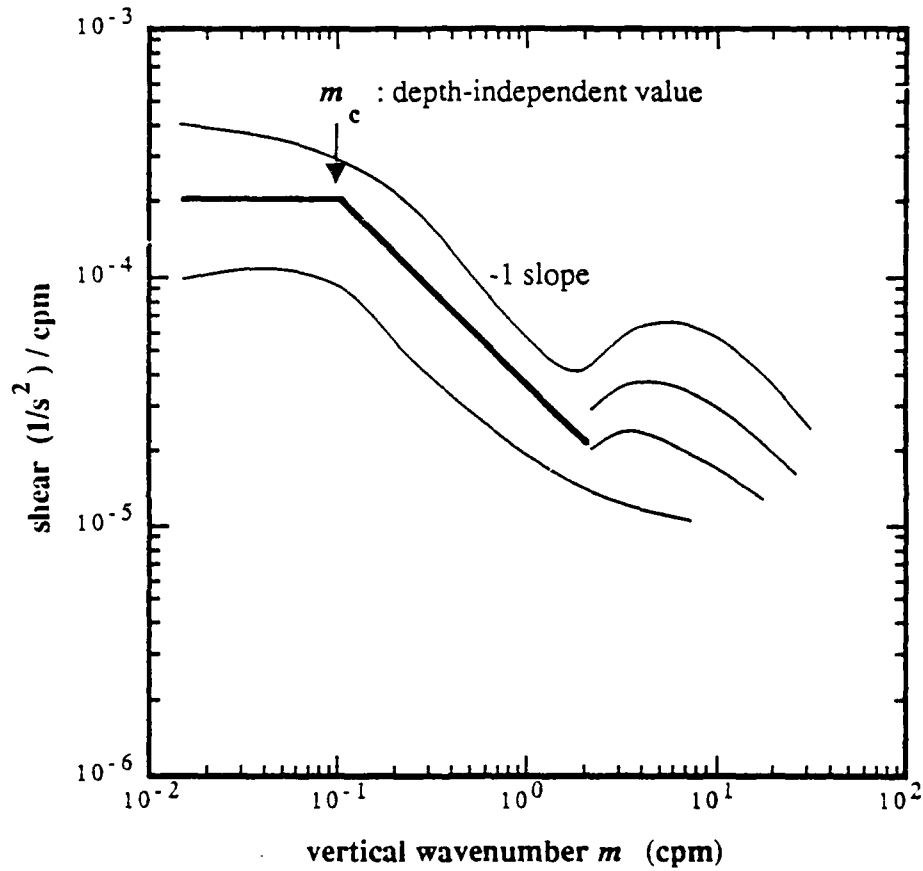
**Figure 1.1.** Gargett et al.(81) based a universal shear spectral model on measurements from the FAME experiment. The $m^0$ slope at low wavenumbers has its energy level scale in a WKB fashion as $N^2$. The break in slope at $m_c \approx 0.1$ cpm is thought to be a depth-independent parameter occurring when IRF($m_c$) ～ 1. The $m^{-1}$ slope is then followed by an intermittent high-wavenumber region, dependent upon mixing events.
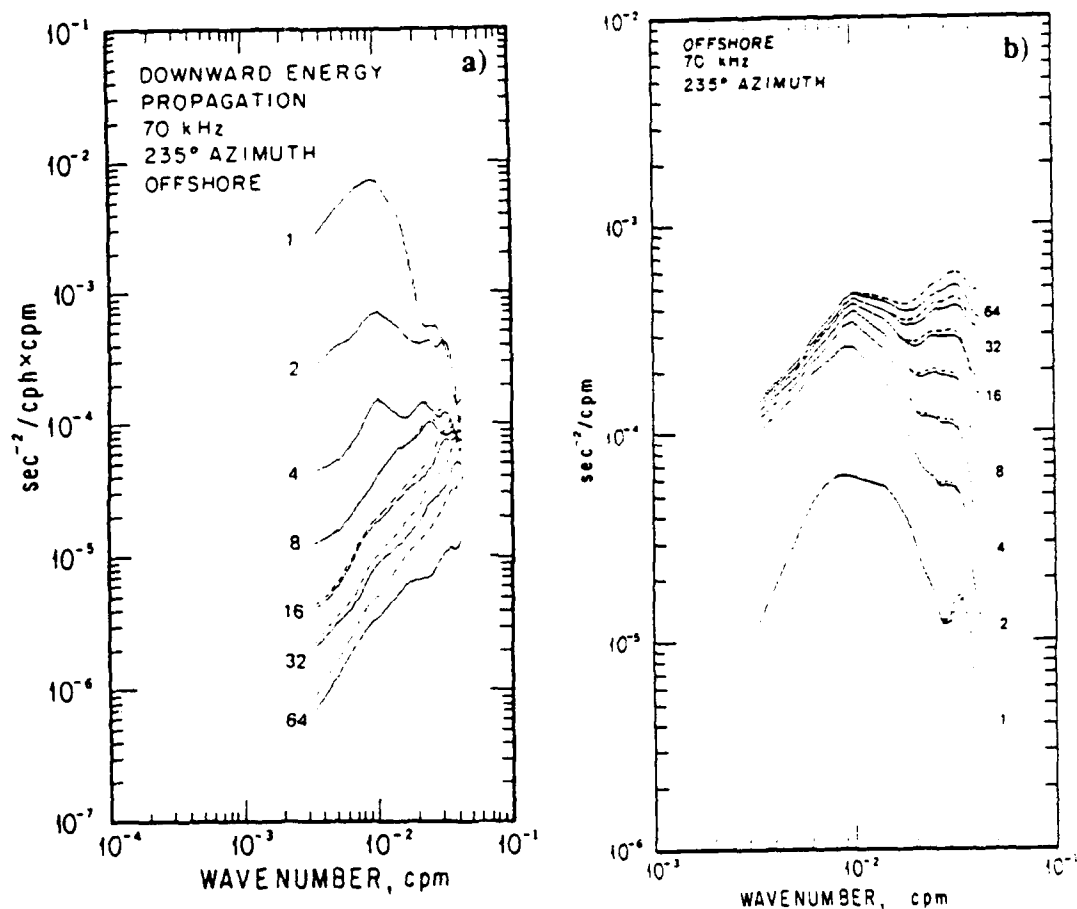
**Figure 1.2.** a) Cross-sections of the $(m,\omega)$ vertical shear spectrum is shown for 1, 2, 4, 8, 16, 32, and 64 cpd, as calculated by Pinkel(85). Dashed lines are the measured values, while the solid lines represent estimates after modeled instrument noise has been removed. b) When the $(m,\omega)$ spectrum is integrated in frequency, the cumulative shear spectrum is obtained. Each line represents the shear variance integrated from 0.5 cpd up to the labeled value (i.e. 0.5-1.0 cpd). The resulting spectral shape ($m^0$ slope for $m>0.01$ cpm) is in agreement with the Gargett et al.(81) model.
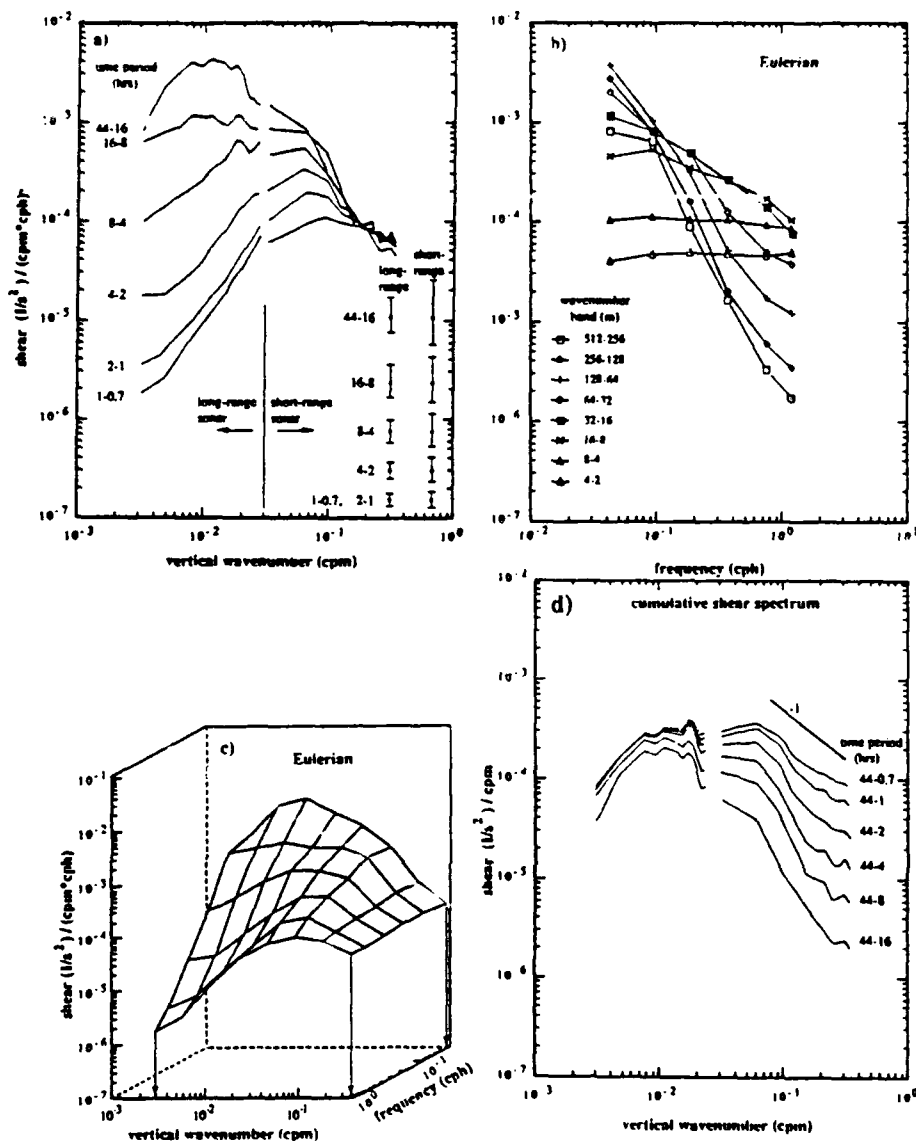
**Figure 1.3.** a) The PATCHEX composite ($m,\omega$) shear spectrum includes both the long-range and short-range sonar estimates. Average spectral density levels are shown for six bands : 44-16, 16-8, 8-4, 4-2, 2-1, and 1-0.7 hour periods. a) Cross-sections of the ($m,\omega$) shear spectrum are displayed for both sonars. The long-range sonar's spectral levels have been reduced by 40% to provide the optimum fit to the short-range sonar spectrum. b) The same spectrum is now viewed in frequency, with cross-sections displayed for 8 different wavenumber bands (as labeled). Each line represents the average spectral density for its wavenumber band. c) Figs. a) and b) are combined in a three-dimensional view of the ($m,\omega$) shear spectrum. d) Integration of energy across frequency bands yields a cumulative vertical-wavenumber spectrum, with the top curve representing total energy contained between 0.7-44 hour time periods.
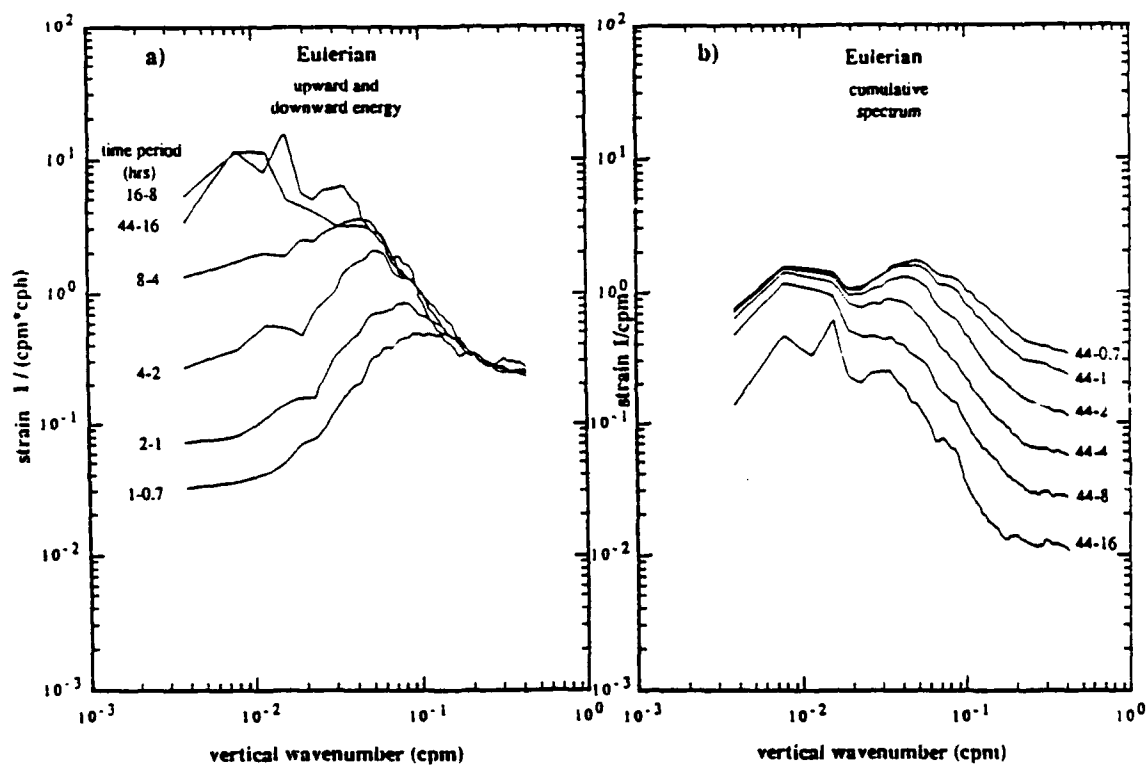
**Figure 1.4.** a) The PATCHEX Eulerian vertical strain $(m,\omega)$ spectrum is displayed in six different frequency bands, as in Fig. 1.3a. Spectral estimates have been logarithmically-smoothed in m, with a bandwidth equal to $\delta m = \pm 0.1m$. b) The cumulative strain spectrum's 44-0.7 hour band is very similar to the the shear cumulative spectral value in Fig. 1.3d.
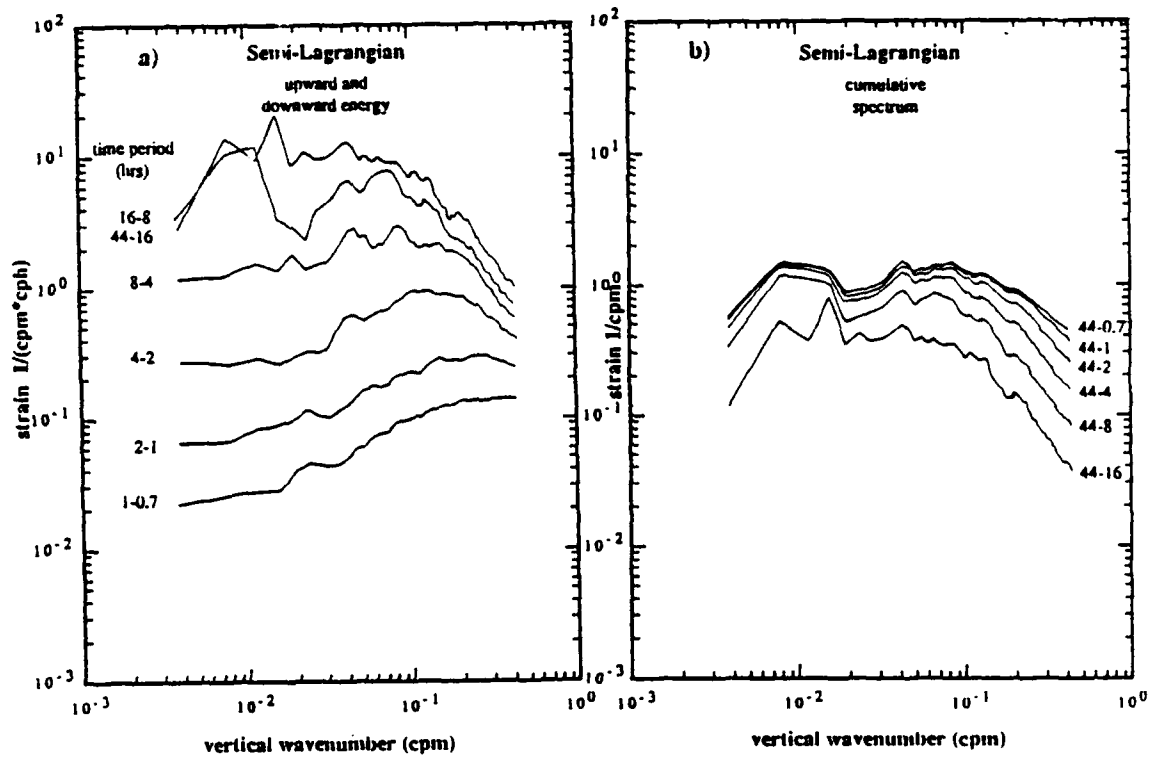
**Figure 1.5.** The PATCHEX semi-Lagrangian vertical strain ($m,\omega$) spectrum is shown in the same format as Fig. 1.4. Although the semi-Lagrangian spectrum in a) looks quite different from the Eulerian strain spectrum in 1.4a, the semi-Lagrangian cumulative spectrum's 44-0.7 hour band (b) is now very similar to the Eulerian's (Fig. 1.4b).
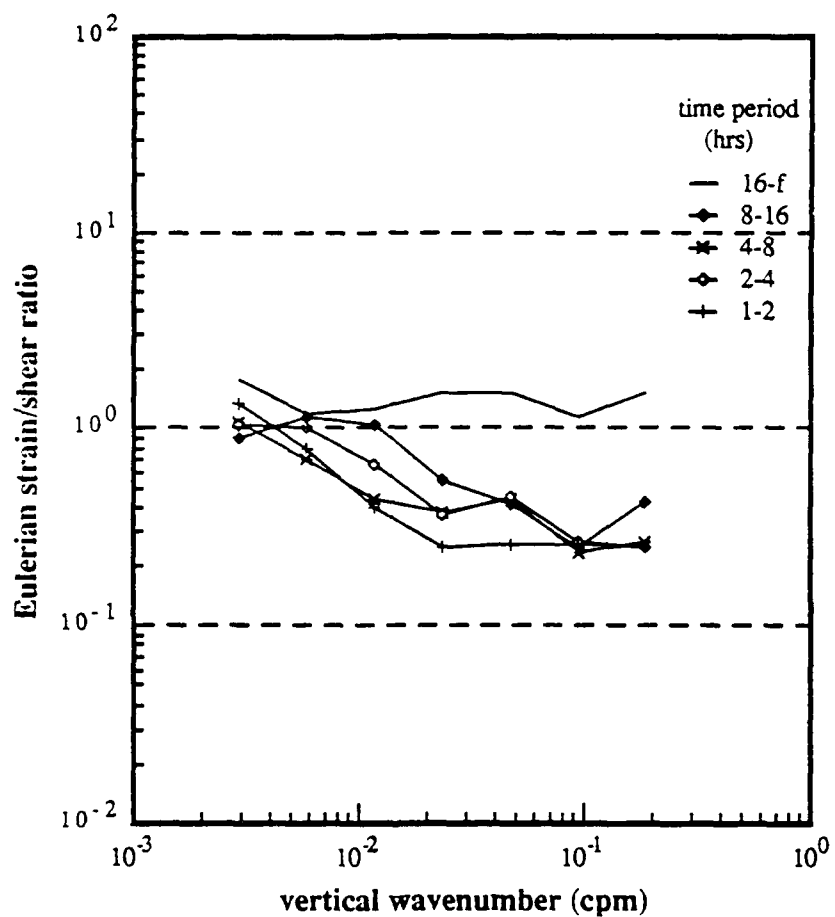
**Figure 1.6.** The measured ratio of vertical strain/shear variance is divided by the ratio predicted by linear theory. A value of 1 means perfect agreement, >1 too much strain, <1 too little strain to agree with linear theory. Estimates are averaged in wavenumber to provide better precision.
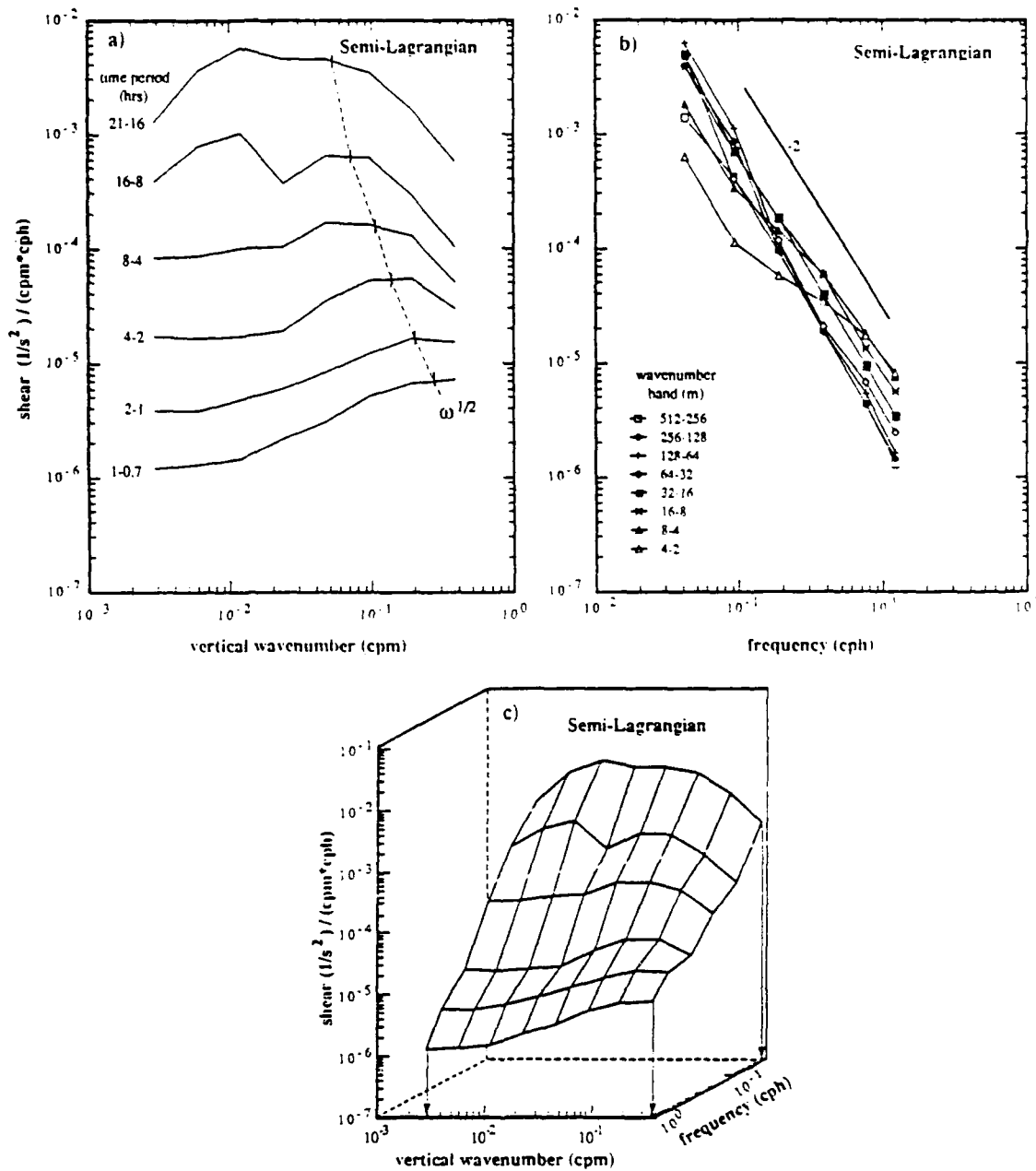
**Figure 1.7.** A semi-Lagrangian vertical shear spectrum is estimated from the semi-Lagrangian strain spectrum, assuming that linear internal wave theory provides the correct strain/shear variance ratio. Spectral densities are averaged into eight different wavenumber bands. a) The high-wavenumber rolloff ($m_c$) appears to increase as a function of $\omega^{1/2}$. b) When viewed in frequency space, all except the highest wavenumber band exhibit an $\omega^{-2}$ slope. c) The ($m,\omega$) spectrum is plotted in a three-dimensional format.
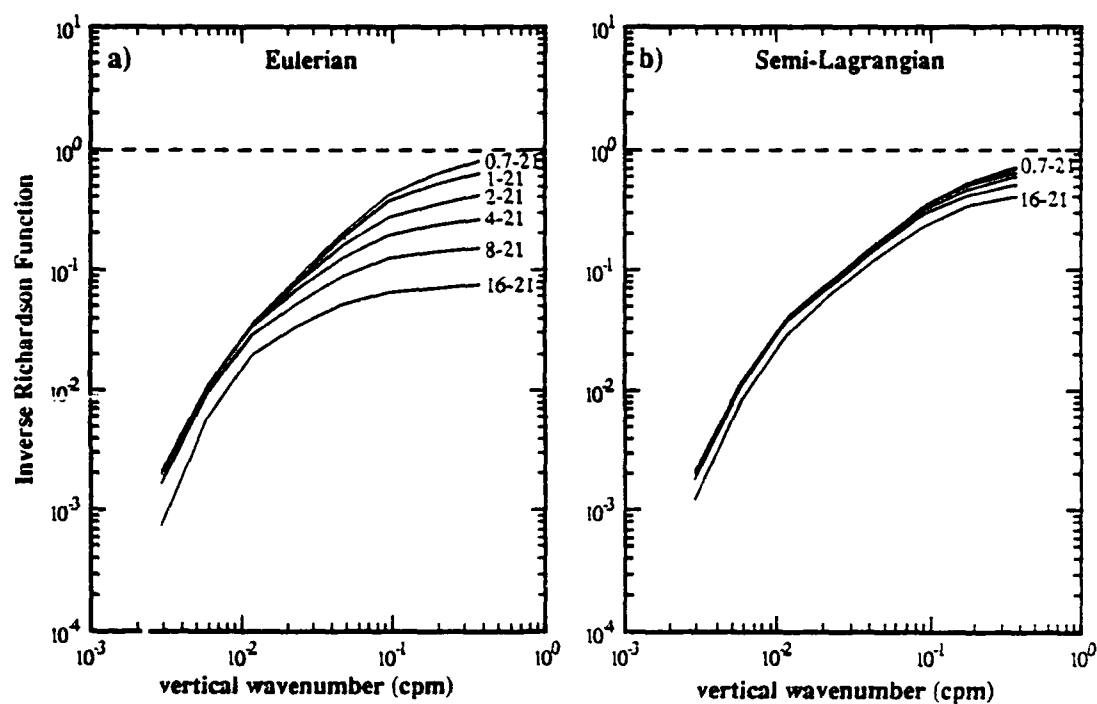
**Figure 1.8.** Estimates are shown of the Inverse Richardson Function. a) is based on the Eulerian shear spectrum. b) is derived from the semi-Lagrangian spectrum (Fig. 1.7). The semi-Lagrangian shows the near-inertial band contributing nearly half of the total variance, whereas the Eulerian estimates the near-inertial band providing 10% of the overall variance.

## CHAPTER II


### Considerations in the Design of a Coherent Sonar


### 2.1    Introduction

Remote-sensing Doppler sonars have been developed over the past decade to produce vertical profiles of the oceanic velocity field (c.f. Pinkel(79), Woodward and Appell(86)). Pulse-to-pulse incoherent processing (Fig. 2.1a) has typically been implemented. Its precision ($\equiv \sigma_{inc}$) in a noise-free environment is defined by (Theriault(86)):

$$\sigma_{inc}(\text{cm/s}) = c/(4\pi f_o \tau M^{\frac{1}{2}}) \qquad (2.1)$$

where c = speed of sound (cm/s), $f_o$ = transmission frequency (Hz), $\tau$ = pulse duration (sec), and M = number of independent estimates averaged together. Precision can be increased by transmitting a higher frequency (which lowers maximum range due to attenuation losses), using a longer pulse (which gives less spatial resolution), or averaging more estimates (which lowers the temporal resolution).

Another Doppler technique is pulse-to-pulse coherent processing (Fig. 2.1b). Transmission pulses are phase-locked to each other, and the Doppler-shift at a specific range is estimated from the variation in phase return from one pulse to the next. Pinkel(80) and Lhermitte(81,83) give excellent descriptions of the coherent process. A coherent sonar's precision is not dependent upon the transmission pulse duration (at least to first order). This allows coherent processing to achieve greater spatial resolution for the same amount of velocity precision as an incoherent system, at the expense of giving up maximum range capability.

This chapter constructs a coherent sonar model applicable to the open ocean, such that estimates of velocity precision can be made. The model's prediction is compared with measurements taken from a coherent system built at Marine Physical Laboratory (MPL) at Scripp's Institution of Oceanography. The trade-offs between a coherent and incoherent sonar are discussed.


### 2.2    System Parameters of a Coherent Sonar

Each sonar system has its own set of characteristics (i.e. transmission frequency, type of deployment, beam angles, etc.) which determines its maximum range, spatial resolution, and velocity precision. Parameters defining a coherent Doppler sonar system are:

> $f_o$ = carrier frequency of the transmitted pulse
> $\lambda$ = wavelength of transmitted pulse ($\lambda = c/f_o$)
> $\tau$ = duration time of the transmitted pulse
> $\Delta$ = time between pulses
> $\phi$ = angle of sonar with respect to azimuth
> $\theta$ = full-width angle of sonar's main lobe
> $\psi$ = solid angle of sonar's main lobe
> $E_b$ = ratio of energy received from main beam versus all other sources (acoustic cross-talk level).

These parameters specify the following system constraints:

$$V_{max} = \lambda/4\Delta = c/4f_o\Delta \text{ - Nyquist velocity}$$
$$R_{max} = c\Delta/2 \text{ - maximum range achieved}$$
$$V_{max}R_{max} = c\lambda/8 \text{ - limitation parameter for given frequency}$$
$$V_{avg} = (c\tau/2)(\theta R_{max}/2)^2 \text{ - average ensonified volume size}$$

The maximum range required for an application sets the value of $\Delta$. Given the expected range of velocities, $f_o$ can be chosen to avoid velocity aliasing. The pulse duration and beam angle determine the spatial resolution. Velocity precision depends upon both environmental conditions and sonar system limitations.

Noise enters the system through the receive system electronics, and by contamination of the receive signal from range-aliased signals and side-lobe interference (Section 2.3).

Environmental conditions increase velocity variance due to: true water motion variance ($\equiv \sigma_w^2$), biota actively swimming ($\equiv \sigma_b^2$), and sonar instrument motion ($\equiv \sigma_I^2$). The number of scatterers present and their size distribution will also affect spatial resolution (Chapter 3).

The performance of the system depends upon the algorithm employed to produce the velocity estimates. Choices include the Rummler autocovariance estimator (Rummler(68)), the first moment of a spectral estimate, or some variation. Sirmans and Bumgarner(75) and Lhermitte and Serafin(84) discuss processing technique tradeoffs in their papers.

## 2.3    Acoustical Interference : Range-Aliasing and Cross-Talk

The ideal receive signal is comprised entirely of scattering from the desired ensonified volume. However, two other sources are also received: acoustic cross-talk, and range-aliasing (shown schematically in Fig. 2.2).

Acoustic cross-talk includes returned side lobe energy from the sonar transmission beam, and, in a multi-beam environment, energy leakage into side lobes from other beams. Since pure volume reverberation has a low backscattering strength compared to a reflective surface(i.e. ocean bottom, surface, ship, or mooring cable will appear on order 60-80 dB brighter per unit solid angle (Urick(83))) a side lobe return can dominate the main beam under poor circumstances.

Total energy received can be estimated for pure volume reverberation by integrating the sonar's beam pattern over the complete hemisphere (solid angle = $4\pi$). This energy can be compared to that received in just the main lobe to estimate $E_b$:

$$E_b = \frac{\int\int^{\psi} b(\theta,\phi) \, d\theta \, d\phi}{\int_{4\pi-\psi} \int b(\theta,\phi) \, d\theta \, d\phi} \tag{2.2}$$

where $b(\theta,\phi)$ is the beam pattern (c.f. Urick). A narrower main lobe means a smaller $\psi$, and requires lower side lobe levels to maintain a constant $E_b$. Cross-talk from a multi-beam system can also be estimated from beam pattern geometry in a similar fashion. Once a system is built, field testing by passively listening on one beam while transmitting on all others gives an empirical estimate of multi-beam cross-talk levels.

Range aliasing is caused by previous pulses scattering further out in range, and arriving at the receiver at the same time as the desired ensonified volume. The energy in the return signal from a single transmission pulse can be modeled as:

$$E(r) = \frac{E_o \sigma}{r^2} 10^{-2\alpha r} \qquad (2.3)$$

where $E_o$ is the energy of the transmitted pulse, $\sigma$ is the fraction of energy actually backscattered toward the receiver, $\alpha$ = absorption loss per meter, and $r$ = distance(range) along the beam. The $r^2$ factor represents attenuation due to spherical spreading of the backscattered signal. (2.3) neglects near-field sonar effects, which lowers $E(r)$ at close range. This includes parallax problems for a split transmit/receive system, and attenuation in the Fresnel zone. The Fresnel zone is where the scattered return is close enough to the transducer such that a plane wave front is not a good approximation. The curvature of the return signal results in phase cancellation across the sonar face, causing attenuation of the signal. (2.3) also assumes a pure volume reverberation return (no reflective surfaces at far range), and no intensity variability from zooplankton patchiness. $E(r)$ is shown in Fig. 2.3a, along with an hour-long afternoon profile measured from the MPL sonar. Electronic noise has been added to the simulated profile to better match intensity at far range. Discrepancies are due to (2.3) not modeling the near-field, and to scattering layers of biota increasing the intensity at midrange depths. Fig. 2.3b is from Plueddemann(87) as measured from a 75 kHz system, and shows the degree of day/night temporal variability.

A coherent sonar runs into problems by transmitting again every $\Delta$ seconds (when $r$ = $R_{max}$). The total signal received is:

$$E_T(r) = E(r) + E(r+R_{max}) + E(r+2R_{max}) + \cdots \qquad (2.4)$$

The range-aliased intensity profile based on $\Delta$ = 60 ms is shown in Fig. 2.3c for both the simulated and hour-long average measured profile in Fig. 2.3a. Also shown is the 7.5 day average profile for the MPL coherent sonar from the PATCHEX cruise. Again, discrepancies at near range are from not modeling near-field effects.

A signal-to-noise ratio (SNR) for range aliasing can be defined as:

$$SNR_{ra}(r) = \frac{E(r)}{\sum_{j=1}^{\infty} E(r + jR_{max})} . \qquad (2.5)$$

$SNR_{ra}$ is shown in Fig. 2.3d for both the hour-long measured and simulated profiles for $\Delta$ = 60 ms. The lower intensity response in the near field of the sonars translates into 4-8 dB lower $SNR_{ra}$ from the simulation. Also affecting the measured estimates is the scattering layer at midranges. When this layer moves up at night, near range intensities increase while far ranges decrease. This steepens the slope of the intensity profile, causing $SNR_{ra}$ to increase.

To improve $SNR_{ra}$, frequency can be increased (causing more attenuation in range), or $R_{max}$ ($\Delta$) can be made greater (so that the aliased signal is further out in range, and smaller in amplitude). $SNR_{ra}$ at $r$ = $R_{max}$ is estimated from the simulated profile for both varying frequency and $\Delta$ in Fig. 2.3e and f. Although increasing

either $\Delta$ or $f_o$ improves $SNR_{ra}$, it also decreases $V_{max}$, causing more velocity aliasing problems. The signal will also decorrelate faster, adding more variance to the velocity estimate.

Another approach to increase $SNR_{ra}$ is to focus the transmit and receive transducers such that only the volume of interest is mutually shared by the two beams (bi-static configuration). Cross-talk SNR is then limited only by side lobe contamination levels. More elaborate techniques involving coded pulses are also discussed in Brumley et al.(87) and Cabrera et al.(87).

Correct modeling of the effect of range aliasing on the velocity estimate is unclear. The Doppler spectrum from a measured range bin is the sum of the true range bin spectrum plus the spectra from all other aliased bins, weighted by their respective intensities. Velocity precision will depend upon the summed spectral shape, plus the velocity estimator used. For instance, a first-moment spectral estimator would predict an aliased velocity $\equiv \hat{V}(r)$ to be:

$$\hat{V}(r) = \frac{E(r)V(r) + E(r+R_{max})V(r+R_{max}) + \cdots}{E(r) + E(r+R_{max}) + \cdots}$$

where $V(r)$ is the actual velocity field. Let $V(r)$ be Fourier-decomposed into slant range wavenumber(k) components:

$$V(r) = \sum_k V_o(k)e^{i(kr+\theta(k))}$$

where $\theta(k)$ is the phase of the wave(k) at $r=0$. The vertical wavenumber $m$ is related to k by $m = k/\sin(\phi)$. The range-aliased response for wavenumber k is:

$$\hat{V}(r,k) = V_o(k)e^{i(kr+\theta(k))} \frac{[ E(r) + E(r+R_{max})e^{ikR_{max}} + \cdots ]}{E(r) + E(r+R_{max}) + \cdots}$$

The value of $\hat{V}$ is estimated for varying wavelengths in Fig. 2.4. The value of r remains fixed, while the wave is allowed to move past r ($\theta(k)$ is varied from 0 to $2\pi$). The measured profile in Fig. 2.1a is used for $E(r)$. It is seen that $\hat{V}(r,k)$ has both a phase and amplitude response. The amplitude response was computed over many wavenumbers, and is shown in Fig. 2.5a. The maximum attenuation occurs when $V(r)$ and $V(r + R_{max})$ are 180° out of phase ($kR_{max} = \pi, 3\pi, ...$).

Besides moving a wave past a fixed range value, $\theta(k)$ can be held constant, and the response in range can be computed. This is analogous to estimating the amount of distortion in the measured profile caused by range-aliasing. This is shown in Fig. 2.6 for various values of k. The distorted wave maintains its wavenumber, but goes through a phase and amplitude shift, as in Fig. 2.4. Consequently, the amplitude response in Fig. 2.5a can also be interpreted as the transfer function between the true and measured wavenumber spectrum.

Given the coherent sonar's maximum range $R_{max}$, and so a bandwidth resolution of $\delta k = 2\pi/R_{max}$, the curve in Fig. 2.5a can be integrated over the measured wavenumber bands to give the expectant measured response. The result (Fig. 2.5b) is that the measured wavenumber spectrum will be approximately 50-60% of the true spectrum, across all wavenumber bands. If the simulated intensity profile is used, with $SNR_{ra} = 8$ dB at $R_{max}$, the wavenumber spectrum is then only attenuated

by 15% .

The above argument depends upon the Fourier-decomposition to be an accurate representation over all aliased ranges. The other extreme is to consider all aliased velocities to be uncorrelated. The aliased spectral peaks will be random, causing the summed spectrum to appear broad-band. Similarly, side-lobe contamination can also be considered as a sum of randomly Doppler-shifted sources. and modeled as a broad-band noise contaminant.

## 2.4    Instrument Package Movement

Sonar movement causes its own Doppler shifting of the return signal. Generally, sonar motion is only a concern at high frequency (i.e. surface wave frequency) and can be adequately removed by averaging. However, its variance does degrade the signal, thus requiring more averaging time for the same amount of precision.

Coherent sonars have additional instrument motion constraints. Doppler shifts are estimated on a $\Delta$ time period. If package movement is violent enough to completely decorrelate the signal (random movement of $O(\lambda)$ every $\Delta$ seconds), the velocity estimate becomes invalid. This implies that $\sigma_l$ should be kept below $V_{max}$ . Also, the beam must point at the same volume of water every $\Delta$ time period. Hence, rotations should be constrained to a fraction of the beam angle every $\Delta$ seconds.

## 2.5    Biota Effects

Chapter 3 discusses effects of a finite number of particles in the ensonified volume. Problems arise when not enough organisms are present to give a true 'volume averaged' velocity estimate. This will bias the velocity if the point source does not reflect the true volume average. Furthermore, point source measurements will cause aliasing in wavenumber space. Biota patchiness causes variability in range, leading to temporal range aliasing problems ($SNR_{ra}$ is small during the advection time of the patch).

Biota actively swimming will add their own variance to the return signal. For instance, velocity precision estimates in Fig. 3.7 show that during the diurnal migration cycle the variance more than doubles. Also, the nighttime variance is higher than during the daytime, presumably because zooplankton are more active at night. It is assumed that biota motions are much higher in frequency than the Vaisala frequency $\equiv N$. Biota effects can be removed by averaging in time, allowing water motions with frequency $< N$ to be resolved.

Another scattering problem, which arises from either instrument motion, biota movement, or background flow velocities, concerns how rapidly scattering particles pass through the ensonified volume. If the return signal is from a different set of particles on each transmission, the phase progression from one return to the next will be random, containing no useful information. Following the same approach as taken in App. B, it can be shown that the SNR is equal to the percent of the same particles remaining in the volume divided by the percent of new individuals. The minimum volume size should be limited so that only a small fraction of scatterers leave the ensonified volume between transmitted pulses.

## 2.6    Receiver Noise

Receiver bandwidth is normally chosen to match the transmission pulse width. For instance, the receive bandwidth would be 1 kHz for a 1 ms pulse width. Since this is typically much wider than $1/\Delta$ (the Nyquist frequency of the measured Doppler shift), it is appropriate to view electronic noise as a white noise source. Let $SNR_{en}$ equal the signal-to-electronic noise ratio of the system. An estimate of $SNR_{en}$ can be obtained by listening to the receive signal while not transmitting, and comparing this level to what is normally received. The effect of white noise on the velocity estimate depends upon the processing algorithm used.

## 2.7    Effect of Signal Processing Technique: Rummler Estimator

Numerous signal processing techniques can be employed to estimate velocity. The Rummler autocovariance estimator is most generally used because of its low overhead computational requirements, and robustness (c.f. Lhermitte and Serafin(84), Sirmans and Bumgarner(75)). This section concentrates on the Rummler technique.

If the carrier frequency is removed from the return signal (i.e. by heterodyning), the return from a specific range bin can be described by:

$$x(t) = x_o(t)e^{i\phi(t)} \tag{2.7}$$

where $\phi(t)$ is the variation in phase from $f_o$. The coherent sonar samples $x(t)$ once every $\Delta$ seconds. The Rummler method computes the autocovariance for the first lag in time ($\delta t = \Delta$):

$$C(\Delta) \equiv <x^*(t)x(t+\Delta)> = <x_o^2 e^{i\Delta\frac{d\phi}{dt}}> \tag{2.8}$$

where * denotes the complex conjugate, and <> signifies pulse-to-pulse averaging. Velocity is estimated from:

$$\hat{v} = \frac{\lambda}{4\pi\Delta} \arg[C(\Delta)] . \tag{2.9}$$

Miller and Rochwarger(70,72) explore the effects of estimating $\hat{v}$ from a total return consisting of the desired signal and an additive noise source that is either band-limited or white-noise. (i.e. from range-aliasing, acoustic cross-talk or receive electronics). The estimator of $\hat{v}$ has a variance dependent upon the the size and shape of the bandwidths. If the signal and noise are Gaussian with equal bandwidths (as might be the case with the range-aliased signal), then the total variance will be (Miller and Rochwarger(70)):

$$\sigma_{coh}^2 = \frac{\sigma_{signal}^2}{M} \left( 1 + 2/SNR + 1/SNR^2 \right) \tag{2.10a}$$

where $\sigma_{signal}^2$ is the variance of the desired volume, and $M =$ number of independent estimates averaged together. The signal variance can be expressed as:

$$\sigma_{signal}^2 = \left[ \sigma_w^2 + \sigma_b^2 + \sigma_f^2 \right]. \tag{2.10b}$$

Estimates are independent when $C(t_2-t_1) \ll 1$. The value of M does not equal the number of transmission pulses, but some subset separated by the decorrelation time. The decorrelation time of the biota movement, instrument motion, and water motion are not necessarily the same. The effective M may vary for the different components of (2.10).

## 2.8    A Sample Case: MPL Coherent Doppler Sonar

A coherent Doppler sonar system was developed at the Marine Physical Laboratory to measure the fine-scale shear field in the upper ocean (App. A). The system consists of four beams oriented in a Janus configuration with 1° wide beams. It is operated at 164 kHz. Typically, a pulse of 1 ms duration (3/4 m in range) is transmitted every 60 ms ($R_{max}$ = 45 m), giving an average ensonified volume size of $\approx 1/4$ m$^3$. The computed Nyquist velocity equals $\pm$ 3.8 cm/s. This small value would normally cause velocity aliasing problems in the oceanic environment. The MPL sonar avoids aliasing by estimating velocity differences over depth every two seconds, effectively measuring shear. Expectant values of oceanic shear give velocity differences over $\Delta r$ (= $c\tau/2$) that are less than $V_{max}$, so that no aliasing should occur. This technique also removes long period Doppler smearing caused by instrument movement (i.e. low-frequency swell motions). The drawback is that first-differencing the velocity also doubles the amount of variance.

Simulated beam pattern programs calculate $E_b$ = 10 dB for the composite transmit-receive transducers. Tests performed at sea measure minus 10-15 dB acoustical cross-talk for three beams contaminating the fourth (Fig. 2.7).

Range aliasing measurements at sea show a lower $SNR_{ra}$ than the simulated intensity profile (Fig. 2.3d). This is because the simulation does not include near-field effects, and the measured profile has a scattering layer located at midrange. The value of $SNR_{ra}$ = 4 dB = 2.5 will be taken as a representative value.

Instrument package variance was calculated from accelerometers, compass, and pressure sensor mounted inside the package (App. A). Variance was found to be $\approx 1.7$ (cm/s)$^2$. Most of this variance is caused by vertical motions, primarily due to FLIP tilting with the surface waves, and strumming of the cable.

Based on the model of Chapter 3, 80% of the return in an average ensonified volume comes from approximately six organisms, with the largest individual contributing 45% of the return. The velocity standard deviation (based on 15 second averages, with variances calculated over 20 minute periods) is shown in Fig. 3.7. There is a strong correlation with the diurnal migration, with the largest variance occurring at dawn and dusk. Nighttime standard deviation is higher (1.2 cm/s) than during the day (0.8 cm/s), presumably because the biota are more active at night.

The above standard deviations are estimated from the total variance (i.e., from all the components in (2.10)). A minimum nighttime value of $\sigma_b$ can be estimated from (2.10) by assuming all other variance sources are time-independent, and that $\sigma_b$ = 0 during the day, giving $\sigma_b$ (cm/s) = $0.9M^{\frac{1}{2}}$. M equals the number of independent estimates taken in a 15 second period, and depends upon how quickly biota motions decorrelate. For instance, if zooplankton motions decorrelate once every second (M = 15), then nighttime $\sigma_b$ = 3.5 cm/s.

Water velocity variance within the ensonified volume can be estimated from physical arguments. If the Richardson number = 1/4 sets an upper limit on shear,

then the maximum expected velocity difference can be computed for the vertical span of the ensonified volume (assuming no active mixing patches are present). This difference can then be used to bound the expected variance. For instance, if the Vaisala frequency $= 4$ cph, with a vertical span $= 60$ cm, then the maximum expected $\sigma_w = 0.84$ (cm/s).

Receiver noise based on long-range transmissions give $SNR_{en} = 25$ dB at $r = R_{max}$ (Fig. 2.3a).

## 2.9     Estimate of the Variance

The velocity variance due solely to the 'desired' ensonified volume can be estimated by summing the values of true water variance, biota variance, and instrument motion. Nighttime variance is estimated from (2.10b), assuming biota decorrelation time $= 1$ s, giving $\sigma_{signal}^2 = \sigma_w^2 + \sigma_b^2 + \sigma_i^2 = (0.7 + 12.2 + 1.7)/M = 14.6/M$ $(cm/s)^2$.

Range aliasing and acoustic cross-talk (both multi-beam and self-contamination) have a combined $SNR = 1/(1/SNR_{ra} + 1/SNR_{multi} + 1/SNR_{self}) = 1/(1/2.5 + 1/10 + 1/10) = 1.7$. It will be assumed that their bandwidths are equivalent to $V_{max}^2 = 14.4$ $(cm/s)^2$. This is nearly the value of $\sigma_{signal}^2$, so (2.10a) should be an appropriate estimation. This gives a total variance equal to $\sigma_{coh}^2 = \sigma_{signal}^2(1+2/1.7+1/1.7^2) = 2.5\sigma_{signal}^2 = 36.5/M$ $(cm/s)^2$. Variance caused by white noise is minimal since $SNR_{en} = 25$ dB. The effect of electronic noise will therefore be ignored.

Daytime precision can be estimated by assuming $\sigma_b = 0$ during the day, giving $\sigma_{coh} = 4.9/M^{1/2}$ (cm/s). The average day and night precision is $\sigma_{coh} = 5.5/M^{1/2}$ (cm/s). Fig. 2.8 displays an average autocorrelation curve taken at sea. The return signal has decorrelated to a value of 0.1 after one second. Independent samples can be assumed to be obtained at least once every second.

The above variance is for velocity along the beam, which is equal to:

$$U_{beam} = U\cos(\phi) + W\sin(\phi) \qquad (2.17)$$

where $U =$ horizontal velocity, $W =$ vertical velocity, and $\phi =$ angle of sonar with respect to azimuth $= 55°$ for the MPL sonar. Horizontal velocities are estimated by subtracting back-to-back beams and dividing by $2\cos(\phi)$, increasing $\sigma_{coh}$ by a factor of $2^{1/2}/(2\cos(\phi))$. The estimate of shear $(dU/dz)$ adds another factor of $2^{1/2}/\Delta z$ $(\Delta z = 60$ cm). The precision of shear is equal to $\sigma_{coh}(cm/s)/[\Delta z\cos(\phi)] = 0.03\sigma_{coh}$ $(1/s)$.

## 2.10     Comparison with PATCHEX Data Cruise Measurements

During the PATCHEX cruise in November 1986, a 7.5 day data set was collected using the MPL coherent sonar. Averaged data was written to tape every 30 seconds. Two repetition periods $(\Delta)$ equal to 50 and 60 ms were alternated on a two second period basis. A 30 second time span consists of 15 seconds of $\Delta = 50$ ms and 15 seconds of $\Delta = 60$ ms. Data analysis in Chapter 4 uses only $\Delta = 60$ ms, since it has a larger maximum range. Data was further reduced by computing 512 twenty minute average profiles ($=40$ records averaged per profile $= 600$ seconds of actual data). Standard deviation estimates based on these 15 second averages were calculated every 20 minutes, with results shown in Fig. 3.7. This figure shows $\sigma_{coh} = (0.8, 1.0, 1.2)$ (cm/s) for the (daytime, average, nighttime) values. Calculated

nighttime precision will agree with the measured value if M equals 25, correspond-
ing to a decorrelation time of 0.6 seconds. The calculated (daytime, average, night-
time) values become $\sigma_{coh}$ = (0.98, 1.1, 1.2) (cm/s).

Another comparison can be made by using the vertical wavenumber spec-
trum of the 512 average shear profiles for the entire cruise, as shown in Fig. 2.9.
This shows an average noise floor equal to 0.0065 1/s for the equivalent of a single
component of shear. The above estimated value (with M=1000 = 0.6 second
decorrelation time) gives $\sigma_{coh}$ = 0.0052 1/s, about 25% lower than measured. Stan-
dard deviation based on daytime-only profiles is estimated at 0.0049 1/s (Fig. 2.9).
Calculated daytime precision is $\sigma_{coh}$ = 0.0046 1/s, which is within 5% of the meas-
ured value.

## 2.11   Comparison with an Incoherent System

The precision of an ideal incoherent system, as given in (2.1), will be com-
pared with the daytime precision of 0.8 cm/s, as measured with the coherent sonar
over a 15 second period. It will be assumed that every transmission will be an
independent estimate, such that M = 15/$\Delta$ = 15/0.06 = 250. The transmission pulse
$\tau$ equals 1 ms (as for the coherent sonar), and c = 1500 m/s. The required fre-
quency to give $\sigma_{inc}$ = 0.8 cm/s is $f_o$ = 940 kHz. The signal would be in the noise
floor at 45 meters at such a high frequency. Since wavenumber is not truly
resolved until a 4 m wavelength (Fig. 2.9), the value of $\tau$ can be tripled ($\tau$ = 3 ms =
1.8 m vertical resolution), reducing the required $f_o$ to 310 kHz, which would have no
problems going 45 meters. Note again this is assuming 'optimum' performance. For
example, Plueddemann(87) and Hansen(85) calculate actual standard deviation to be
roughly twice that of the optimum for the system developed by Pinkel.

For the incoherent velocity precision to remain constant, spatial resolution
can only be gained by increasing $f_o$ (from (2.1), $f_o \tau$ = constant for $\sigma_{inc}$ = constant).
Attenuation of the signal (which is equivalent to 1/(maximum range)) depends on $f_o^2$
(c.f. Urick). The spatial resolution divided by the maximum range is proportional to:

$$\frac{\text{spatial resolution}}{\text{maximum range}} \approx \frac{\tau}{f_o^{-2}} \approx f_o(f_o \tau) \approx f_o \quad \text{for } \sigma_{inc} = \text{constant.}$$

As an incoherent system is pushed to higher frequencies to gain spatial resolution,
the total number of estimates in range decreases. A coherent system will be pre-
ferred when, for the same spatial resolution, it can achieve a larger maximum range.
Large-scale phenomena (with low spatial resolution) are best performed by
incoherent processing, whereas microstructure measurements are best suited for a
coherent sonar. The fine-scale field of 1 m vertical resolution over a 50 m max-
imum range pushes both incoherent and coherent methods towards their limits,
resulting in both systems having about the same performance capabilities.

## 2.12   Summary

An analysis of error sources in a coherent sonar system has been presented.
Precision is affected by white noise from receive electronics, variance from the
desired ensonified volume, and acoustic interference (range-aliasing and side-lobe
contamination). Variance from the desired ensonified volume comes from true
water motion, instrument movement, and biota actively swimming. Biota motion and

instrument movement are considered high frequency phenomena, such that their signals can be removed by time averaging. Modeling of range-aliasing for varying wavenumbers suggest that the measured wavenumber spectrum will be underestimated across all resolved wavenumbers. The amount of attenuation will depend upon the total energy contained in the aliased ranges.

Expected velocity variance is calculated for a coherent sonar designed by MPL for use off the research platform FLIP. The total return energy is computed to be comprised of 63% from the desired ensonified volume, 25% from aliased ranges, and 12% from side-lobe contamination. Future work can improve precision by crossing the transmit and receive beams such that only the near range is 'focused', and by better rejection of side lobe energy.

Variance from the desired range bin is estimated to be near $V_{max}$. This level is mainly due to biota activity and instrument motion. Only instrument motion can be reduced, but would pose a difficult task. If it is assumed that all acoustic interference is eliminated, such that variance only depends upon water, biota, and instrument motions, velocity precision would improve from (1.0,1.2) cm/s (daytime, nighttime) computed values to (0.3, 0.8) cm/s (for a 15 second averaging period).

Comparison of calculated variance with measured values agree reasonably well. Differences may result from not including higher biota variance levels observed at dawn and dusk, or because a 0.6 second decorrelation period is inappropriate for some components of the variance.

When the MPL coherent Doppler system is compared with an optimum incoherent system, it is found that the incoherent system would be required to operate at twice the frequency to achieve the same results. The MPL's sonar's temporal, spatial, and maximum range requirements push both the incoherent and coherent processing methods towards their respective limitations.
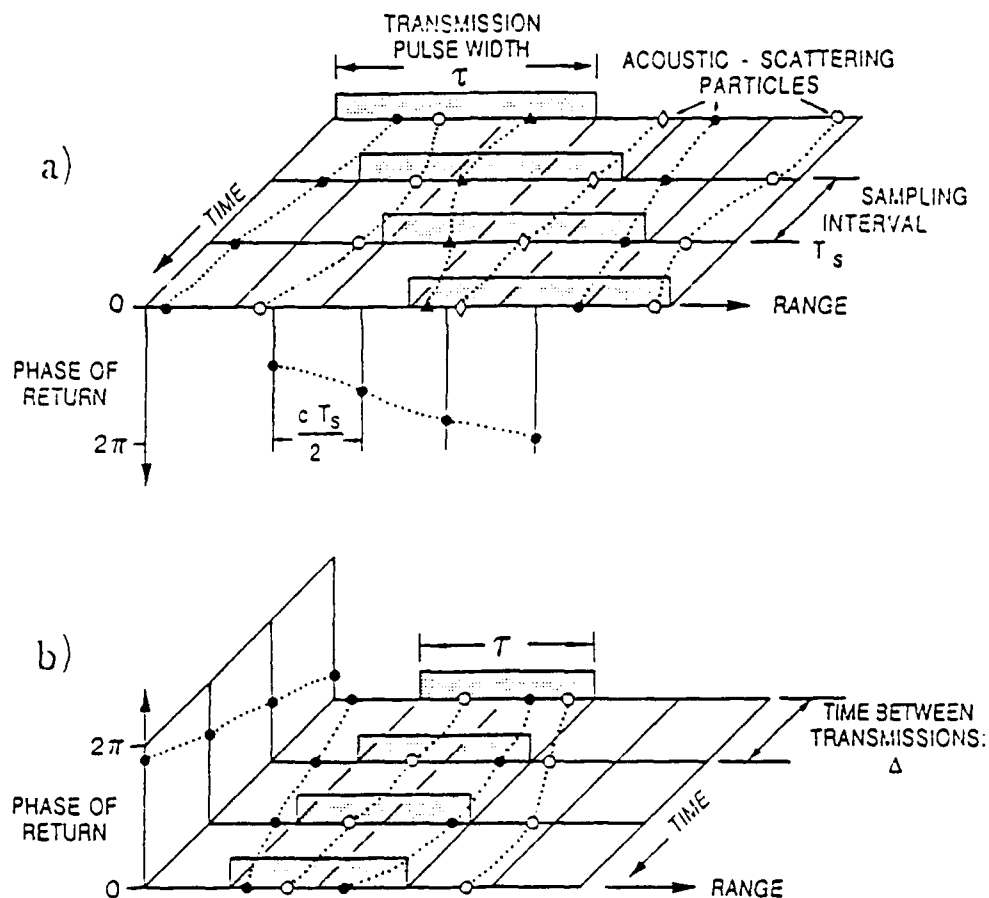
**Figure 2.1.** a) With incoherent processing, a transmission pulse of duration $\tau$ travels outward in range, ensonifying a number of scatterers at any instance in time. The return signal is sampled every $T_s$ seconds, with phase information recorded. Each new phase estimate represents a change in ensonified volume by distance $cT_s/2$, with a certain percent of different scatterers present. The return phase will only stay correlated for a pulse duration time period, setting a limiting bandwidth on the Doppler estimate equal to $1/\tau$.

b) With coherent processing, every $\Delta$ seconds another pulse is transmitted with the same phase. The time-varying phase return at range r will reflect the true Doppler shift, as long as the particle's advection time through the ensonified volume is long compared to $\Delta$. Ambiguity arises if particle movement causes a phase change greater than $2\pi$ in a $\Delta$ time period.
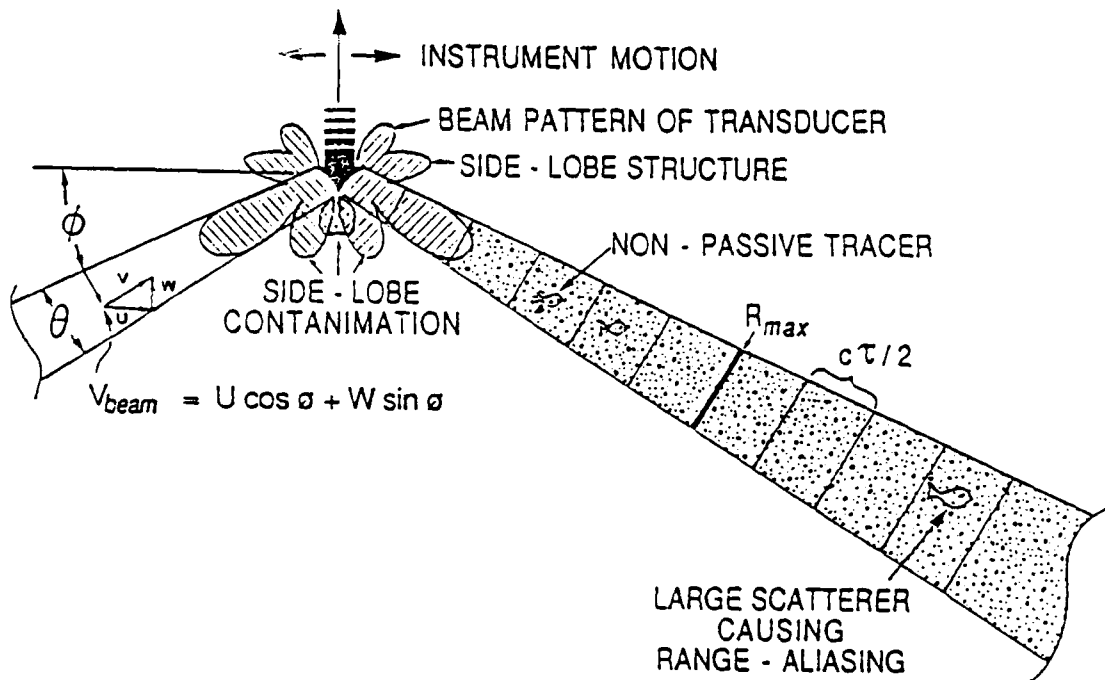
**Figure 2.2.** A coherent sonar in an oceanic environment has many variables that come into play. Instrument movement and biota actively swimming cause false Doppler shifts of the true water velocity. Scattering beyond $R_{max}$ (the maximum range resolved) contaminate the return signal. This range-aliasing may dominate the return when large scatterers are present at far range. Sonar side lobes will transmit and receive energy, causing both self and cross-beam contamination.
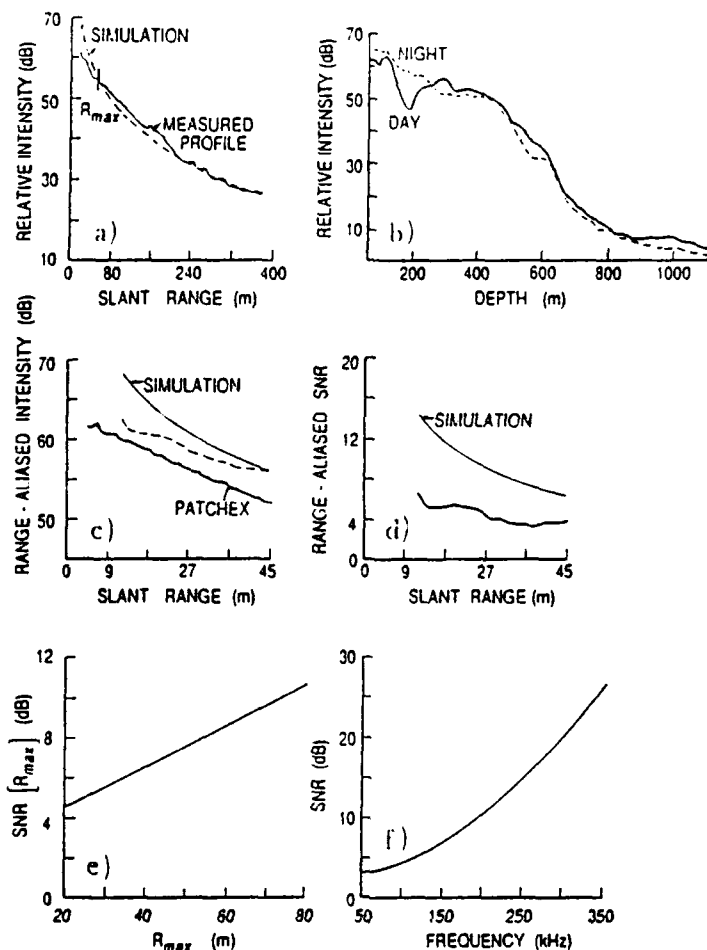
**Figure 2.3.**
a) Computer simulation of (2.3), with a noise floor added, is compared with an hour-long average afternoon profile taken at sea. Differences between actual and simulated curves are due to near-field effects not being modeled, and variation of biota distribution with depth. $R_{max}$ is shown for the PATCHEX repetition rate ($\Delta$ = 60 ms). All intensity return further out in range than $R_{max}$ will contaminate the desired signal.
b) Twelve-day averages of day/night intensity profiles from a 75 kHz sonar were calculated by Plueddemann(87) during the MILDEX cruise. MILDEX took place in October 1983 in the same locale as the PATCHEX cruise in October 1986. Note the 10 dB variability near 200 m depth.
c) Coherent sonar range-aliased intensity profiles as calculated from (2.6) are shown using both the measured and simulated profiles in a). The 7.5 day PATCHEX average profile is also displayed (at an arbitrary dB level), showing an overall slope more reminiscent of the simulated data than the measured profile. This may be the result of the biota variability effecting the hour-long measured profile, as mentioned above.
d) $SNR_{ra}$ was calculated from (2.5) for both the simulated and measured profiles. Discrepancies are due to not modeling near-field effects and biota variability.
e) $R_{max}$ is varied in (2.5), which is equivalent to trying different pulse repetition rates ($\Delta$). This is plotted against $SNR_{max}$ as calculated at r = $R_{max}$ (where SNR is at its lowest). As $\Delta$ increases there is less intensity aliasing, and SNR improves.
f) Transmission frequency $f_o$ can also be increased, causing greater attenuation at far range, and better SNR values. The nonlinear relationship is due to absorption being dependent upon the frequency squared.
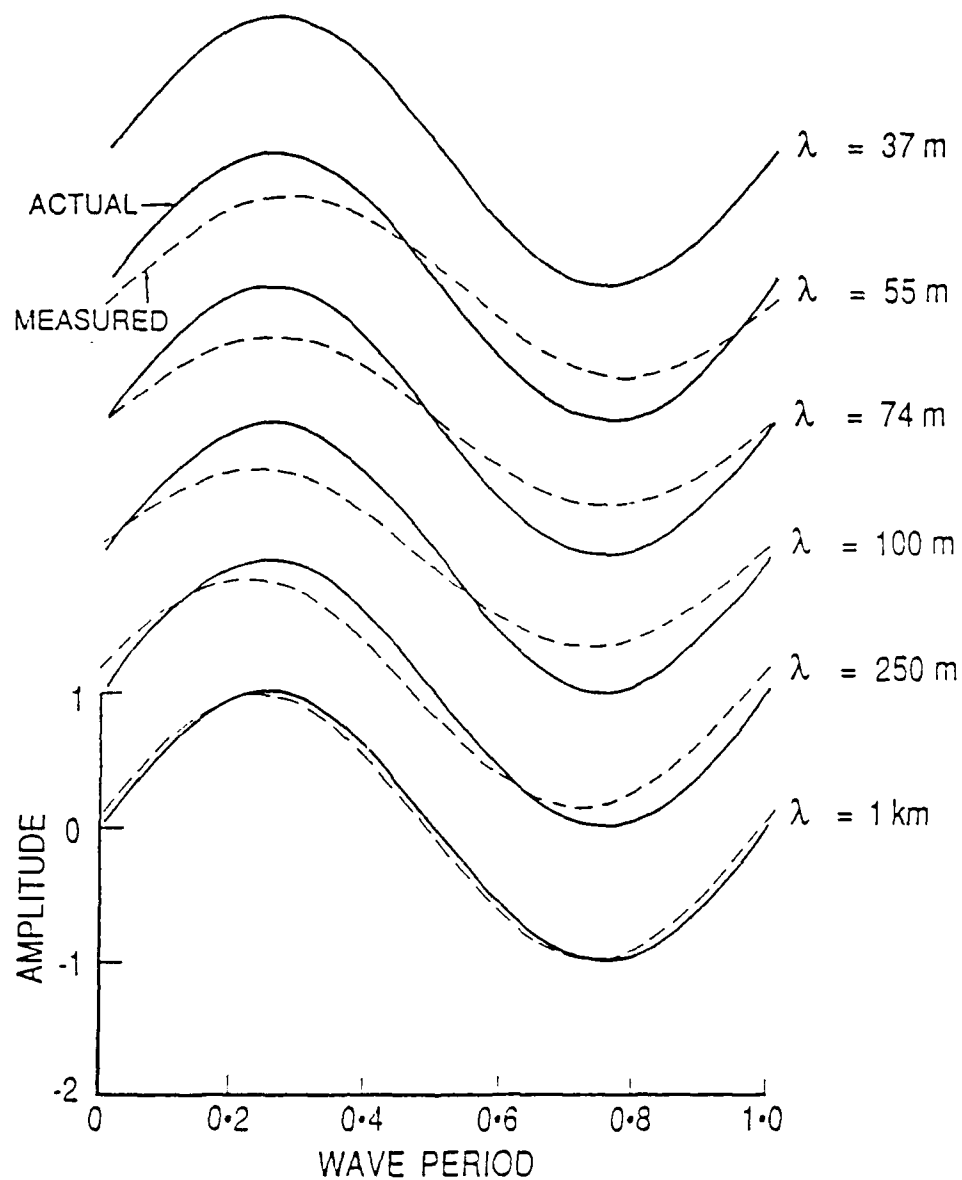
**Figure 2.4.** A velocity field with vertical wavelength λ propagates past a fixed range r. The dark lines are the true velocities, while the dashed lines are values contaminated by range-aliased components. The range-aliased estimates are both phase and amplitude shifted. A vertical wavelength of 37 meters corresponds to the maximum vertical range of the sonar ($R_{max}sin(\phi)$ ).
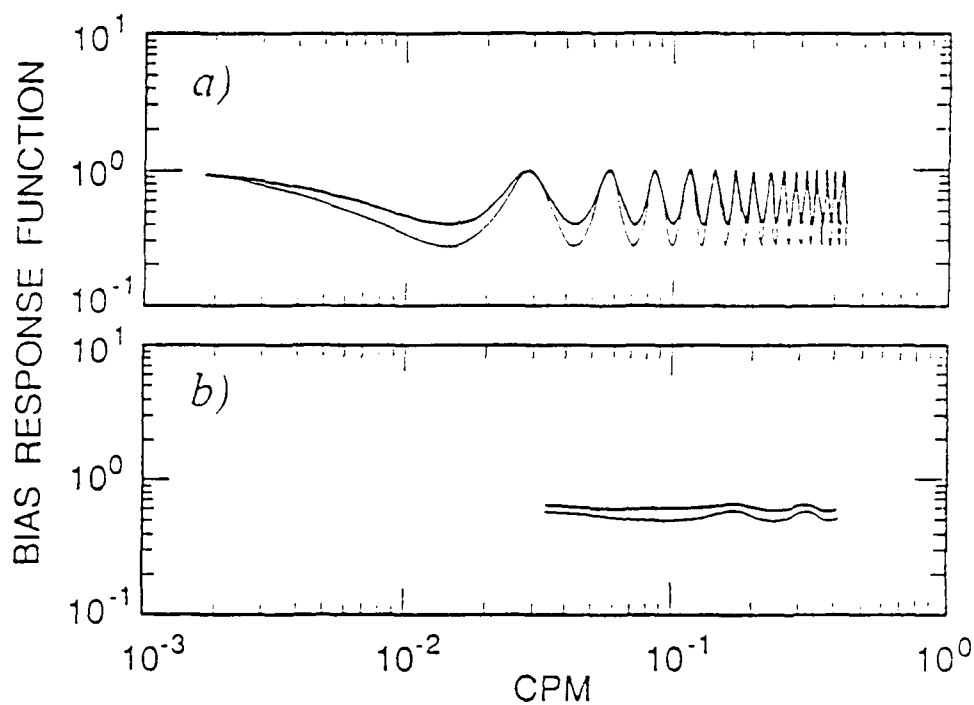
**Figure 2.5.** a) The amplitude response of Fig. 2.4 is shown over a wide wavenumber range. Maximum attenuation occurs when the first aliased return is 180° out of phase with the desired return. The dark line is the response function for slant range equal to 15 m from the sonar, and the light line is at 45 m (maximum slant range).

b) The amplitude response in a) is averaged over the wavenumber bands resolved by the coherent sonar (bandwidth = 1/(maximum range)). The dark and light lines correspond to responses at 15 and 45 m range respectively.
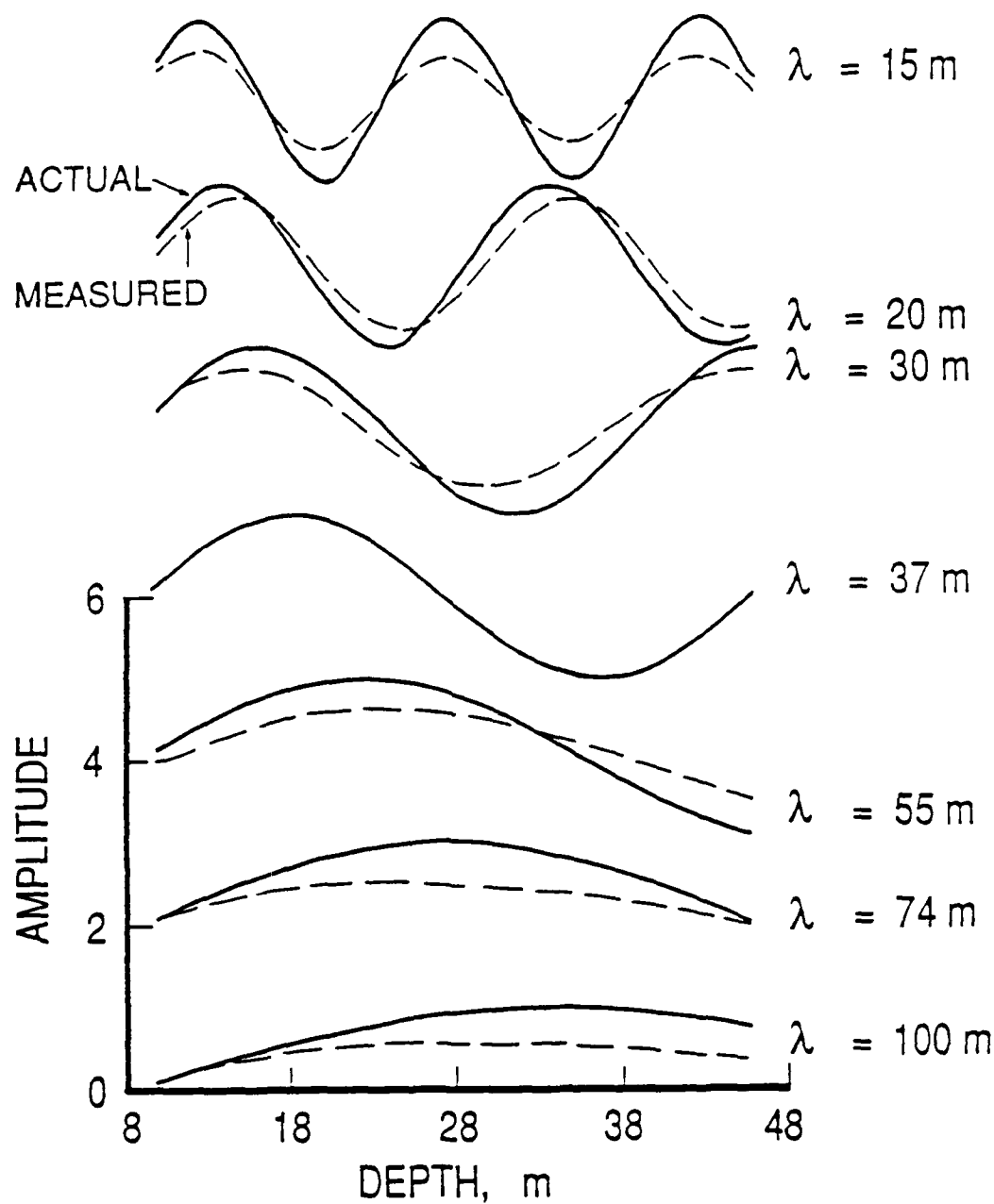
**Figure 2.6.** The range-aliased response as a function of range is shown for vertical wavelengths from 15-100 m. The dark lines represent the true velocity profiles, while the dashed lines are the estimates contaminated by range-aliasing.
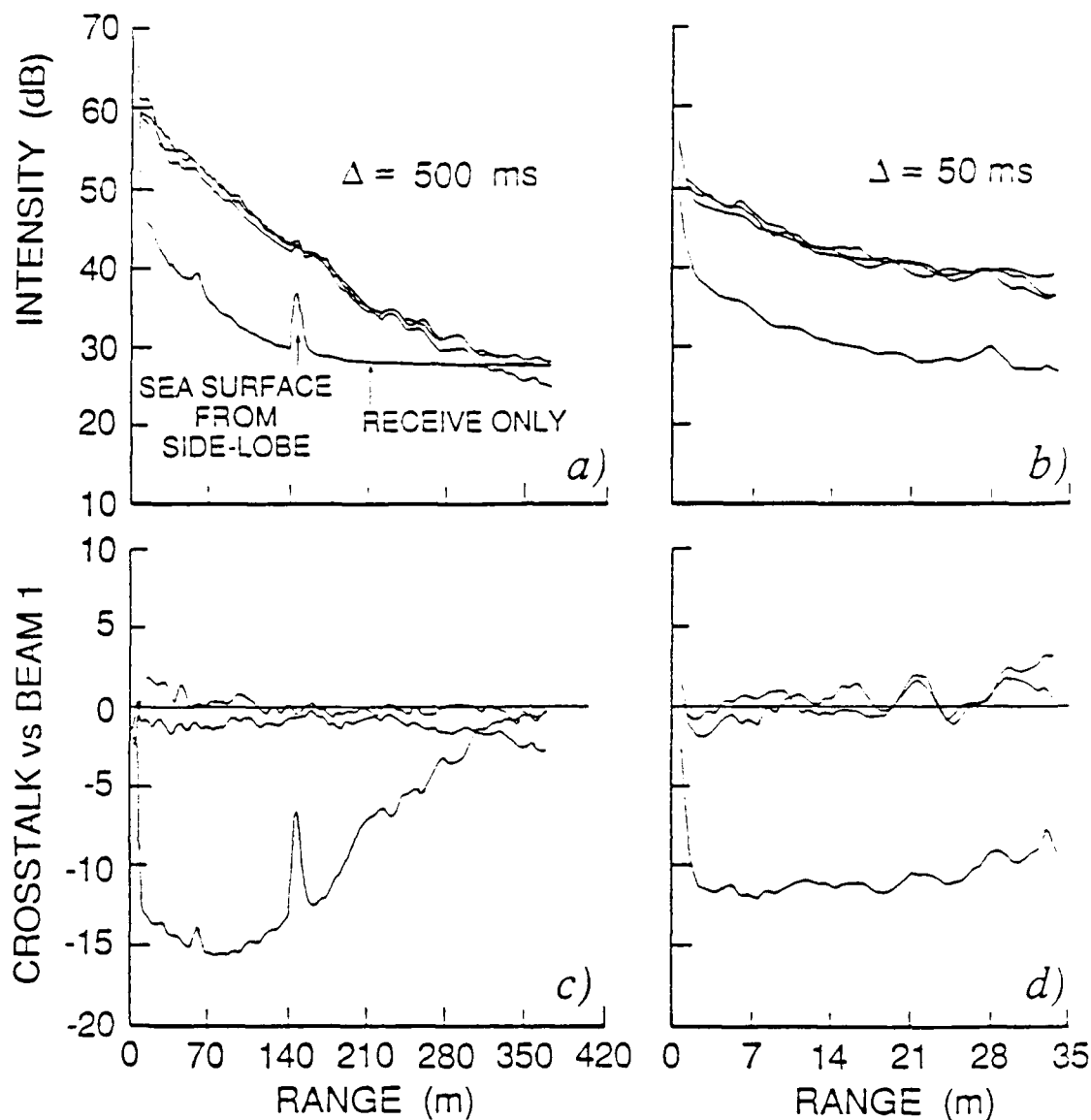
**Figure 2.7.** a) Three out of the four beams of the MPL sonar transmitted every 0.5 seconds. The return signals of all four beams were recorded. The 'bump' seen at 145 m range in the fourth (non-transmitting) beam is most likely a side lobe reflecting off the sea surface. The sonar's depth was 145 m.

b) The same transmit configuration as in a), but now transmitting at a 50 ms repetition period.

c) The return profile of beam 1 is subtracted from the other three beams in a), giving a measure of crosstalk level into the receive-only beam. All beams merge at far range since they share a common noise floor.

d) Cross-talk is estimated from b). When all cross-beam contamination is also range-aliased, the receive-only beam has an intensity value 10 dB below the other beams. When all four beams are transmitting, any one beam will have approximately 10% of its total return contaminated by side-lobe contamination from the other beams.
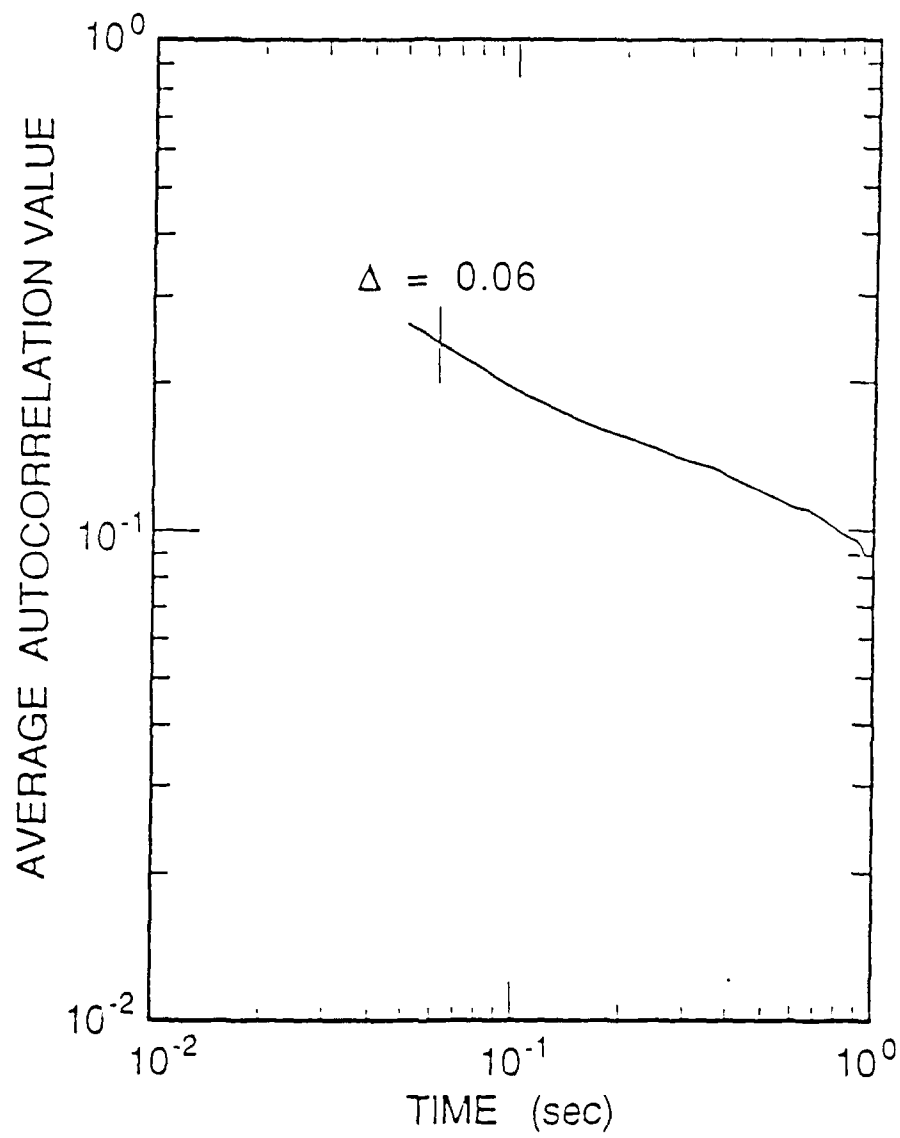
**Figure 2.8** An average value of the autocorrelation function is shown based on 30 minutes of data. A time lag of $\Delta$ = 60 ms was used during the PATCHEX experiment.
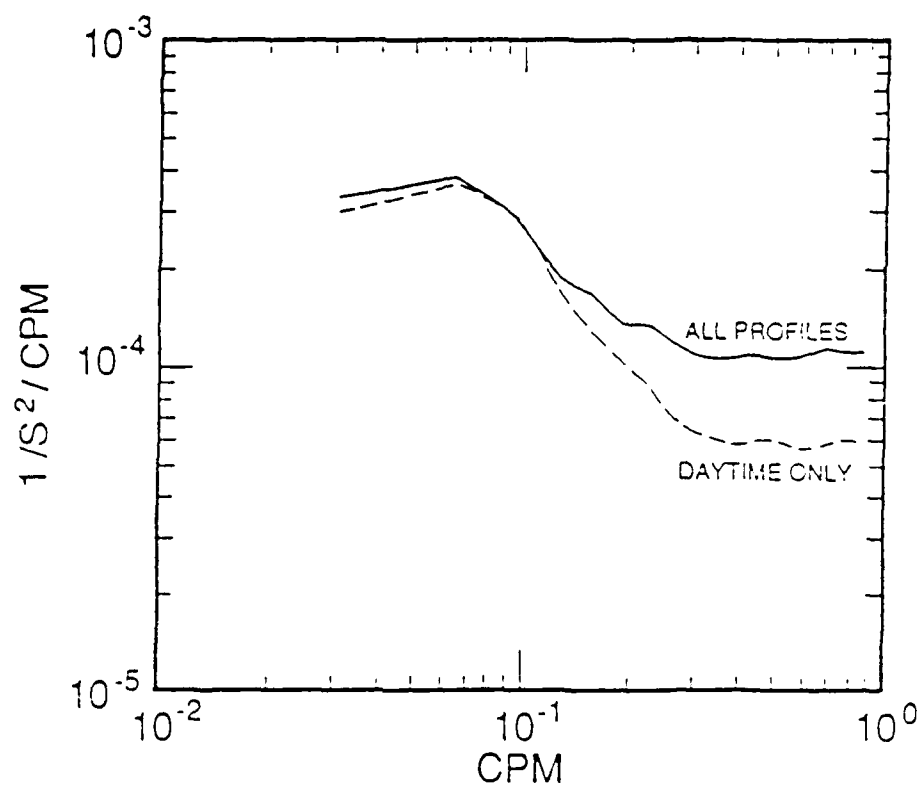
**Figure 2.9** Vertical wavenumber spectra were computed from the 512 twenty minute averaged profiles of the PATCHEX data cruise for both components of shear. Spectra were calculated from all profiles and from daytime-only profiles. The noise floor at high wavenumber allow variance estimates to be made of the noise level for a single component of shear, giving a daytime value of 0.0049 1/s and average value of 0.0065 1/s

# CHAPTER III

## The Effects of Zooplankton Biomass Distribution
## on the Precision of a Doppler Sonar

### 3.1   Introduction

Standard Doppler theory makes two suppositions regarding particle behavior: Many organisms are present in the scattering volume, and they have a mean velocity reflecting that of the true water motion. As Doppler sonar techniques are applied to finer scale measurements in the open ocean, ensonified volumes have been growing smaller. However, with small volumes, the number of scattering targets may be few, resulting in both a non-uniform average over the scattering volume, and the possibility of an inaccurate velocity estimate (when the biota are actively swimming). Since fine-scale motions contain important high-frequency components, it is imperative that the Doppler sonar's precision is accurately quantified.

As microstructure scales are approached, the statistical nature of the acoustic-scattering particles must be considered. Specifically, the spatial and temporal characteristics of these scatterers must be modeled to estimate the quality of velocity measurements. This chapter specifically addresses the open ocean environment, where zooplankton are expected to be the major contributors to volume reverberation.

Determining reliable error bounds is complicated by the fact that the zooplankton distribution varies not only with depth and geographic location, but also temporally on scales from the advection time of a patch, through diurnal migration cycles, to seasonal variations. The uncertainty in the spatial distribution of targets and their swimming properties might be the limiting factor on making high-quality, high-frequency time series measurements from a volume-reverberation sonar.

The zooplankton distribution problem is approached here by modeling 'pseudo-distributions' of targets based on biomass estimates from ocean observations. These are coupled to a backscattering strength model to produce estimates of the number of 'acoustically significant scatterers' in a given ensonified volume. Performance estimates can then be made based on computer simulations incorporating a variety of estimation algorithms.

### 3.2   Modeling the Backscattered Signal

Let the sonar transmission be modeled as a boxcar pulse with duration $r$ and carrier frequency $f_0$ :

$$T(t) = \begin{cases} S_0\sin(2\pi f_0 t) & t<r \\ 0 & t>r \end{cases} \tag{3.1}$$

As the pulse travels outward, it will ensonify a volume V, given by:

$$V(r) = \left[\frac{cr}{2}\right]\frac{\pi}{4}(r\theta)^2 \tag{3.2}$$

where $c$ = speed of sound, $\theta$ = full beam angle (narrow beam approximation), and $r$ = range along the beam. (3.2) is only valid for the far field (where spherical spreading occurs), and for a radially symmetric beam.

Within this volume will be N individual organisms, which will backscatter the transmitted pulse to varying degrees. Plankton are typically modeled as fluid-filled spheres in the prediction of their acoustic scattering properties (Anderson(50)). Johnson(77) has modeled the backscatter strength $\sigma_b$ for a sphere of radius a to be:

$$\sigma_b(a) = \frac{A_1 f_o a^6}{2 + 3(ka)^4} \tag{3.3}$$

where $k$ = wavenumber ($2\pi f_o/c$), and $A_1$ is a constant dependent upon the density properties of the sphere. The backscatter function is shown in Fig. 3.1. Note $\sigma_b$ changes from an $a^6$ response to $a^2$ at about $a$ = 0.1-0.2$\lambda$, where $\lambda$ is the acoustic wavelength at frequency $f_o$ ($\lambda$ = $c/f_o$).

The total backscattered return is given by:

$$R(r) = \sum_{j=1}^{N(r)} \sigma_b(a_j) e^{i(2\pi f_o t + \phi_j)} \tag{3.4}$$

where $\phi_j$ = phase of the $j^{th}$ zooplankton, whose value is dependent upon the particle's position. To know the characteristics of the return signal, both the number of scatterers $N(r)$ in the scattering volume, and their size distribution $a_j$ must be known. This will determine if the sonar's signal is dominated by a few large zooplankton, or is well distributed over many small scatterers. The approach here is to estimate $N(r)$ and $a_j$ using a biomass distribution model developed by biological oceanographers. Biomass distribution is defined as the amount of biomass per unit volume contained within a size category (i.e. all the biomass of organisms between 1-2 mm in size).

Marine biologists have done both theoretical modeling (c.f. Platt(85)) and analysis of oceanic data sets (Rodriguez and Mullin(86a), henceforth RM86a) of biomass distribution. RM86a calculated such a distribution for the North Pacific Central Gyre, obtaining for macrozooplankton:

$$\frac{\Delta B}{\Delta w} = A_o w^{-1.13} \tag{3.5}$$

where w is the mean individual weight ($\mu gC$) of a size category with a weight spread ($w-\Delta w/2$, $w+\Delta w/2$), and $\Delta B$ = biomass per unit volume ($\mu gC/m^3$) for this category. $A_o$ is a measurement of overall biomass level, and is dependent upon the location and its productivity. A surprising result of their study was that the power relation (-1.13 term) exhibited only a small spread (-1.07-1.34) over various depth ranges, seasons of the year, and diurnal variations. This result compares well with the Platt theoretical model, which predicts a -1.22 slope.

(3.5) can be integrated to estimate the amount of biomass present between two individual weights to obtain:

$$B(w_1, w_2) = \int_{w_1}^{w_2} A_o w^{-1.13} \, dw = \frac{A_o}{0.13} (w_1^{-0.13} - w_2^{-0.13}) \tag{3.6}$$

This states that the sum of the biomass from organisms (per unit volume) which weigh between $w_1$ and $w_2$ equals $B(w_1,w_2)$.

If a geometric mean weight is defined as:

$$w_m = (w_1 w_2)^{1/2} \tag{3.7}$$

then the number of individuals (n) with weight $w_m$ in the ensonified volume V can be modeled as:

$$n(w_1,w_2) = \frac{B(w_1,w_2)}{w_m} \cdot V = \frac{A_o V}{0.13} \frac{(w_1^{-0.13} - w_2^{-0.13})}{(w_1 w_2)^{1/2}} . \tag{3.8}$$

When $n(w_1,w_2) = 1$, V equals the minimum volume size at which one organism of weight $w_m$ is likely to be found.

It is now possible to model the number of particles and their size distribution given a volume V. A starting weight for $w_1$ is chosen, and $w_2$ is computed from (3.8), thus giving $w_m$ for the first particle. The new value of $w_1$ is set to the old $w_2$, and the above computation is repeated. This iteration process is continued until no $w_2$ exists such that (3.8) can be satisfied for n=1. This last step essentially defines the largest organism expected to be found in the finite volume V. N particles have now been computed with weights $w_m(j)$ which satisfy the biomass distribution as given by (3.5).

It remains to convert $w_m(j)$ into an equivalent radius such that it can be used in (3.4). (3.5) was computed in terms of carbon weight ($\mu gC$) by RM86a. The radius required is that of a sphere with an equivalent displaced volume of the organism. How carbon weight relates to displaced volume will depend upon the type of zooplankton and its size. It is theorized (Omori and Ikeda(84), and Wiebe et al.(75)) that the 'ideal' cubic relationship is expected:

$$4/3\pi a^3 = c_1 w \tag{3.9a}$$

(carbon weight is simply proportional to the displaced volume by some constant $c_1$ ). However, Wiebe et al.(75) also give an empirical fit based on many data sets as:

$$4/3\pi a^3 (mm) = 1.36 w^{0.808} (\mu gC) \tag{3.9b}$$

This suggests that heavier organisms are actually smaller than predicted by the ideal relationship. (3.9a) and (3.9b) can be rewritten to give:

$$a(mm) = 0.63 w_m^{0.333} (\mu gC) \tag{3.10a}$$

$$a(mm) = 0.688 w_m^{0.27} (\mu gC) \tag{3.10b}$$

where $c_1$ was calculated such that (3.9a) = (3.9b) for a = 1 mm. RM86a argue that Wiebe et al.'s empirical relation is not consistent with their oceanic data, which varied through seven orders of magnitude in a, and is simply an artifact of measurement technique (as also suggested by Wiebe et al.). Nevertheless, (3.10b) will be used as an extreme bound for comparison.

The only unknown left is the biological factor $A_o$, which must be ascertained from field data from each locale of interest. Due to diurnal and patchiness variability, $A_o$ can vary by a factor of four even for the same site (Greenblatt(80), RM86b, Fig. 3.7). Therefore, once a rough number has been estimated for an area, models should be run for different values of $A_o$.

## 3.3    An application of the Model

Marine Physical Laboratory at Scripps Institution of Oceanography has developed a 164 kHz Doppler sonar which ensonifies $0.2-0.5$ m$^3$ volume. This instrument has been deployed off the Southern California coast. Net tows have been performed near the same locale by Greenblatt(80), who found the zooplankton population to be dominated by copepods and euphausiids, which averaged 1-2 individuals/m$^3$ for the 4-8 mm class size category. By using Johnson's empirical length-to-equivalent radius formula, this translates into 1-2 organisms/m$^3$ with a $=$ 1.2-3.4 mm. Simulation of this biomass distribution yields a value of $A_o = 50$ $\mu$gC/m$^3$, which is within a factor of two of RM86a's value of 100 $\mu$gC/m$^3$.

The iteration process was run on (3.8) using the cubic relation of (3.10a). A minimum length of 0.3 mm was used as the starting point, yielding a total of 136 individuals per 0.25 m$^3$ with a size distribution as shown in Fig. 3.2.

The total return signal can now be computed from (3.4). There are two quantities which are helpful in interpreting the return signal:

$$dF(a_j) = \sigma_b(a_j) \ / \ \sum_{k=1}^{N} \sigma_b(a_k) \qquad (3.11)$$

$$F(a_j) = \sum_{k=1}^{j} \sigma_b(a_k) \ / \ \sum_{k=1}^{N} \sigma_b(a_k) \qquad (3.12)$$

where dF represents the fraction of the total return which particle $a_j$ contributes, and F gives the fraction of the total return in which particles $\leq a_j$ contribute. These are plotted in Fig. 3.3. Fig 3.3a shows that the largest individual contributes about 44% of the total return, the next individual 16%, etc. Fig. 3.3b shows that all particles $<0.6$ mm represent $<10\%$ of the total backscatter signal, while 80% of the return is determined by the six largest organisms. Also shown in Fig. 3.3b is the result of using Wiebe et al.'s relation (3.10b), demonstrating that the largest particle is of smaller radius, and contributes only 25% of the total return.

The product $A_o V$ can be varied to explore the sensitivity of the results to both volume reverberation size and total biomass present in the water. Plotted in Fig. 3.4a is the number of largest organisms which contribute 80% of the return, henceforth regarded as the number of 'significant scatterers.' It is seen that the number of significant scatterers increases linearly with $A_o V$. Shown in Fig. 3.4c is the percent of the total return backscattered by the largest individual (or MSB, for the Most Significant Bug). Also shown is the percent return from the two and three largest organisms combined. Fig. 3.4b shows that the size variation of the MSB encompasses the $0.1-0.2\lambda$ transition zone of Fig. 3.1. At low values of $A_o V$, each new individual added represents a backscattering strength near the $a^6$ region, and thus dominates the return. At higher values of $A_o V$, the backscattering goes as $a^2$, and the contribution from each new individual goes down. This is reflected in Fig. 3.4c,

where the contribution of MSB has it's most rapid change through this transition region. The variance in all three plots is contributed to the model's 'least count noise' of computing plus/minus one extra organism before the maximum cutoff.

Besides modifying the ensonified volume size, the sonar designer can also alter the transmission frequency $f_o$. Fig. 3.5 repeats Fig. 3.4, but now as a function of frequency ($A_oV$ is held constant). Again, the effect seen is the change in slope of backscattering strength as a function of the largest individual present. Near 115 kHz, the dominant scatterer's size exceeds $0.1\lambda$. Fig. 3.5c displays the required $f_o$ to guarantee that the MSB $>0.1\lambda$ for a given $A_oV$. A sonar designer working with a known frequency and $A_o$ can estimate the volume required such that the size of the largest expected individual lies in the $a^2$ backscattering region.

## 3.4    Error Estimates

It remains to translate scatterer distribution into velocity variance estimates. Precision and accuracy will be affected by how truly the individuals represent the actual water velocity, and the manner in which the signal processing algorithm reacts to the input signal. The effects of the algorithm can by tested by taking the modeled biomass distribution, assigning each particle some normally-distributed velocity about the mean, and doing a computer simulation using that algorithm.

The use of the Rummler autocovariance method (a standard real-time processing technique) has the interesting result that a marginal advantage is achieved in precision by having fewer scatterers (App. B). This results from the fact that having only one scatterer present provides a perfectly correlated signal, with degradation proceeding in a N/(N-1) manner after that.    Fig. 3.6a displays results of computer simulations for various values of $A_oV$, showing no dependence of velocity variance on N. Standard deviation estimates from an oceanic data set with various pulse widths (1/2, 1, 2 ms), show less than a 15% deviation with volume size (Fig. 3.6b). This factor of four variation in $\tau$ would correspond to approximately twice the number of significant scatterers (from Fig. 3.6), and thus does not provide a broad range for verification. However, both simulation and actual data suggest that having more scatterers present does not aid the processing algorithm itself.

The number of scatterers does play a role in providing a good spatial statistical average. If only one individual is dominant, then a point measurement somewhere in the scattering volume is obtained. This does not represent a true volume average, and creates high-wavenumber aliasing problems in wavenumber spectra estimates. Only by averaging many velocity estimates together, such that the individual's position varies over the entire volume, can a spatial average be obtained. However, if the dominant organism is selectively following some microstructure feature within that volume, the averaged value will still be a biased estimate of the true volume average.

Measured biota motion variance is of the order 1-4 $(cm/s)^2$ (Fig. 3.7, Plueddemann(87)), which is of the same order as the expected oceanic velocity differences on a 1-10 m scale. Since variance is not reduced by having many scatterers present, higher precision will only be obtained by doing either spatial or temporal averaging on velocity estimates. Either approach will constrain the highest wavenumbers (or frequencies) which can be measured.

## 3.5   Summary

A modeling technique has been presented to estimate the statistical charac-teristics of backscattering from a specified volume size and sonar frequency. This approach is based on an empirically measured biomass distribution model which agrees well with theoretical derivations. The results enable the sonar designer to estimate the number of significant scatterers in a return signal, given the type and size of organisms dominant in the deployment area. Due to the high variability of zooplankton numbers and size distribution within patches, the above model only provides the expected results on average.

For a small ensonified volume (such that the largest organism has a radius less than $0.1\lambda$), the largest individual provides more than 50% of the total return signal (Fig. 3.5). In contrast, Greenblatt(80) concludes that large scatterers do not dominate the total signal. This results from Greenblatt working in the limit of an infinite volume size, where scattering is expected from all size ranges.

The percent return expected from the largest individual can be used as a guide to predict the amount of variance in the return intensity. For instance, for the MPL sonar volume range, Fig. 3.4 suggests an intensity variation of 30-50%. Reason-able bounds can therefore be placed on an 'anomalous' intensity return (i.e. due to nekton swimming through the volume), and the data processed accordingly.

It was found that the number of scatterers had no important effect on the Rummler autocovariance estimator. Computer-simulated velocity variance was within 30% of actual input variance over a range of 10-870 individuals occupying the volume, with no trend apparent. This implies increasing the ensonified volume will not increase precision due to averaging over more scatterers. However, an increase in the number of organisms will provide a better volume averaged velocity estimate, thus decreasing the degree of aliasing in wavenumber.

Due to biota motion variance matching that of fine-scale motions, the true ocean velocity field can only be separated from biota swimming by assuming that the zooplankton's motions contain only high-frequency components, and time-averaging to retrieve the background velocity field. However, this averaging results in loss of high-frequency velocity information, which may, in the end, defeat the scientific purpose of a high-resolution Doppler sonar.
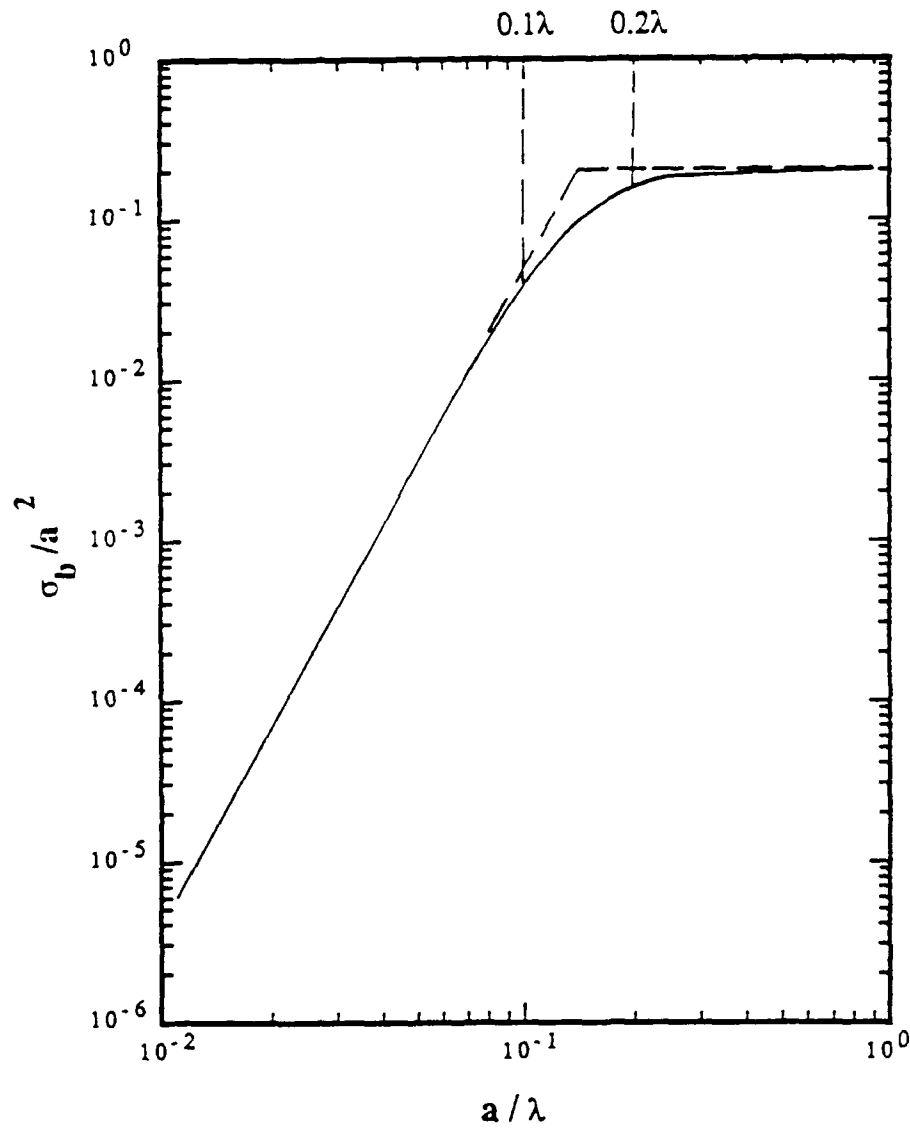
**Figure 3.1.** Johnson's backscattering model is plotted versus radius. Note the change of slope occurs between 0.1-0.2λ.
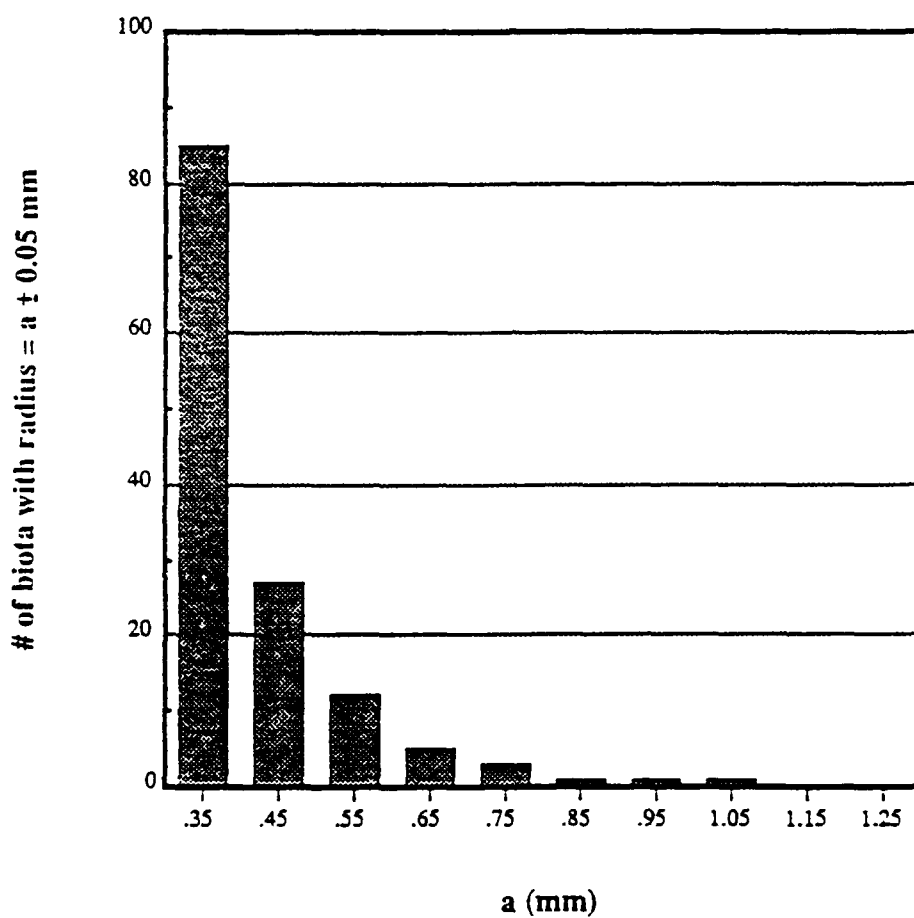
**Figure 3.2.** Simulation of size distribution is computed for a $1/4$ $m^3$ volume with a biomass level set equal to oceanic measurements by Greenblatt. Shown is the number of individuals with radius equal to $a\pm0.05$ mm.
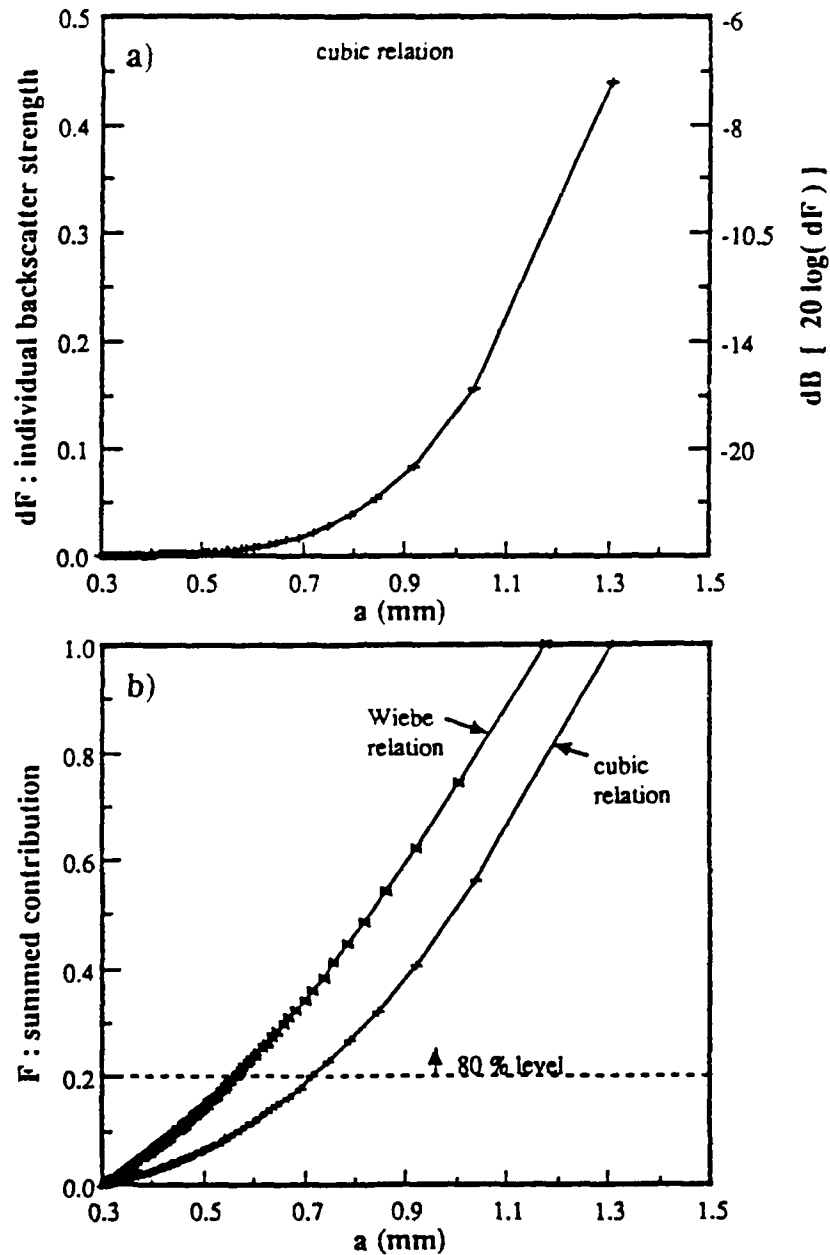
**Figure 3.3.** a) Estimates of individual backscattering strength as a fraction of the total return are calculated for the distribution shown in Fig. 3.2. Assumed sonar frequency is 164 kHz ( = MPL sonar). Each cross-mark represents a single individual as calculated from the simulation. The largest organism contributes 44% of the return, next largest 16%, etc. b) Cumulative backscattering strength (the integral of a) ) is plotted for both the cubic relation of carbon weight to displaced volume, and the empirical Wiebe relation. The cubic relation places greater importance on the larger organisms, showing that 80% of the return can be attributed to the six largest individuals, whereas the Wiebe relation calculates over two dozen organisms comprising 80% of the return.
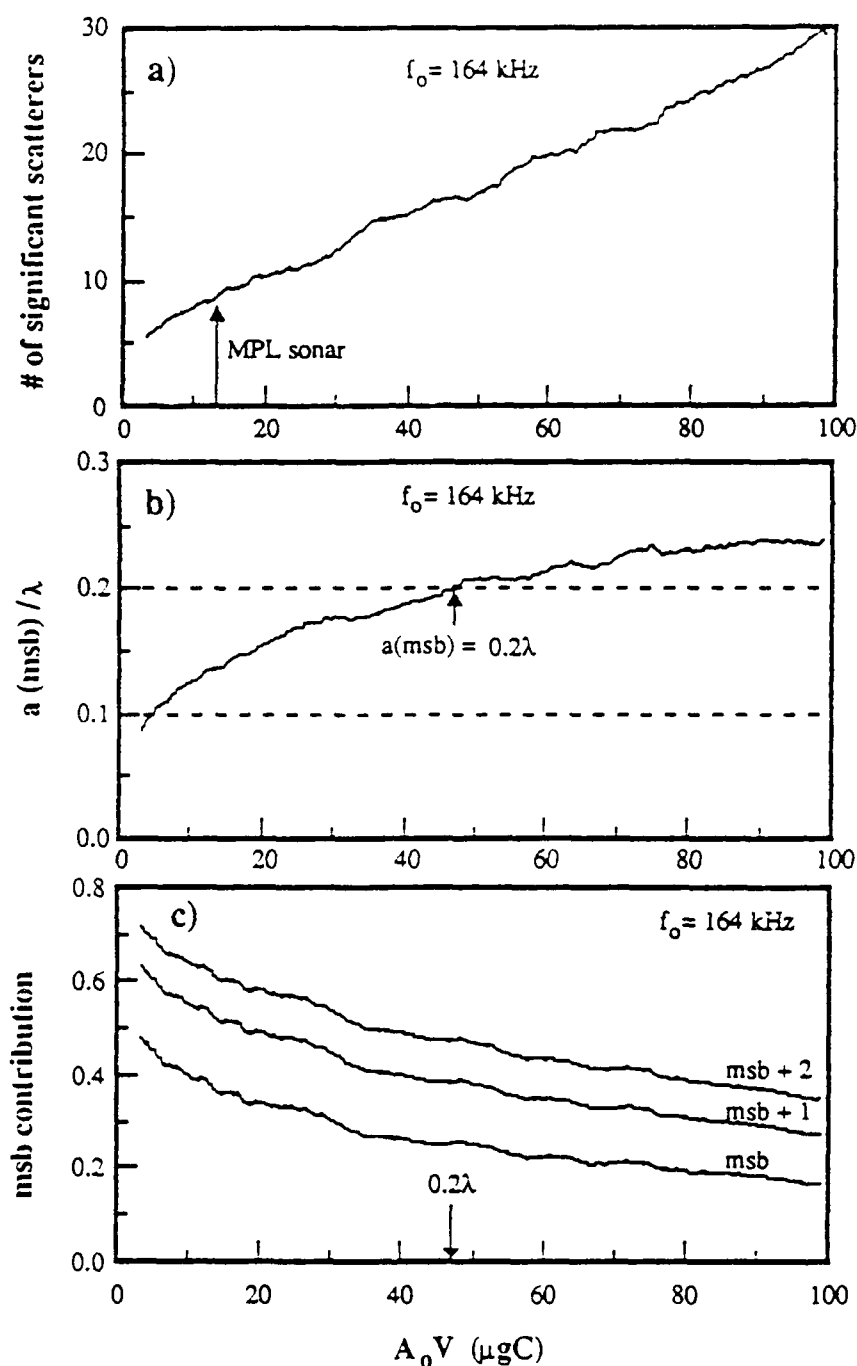
**Figure 3.4.** a) As the product $A_oV$ increases (for frequency = 164 kHz), the number of largest organisms contributing 80% of the total return (the number of 'significant scatterers') also rises. The variance in the plot is an artifact of the model. b) As $A_oV$ is varied, the fractional size $(a/\lambda)$ of the largest individual (or Most Significant Bug (MSB)) passes through the $0.1$-$0.2\lambda$ transition zone of Fig. 3.1. Correspondingly, in c), the fraction of the total return from the largest individual shows a decrease in rate of change for $a>0.2\lambda$. Also shown is the percent of the total return for the two and three largest organisms combined.

42
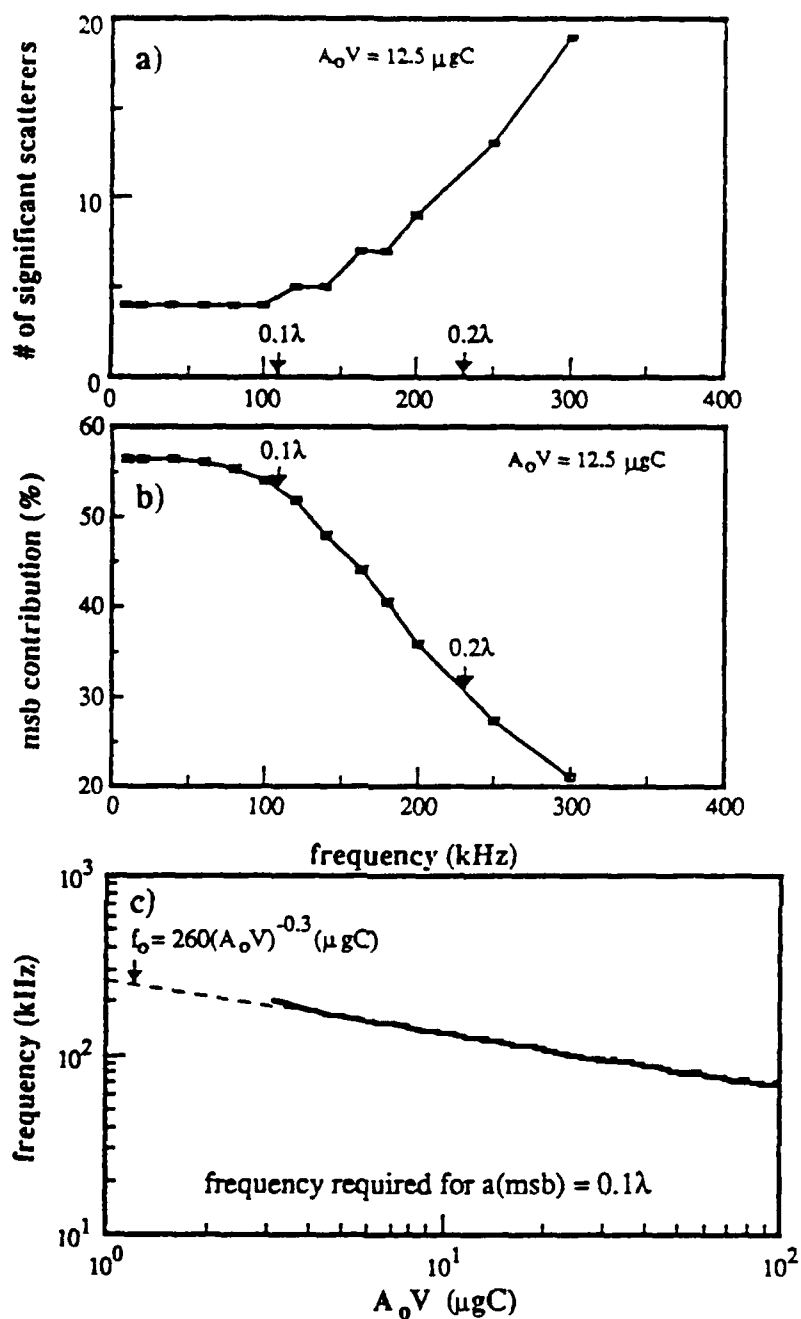
**Figure 3.5.** a) The number of significant scatterers is calculated for various frequencies. Biomass level is held constant to the value used in Fig. 3.2. Also shown is the frequency where $\lambda$ reaches a value such that the largest organism's radius is equal to 0.1 and 0.2$\lambda$. b) The contribution from MSB is calculated for varying frequency. Again, it is seen that the percent of the total return from the largest individual is a strong function of the change in power relation in Johnson's model. c) displays the frequency necessary such that a(MSB) = 0.1$\lambda$ for a given $A_oV$.
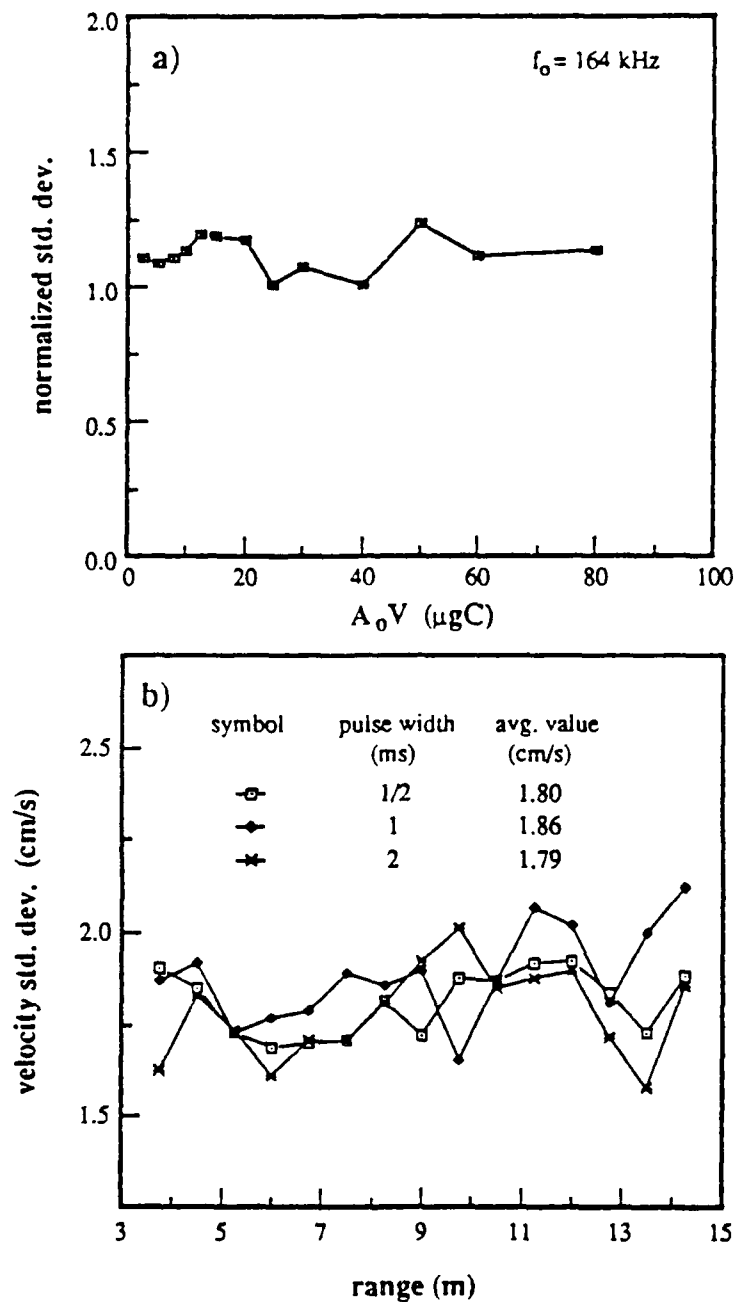
**Figure 3.6.** a) Normalized standard deviation for the Rummler autocovariance technique is calculated using the backscatter strength distribution as shown in Fig. 3.3 for varying values of $A_oV$. No trend is apparent, with estimated values having less than 30% variation, and averaging 10% higher than the input value. b) Velocity standard deviation estimates are given as a function of range for three different pulse widths (1/2, 1, 2 ms). Again, no apparent dependency on pulse width (and therefore number of organisms) can be seen.
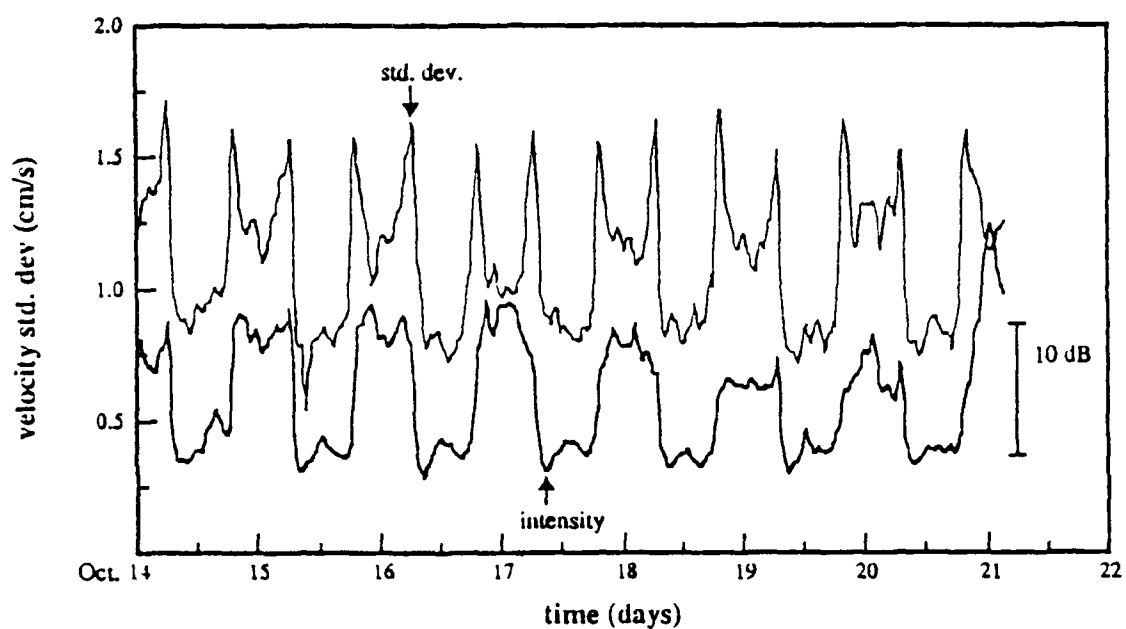
**Figure 3.7.** The time series of intensity (dark line) and velocity standard deviation is comprised of 512 points of 20 minute averages over all beams and range for the 7.5 day PATCHEX data set. Strong correlation is seen with the diurnal migration. Nighttime variance levels are higher than during the day, suggesting that the biota are more active at night.

## CHAPTER IV

## A Statistical Comparison of Upper Ocean Shear and Strain

### 4.1   Introduction

This chapter explores the spatial and temporal characteristics of the vertical shear and strain fields on vertical scales of 3-600 meters as measured during the 1986 PATCHEX cruise. Historical observations and theories of the vertical wavenumber shear spectrum are reviewed. This is followed by a description of the PATCHEX experiment, along with a presentation of the shear and strain data sets. Frequency-wavenumber spectra are estimated, and consistency tests with linear theory are investigated. Contamination effects due to horizontal and vertical advection are modeled to help resolve discrepancies. Richardson number functions are computed for various 'advection-corrected' spectra. Results are compared with other proposed spectral models, followed by speculation on the possible role of caustics on spectral shape.

### 4.2   Historical Observations of Shear Spectra

Garrett and Munk(72) hypothesized a model of the frequency-wavenumber spectrum for the internal wave field which was consistent with various data sets, and used linear theory to relate the assorted spectral forms to each other. This model has been fine-tuned over the years (c.f. Munk(81), Desaubies and Smith(82)) to better agree with newer, more detailed observations. One of the major assumptions of this model is that the frequency and wavenumber dependency of the spectrum is separable, i.e. $E(\omega,m) = f(\omega)*g(m)$, where $m$ = vertical wavenumber, and $\omega$ = frequency. In their model, $m$ is related to the horizontal wavenumber k through the linear dispersion relationship:

$$\frac{m}{k} = \pm \left[ \frac{N^2 - \omega^2}{\omega^2 - f^2} \right]^{\frac{1}{2}} \tag{4.1}$$

where N = Vaisala frequency, and f = Coriolis frequency. Gargett et al.(81) have further hypothesized a 'universal' shear spectrum based upon observations from three different types of shear profilers during the FAME experiment (Fig. 4.1). This model has a flat spectral shape out to vertical wavenumbers of order 0.1 cpm, where it then breaks off to a $m^{-1}$ form. At scales smaller than 1 m, the spectral form is irregular, dominated by the intermittent presence of mixing. Gargett et al. hypothesize that at low wavenumbers, where linear internal wave theory is appropriate, the shear spectrum's energy level will scale in a WKB fashion as $N^2$. They also suggest that the change in slope at 0.1 cpm is a depth-independent quantity, referred to as the 'cutoff wavenumber' $\equiv m_c$. This is thought to occur at the scale where the Inverse Richardson Function $\equiv IRF(m_c) = 1$, with $IRF(m)$ defined as:

$$IRF(m) = \frac{1}{N^2} \int_0^m \phi(m)dm, \tag{4.2}$$

where $\phi$(m) is the shear wavenumber spectrum.

Comparison of other, more recent, vertical wavenumber spectra from the literature (Fig. 4.2) provides some collaboration, although no specific agreement with the Gargett et al. proposed spectrum. Included in this collection are the Gargett et al.(81) measurements, data from Toole and Hayes(84) in the near-Equatorial region, Northeastern Pacific data from Pinkel(85), and California coastal measurements by Duda(86). Also shown are the results from this chapter. Most observations do show a nearly-white spectrum at long wavelengths, with a break in slope at about 10-20 m, going to a $m^{-1}$ to $m^{-2}$ slope.

When the spectral energy levels are normalized to the same value at 0.1 cpm (Fig. 4.2b), it is seen that Gargett's spectral shape is a fair model of most of the observations. Past studies have not done time-series analyses on fine-scale shear, giving no insight into which frequencies play a dominant role at high wavenumbers.

## 4.3    Description of PATCHEX Experiment

During October 1986 the research platform FLIP participated in the PATCHEX experiment. The experiment site was at 34° N, 127° W, approximately 300 miles west of Point Conception, California (Fig. 4.3a). Numerous instruments were deployed from FLIP. Two profiling CTD's monitored the density field in the top 560 meters of the water column. Four long-range Doppler sonars (using pulse-to-pulse incoherent processing) measured the oceanic velocity field to depths in excess of one km. A four-beam short-range Doppler sonar (using pulse-to-pulse coherent processing) measured fine-scale shear from 150-180 meters in depth. A full set of environmental sensors was also deployed. Each instrument was operational for various lengths of time: from a little over one week for the short-range sonar (this was its first full-deployment) to over three weeks for the CTDs and long-range sonar.

FLIP was kept on station by a two-point mooring. Her relative bearing remained constant to within ± 15° for the entire cruise, as shown in Fig. 4.4. Also shown is wind direction, and wind speed. Light winds were experienced for most of the cruise.

## 4.4    Short-Range Sonar Data : Fine Scale Shear

The short-range Doppler system consisted of a four beam Janus configured sonar located 145 m below the surface (Fig. 4.3b). A technical description of the instrument can be found in App. A, with a discussion of its performance given in Chapter 1. The sonar transmitted a 1 ms pulse downwards at a 55° angle every 60 ms, giving it 60 cm vertical resolution over 30 m depth (The first 6 meters of the return were not usable due to degradation of the signal by near-field effects). To remove the effect of Doppler-smearing of the signal by instrument motion, velocity differences in range, rather than velocity itself, were computed every two seconds. These velocity-difference estimates were subsequently averaged in time and recorded onto tape every 30 seconds. During PATCHEX, a 7.5 day time series was recorded at the 145 m depth. Measured standard deviation (Fig. 3.7) suggest that along-beam velocity estimates were precise to within 0.8 cm/s rms for each 30 second record during the day. Variability was ~50% higher at night, and roughly twice as high during the dawn/dusk migration times.

The 7.5 day data set was divided into 512 twenty minute average profiles, with each profile comprised of 50 independent estimates in depth. The Janus configuration consists of two pairs of back-to-back beams. The pairs are orthogonal, allowing both horizontal components of vertical shear to be computed by subtracting back-to-back beams.

To accurately estimate the vertical shear low wavenumber variance (to provide comparison with the long-range sonar's data set), while still allowing the ease of using a FFT routine, each depth profile was linearly interpolated to give 64 total points in depth. If the profiles were instead padded with zeroes to give 64 points, then the Fourier transform would be computed over 38 m in depth (instead of the actual 30 m). The lowest wavenumber resolved by the FFT would not correspond to the actual resolution of the sonar, providing inaccurate comparison to the long-range sonar. The linear-interpolated profiles were also low-pass filtered to remove energy in wavenumbers > 0.4 cpm. The final data set consists of a 64x512 array in depth-time, allowing for easy Fourier decomposition into wavenumber-frequency space. The resulting time series for both components of shear are shown in Fig 4.5.

Vertical wavenumber spectra of shear were computed for both the total cruise and for daytime-only profiles (Fig. 4.6). It is seen that the daytime-only spectrum has roughly half the noise level as the spectrum of all profiles. The spectra exhibit a break in slope at $\approx$ 16 m wavelength, with a $m^{-1}$ slope at higher wavenumbers, which agrees well with the Gargett et al.(81) model. However, when a modeled white noise floor is subtracted from the spectrum, a $m^{-2}$ slope emerges at the higher wavenumber. Since these spectra are computed from time-averaged profiles, the data may be suffering from spatial smoothing caused by the vertical displacement and straining of the high-frequency internal wave field within each twenty minute averaging period. Isopycnal displacement based on CTD casts (taken once every three minutes) has a variability of 1.2 m over 21 minute periods. It is expected that the shear field has been displaced 1.2 m during the averaging time, thus acting as a low-pass spatial filter on the data. If this is modeled as a boxcar filter in depth of width 1.2 m, then the wavenumber spectrum should be divided by the $\sigma_{inc}^2$ function to retrieve the original shape. This is also shown in Fig. 4.6, where there is now closer agreement with a $m^{-1.5}$ slope.

## 4.5   Long-Range Sonar Data : Large Scale Shear

During PATCHEX, long-range sonar data were collected for 22 days using a 75 kHz four-beam Janus configured system, with beams pointed downwards at a 52° angle. A technical description of this system can be found in Plueddemann(87). Pulses of 30 ms duration were transmitted, giving a vertical range resolution of 18.5 m. The return signal/noise ratio exceeded unity at depths in excess of 1 km. However, to avoid possible velocity biasing problems which occur at low signal-to-noise (Plueddemann(87)), only the first 600 m of depth was used in the present analysis. For comparison with the short-range sonar, only a subset of the total 22 day data run was used. 512 18-minute averaged shear profiles were computed, to give 6.4 days of data overlapping the short-range sonar data set in time. The two components of the shear field were computed by subtracting back-to-back beams (as done with the short-range sonar). A low-pass filter in wavenumber was applied to remove energy above 0.03 cpm. Corrections were also applied in wavenumber to correct for the measurement effects of sampling with a volume-averaging pulse, and using the first-differencing technique to estimate shear.

## 4.6    Shear Wavenumber-Frequency Spectral Analysis

Given both long-range and short-range sonar data sets, the wavenumber-frequency spectrum of shear can be estimated over 3-600 m vertical scales. Rotary spectra were formed by Fourier transforming in both space and time the complex data set (u + iv), where u,v denote the two components of the shear field. This allows the clockwise, counterclockwise, upward, downward, and total spectral energy to be analyzed.

Wavenumber-frequency spectra were computed for both the long-range and short-range sonars by breaking down the 512x64 data arrays into seven 128x64 arrays (seven 38.4/46.6 hour time periods for the long-range/short-range data sets), with each array overlapping another by 50% in time. A triangular window was used in both space and time. All seven spectral estimates (four independent) were averaged together to increase precision. The wavenumber-frequency spectra were subdivided into six bands: 44-16, 16-8, 8-4, 4-2, 2-1, and 1-0.7 hour periods. The average spectral energy density was calculated for each frequency band. Before results are presented, the attributes of WKB scaling are discussed.

## 4.7    WKB Scaling

The shear field is thought to consist of linear waves at low wavenumbers, with nonlinear waves (and perhaps 'vortical mode' contamination) at higher wavenumbers. The low wavenumber, 'linear regime' of the shear spectrum should scale in a WKB sense. Proper scaling for the 'nonlinear regime' at high wavenumbers is unknown. The Gargett et al.(81) model reflects these two features by having a high-wavenumber cutoff independent of depth (non-WKB-scaling) and a low-wavenumber energy level which scales as $N^2$ (as per WKB theory).

Since strong nonlinearities are expected at O(60 m) vertical scales and shorter (Holloway(80), Munk(81)), it is not clear whether the long-range sonar data set should be WKB-scaled. WKB scaling of linear internal waves suggests that both amplitude and wavenumber will vary as functions of the Vaisala frequency N. A linear wave packet should have its vertical wavenumber vary by N, with its shear variance being proportional to $N^3$. For a signal with a finite bandwidth, this amplitude variation is comprised of two parts: There is a spectral energy density level that varies as $N^2$, and a changing of the spectral bandwidth that scales with N.

The Gargett et al. model does not assume that the high wavenumber cutoff scales with N. This model therefore predicts a total shear variance which scales as $N^2$ (instead of $N^3$, as predicted from WKB theory). The long-range sonar's shear variance is plotted versus depth, along with $N^2$ and $N^3$ for the cruise-average, and historical Vaisala frequency profiles, in Fig. 4.12. The best fit is for the shear variance scaling with $N^2$, where N is based on the historical Vaisala frequency curve (Fig. 4.11b). However, the cruise-average $N^3$ does follow the shear variance well for depths greater than 200 m.

Figs. 4.7a and b demonstrate the resulting wavenumber spectra obtained in depth when WKB-scaling is either ignored(a) or applied(b). The non-linear regime's spectral density is assumed to scale with $N^2$, as per Gargett et al. model. The low-pass filter applied to the long-range sonar forces the 0.03 cpm depth-independent high-wavenumber cutoff. The depth-averaged non-WKB-stretched spectrum accurately depicts the high-wavenumber cutoff, but distorts the low-wavenumber response. The linear regime's energy band is centered at the same wavenumber that defines its peak at the average Vaisala frequency value of $\overline{N}$. Let the bandwidth

of the linear regime equal $\delta m = m_2 - m_1$. WKB theory suggests that both $m_2$ and $m_1$ vary by N with depth. The ratio $m_2/m_1$ therefore remains constant. When $\delta m$ is displayed on a logarithmic plot, it appears constant in width, although its absolute value is proportional to N. By WKB-stretching (Fig. 4.7b), the nonlinear regime's high-wavenumber cutoff now appears variable in depth (or similarly, the long-range sonar's low-pass filter is now variable in depth). The depth-averaged spectrum has now 'smeared' the high-wavenumber cutoff, while maintaining the integrity of the linear regime. The linear regime's peak is centered at the same wavenumber as the non-WKB-stretched spectrum.

The long-range sonar data set was processed in three different formats. No WKB scaling was implemented with one set ($\equiv$ non-WKB). Another data set had only WKB amplitude-scaling applied, such that the shear variance was constant in depth ($\equiv$ WKB-A). Amplitude was scaled using the historical Vaisala frequency profile, and assuming that the shear variance scaled with $N^2$. The final data set had both WKB amplitude-scaling and WKB-stretching in depth, so that a linear internal wave should appear with a constant wavenumber at all depths ($\equiv$ WKB-SA). Time series of both WKB-A and WKB-SA data sets are shown in Figs. 4.9 and 4.10.

To compare the effects of WKB-scaling, wavenumber-frequency spectra were computed for all three data sets (see above section for details on spectral processing). Results are shown in Fig. 4.8, based on the long-range sonar's average Vaisala frequency of $\bar{N} = 2.6$ cph. The non-WKB and WKB-A spectra agree well. As in Fig. 4.7b, WKB-SA has distorted the high-wavenumber cutoff of the filter. Major disagreement between WKB-SA and WKB-A occurs only for the inertial band (16-44 hour periods), where WKB stretching has decreased the bandwidth by a factor of two.

WKB scaling of the spectrum to a different depth requires an adjustment in energy level and wavenumber. The Gargett et al. model hypothesizes just a shift in energy level for wavenumbers > 0.01 cpm (the lowest wavenumber resolved in their measurements). The long-range spectral estimates are readjusted using both techniques in Fig. 4.8b. Spectra are rescaled from $\bar{N} = 2.6$ cph to $\bar{N} = 5.3$ cph (the average value for the short-range sonar's depth range). Shear spectral density levels are rescaled by a factor of $(5.3/2.6)^2 = 4.2$. The WKB approach rescales all wavenumbers by $(5.3/2.6)$, which shifts the spectrum over by a factor of two. For comparison, spectral estimates from the short-range sonar are also shown.

In later sections, shear spectra are compared with estimates from vertical strain data, which spans 0.5 to 1/256 cpm in vertical wavenumber. The strain's high wavenumber band (which is well into the nonlinear regime) is not expected to follow WKB-stretching. To preserve the high-wavenumber spectral shape, the strain is not WKB-stretched. To compare strain and shear spectral estimates fairly, the WKB-stretched long-range spectrum is not used. This allows either the non-WKB or WKB-A spectrum to be used. Both are nearly identical in form. The non-WKB spectral estimates will be used in future discussion. This decision is based primarily on the fact that uncorrected WKB profiles have larger amplitudes at the shallower depths. This automatically weights the high wavenumber spectral estimates in the depth region at which the short-range sonar was located.

## 4.8    Discussion of Shear Spectra

The non-WKB long-range sonar spectrum is compared to the short-range sonar spectrum in Fig. 4.15a. The short-range spectral energy levels appear

approximately 40% lower than the long-range level. This may be from the effects of range-aliasing of the short-range sonar causing attenuation in wavenumber (Chapter 2), or due to WKB rescaling of the amplitude overestimating the variance at shallow depths (as seen in Fig. 4.12). Also shown in Fig. 4.15a (light lines) are the long-range spectral levels optimally matched to the short-range levels (long-range spectrum multiplied by 0.6). This optimized composite spectrum will be used in future discussion, although it's absolute variance may be 40% low of reality.

Both sonar systems are contaminated by noise. The long-range sonar estimates velocity, such that its noise will appear white in velocity wavenumber spectra, and with a $m^{+2}$ slope in shear spectra. In Fig. 4.15b, a modeled noise spectrum equivalent to $\sigma_{rms} = 1$ cm/s after six minutes of averaging (which equals the noise level observed from frequency spectra) has been removed. The short-range sonar estimates shear, so its shear spectrum will have a white noise floor (as seen in Fig. 4.6). The short-range noise level subtracted in Fig. 4.15b corresponds to the level seen in Fig. 4.6.

Fig. 4.15 shows a spectral shape band-limited in wavenumber. As frequency increases, the wavenumber bandwidth decreases, with the center of the band moving to higher wavenumber (the 1-2 hour period energy is limited to 10-30 m wavelengths, while 4-8 hour periods broaden to 10-50 m bandwidth). The inertial period band (16-44 hr) is energetic throughout a 50-150 m bandwidth. The WKB-stretched spectrum (Fig. 4.8a) indicates that the actual inertial bandwidth may be closer to 50-80 m (assuming these inertial waves behave linearly). The clockwise inertial band also displays vertical asymmetry at low wavenumbers (Fig. 4.16), with the downward energy being twice that of the upward energy.

The counterclockwise spectra do not exhibit any strong vertical asymmetry, and tend to show a bandlimiting process that changes its wavenumber location with frequency. That is, 1-2 hour periods have 10-20 m bandwidth, while 16-44 hour periods have a 20-50 m bandwidth.

When the shear variance is integrated over all frequency bands, producing a cumulative wavenumber spectrum (Fig. 4.17), the end result is a vertical wavenumber spectrum energetic over 10-200 m vertical wavelengths, which agrees well with the observations of Gargett et al.(81). It is also seen that long wavelengths are dominated by inertial motions, with higher frequencies contributing more at high wavenumbers.

## 4.9    CTD Data : Vertical Strain

FLIP was instrumented with two CTD packages, one profiling between 0-300 m in depth, the other from 260-560 m. The drop rate was 3.8 m/s. A complete cycle was completed every three minutes. Sea-Bird Electronics CTD instruments were deployed, with $5\times10^{-4}$ mmho/cm, and $5\times10^{-4}$ °C resolution, corresponding to $5\times10^{-7}$ gm/cm$^3$ density precision. To avoid wake disturbances caused by the package itself, data were recorded only while the instruments were descending.

Salinity spiking was reduced by matching the conductivity time response characteristics to those of the temperature sensor. The method used was similar to Williams(85), and is outlined in App. D. Briefly stated, a low salinity-gradient region was chosen, such that the conductivity sensor was mainly responding to temperature. Cross-spectra were calculated between dC/dz and dT/dz, giving a phase and amplitude transfer function. This correction was applied to dC/dz for each profile. In addition, a low-pass filter having a 3 dB rolloff at ˜0.5 cpm was applied to both

dC/dz and dT/dz. Salinity, potential temperature, and potential density were then calculated for every profile.

The mean density profile for the PATCHEX cruise is given in Fig. 4.11a. A set of reference density values, separated by 1 m in depth in the mean profile, was chosen for subsequent isopycnal following. This set of density values defines 560 isopycnal surfaces, each uniquely identified by $\rho(\varsigma)$, where $\rho$ is its density, and $\varsigma$ is its mean depth. An isopycnal displacement can be defined as:

$$\eta(\varsigma,t) = Z(\rho(\varsigma)),t) - \varsigma \qquad (4.3)$$

where $Z(\rho,t)$ = depth of $\rho(\varsigma)$ at time t.

For comparison with shear spectral estimates, a subset of the CTD data was used. 512 twenty-one minute average estimates were computed in time, with $\varsigma$ spanning 150-406 m in depth, giving a 512x256 array. Computed displacements are shown in Fig. 4.13.

The strain field is fully described as a tensor, representing three-dimensional straining of all three components of the displacement field. The CTD data set only allows for an estimate of the vertical straining of the vertical displacement field, henceforth referred to as the vertical strain.

Vertical strain can be estimated from either an Eulerian approach (fixed depth reference frame), or a semi-Lagrangian method, where isopycnals are followed, and strain is estimated from the vertical separation between surfaces (Fig. C.1):

$$\eta_\varsigma(\varsigma) \equiv d\eta/d\varsigma = \frac{\eta(\varsigma+\delta\varsigma) - \eta(\varsigma)}{\delta\varsigma} \qquad (4.4)$$

where $\delta\varsigma$ = mean separation between isopycnals (= 1 m). The Eulerian definition of vertical strain is (c.f. App. C):

$$\eta_z \equiv d\eta/dz = \frac{1}{\overline{\rho_z}} \frac{d\rho'}{dz} \qquad (4.5)$$

where $\overline{\rho_z}$ = mean density gradient, and $\rho'$ = fluctuation density about its mean ($\rho(t)$ = $\overline{\rho} + \rho'(t)$ ). Thus $\eta_z$ represents the fractional change of the density gradient from its mean value.

$\eta_z$ can be expressed in terms of $\eta_\varsigma$ to first approximation as (Desaubies and Gregg(81), App. C):

$$\eta_z(z_o) = \frac{\eta_\varsigma(\varsigma(t))}{[1 + \eta_\varsigma(\varsigma(t))]} \qquad (4.6)$$

where $\eta(\varsigma(t))+\varsigma(t)$ = $z_o$. Note for small strain, $\eta_z$ = $\eta_\varsigma$. Also, (4.6) will fail when the mean density is not locally linear ($\eta_{zz}$ is no longer negligible). $\eta_z$'s temporal characteristics are determined by multiple $\varsigma$, since different isopycnals are advected past the fixed depth $z_o$ in time. The relation between $\eta_z(t)$ and $\eta_\varsigma(t)$ depends upon the correlation of $\eta_\varsigma(\varsigma)$ with depth, and how quickly $\varsigma(t)$ varies in time. Therefore, there is no simple translation between the frequency dependence of $\eta_z$ and $\eta_\varsigma$. Both $\eta_z$ and

$\eta_\varsigma$ were estimated for the PATCHEX data set, with time series shown in Fig. 4.14.

## 4.10 Vertical Strain Frequency-Wavenumber Spectral Estimates

Wavenumber-frequency spectra were computed for both $\eta_z$ and $\eta_\varsigma$, and are shown in Figs. 4.18 and 4.19. $\eta_z$ and $\eta_\varsigma$ differ most strongly at high wavenumber, where $\eta_z$ exhibits the same band-limited behavior as the shear spectrum. The semi-Lagrangian spectrum shows the near-inertial band rolling off with a $m^{-3/2}$ slope in wavenumber at 10 m scale, while the higher frequencies are more nearly white in wavenumber. The question then arises on which spectrum most truly represents the actual oceanic field. $\eta_\varsigma$ estimates are not contaminated by vertical advection of finestructure, and should be more accurate (although both will still be contaminated by horizontal advection effects). It is worthwhile to better quantify the spectral response to finestructure contamination.

## 4.11 Finestructure Contamination of a Generalized Background Field

Finestructure contamination of a fixed-depth sensor has been addressed by many authors (e.g. Phillips(71), Garrett and Munk(71), and McKean(74)). It is typically assumed that the finestructure field behaves like a 'sheet and layer' model, exhibiting a Poisson probability distribution. However, Desaubies and Gregg(81) have pointed out that observations of 'sheet and layer' finestructure may just be an artifact of internal wave straining. The approach here is to model the finestructure as some background spatial field $\Theta$ which can be represented by its Fourier components:

$$\Theta(x,y,z) = \sum_{i=1}^{M} \Theta_i \sin(\alpha_i x + \beta_i y + m_i z + \phi_i) \tag{4.7}$$

where $\alpha_i$ and $\beta_i$ are the corresponding wavenumber components for the x and y directions, and $\phi_i$ is some random phase.

An observer at a fixed position $\bar{x}_o = (x_o, y_o, z_o)$ will see $\Theta$ being advected by internal waves, with a velocity field $\bar{U}(\bar{x}_o) = (u,v,w)$. At any time t, the amount of advection will be:

$$x(\bar{x}_o, t) = \int_0^t u(\bar{x}_o, t) dt$$

$$y(\bar{x}_o, t) = \int_0^t v(\bar{x}_o, t) dt \tag{4.8}$$

$$z(\bar{x}_o, t) = \int_0^t w(x_o, t) dt \quad (=\eta(\bar{x}_o, t)).$$

This assumes that straining of $\Theta$ by the internal wave field is minimal. This is not realistic at high wavenumbers (where measured strain is large), but does allow for easy simulation. It will also be assumed that $\alpha = \beta$, with $\alpha^2 + \beta^2 = k^2$, and that the aspect ratio $\delta \equiv \alpha/m$ is constant $<< 1$. (4.7) reduces to:

$$\Theta(\overline{x}_o, t) = \sum_{i=1}^{M} \Theta_i \sin[m_i(z(t) - z_o + \delta(x(t) - x_o + y(t) - y_o)) + \phi_i]. \qquad (4.9)$$

Velocity estimates from the long-range sonar, coupled with vertical displacements measured from the CTD system (both averaged over 60 m in depth), were substituted into (4.8) to estimate the advected distances expected at 150 m depth. Rms advected distances were 500 m in the horizontal, and 6 m in the vertical. The time series from (4.8) were substituted into (4.9), along with assuming $\Theta_i$ = constant, to simulate the observed background signal. Forty vertical wavenumber components were used, varying from 0.01-.4 cpm, in 0.01 cpm increments. $\Theta$ was Fourier transformed in $(\omega, m)$ space, and summed into frequency bands, such that the display is similar to Fig. 4.15. The results are shown in Fig. 4.20 for $\delta$ = 1/25, and 1/100. At low vertical wavenumbers, $\Theta$'s variance is mainly comprised of low frequency motions. As $m$ increases, more high-frequency contamination is observed. At high wavenumbers, $\Theta$ appears white in frequency.

The cumulative wavenumber spectrum (variance integrated from 1 to 44 hour periods) demonstrates that the observed $\Theta$ is attenuated only at low wavenumbers. The amount of low-wavenumber attenuation is dependent on the aspect ratio. If the high-wavenumber variance of the shear spectrum is solely due to finestructure contamination, then $\Theta_i(m)$ must have the same cumulative spectral shape and energy level as shown in Fig. 4.17. The finestructure vertical wavenumber spectrum was modeled with $m^0$ slope out to 0.07 cpm, and $m^{-1}$ slope at higher wavenumbers. Results are shown in Fig. 4.20c for $\delta$ = 1/100, along with the measured shear spectrum from Fig. 4.15. Both spectra agree well for $m > 0.06$ cpm.

By not allowing any vertical displacement, the effects of only horizontal advection can be explored. Calculations were repeated with the same input spectrum used in Fig. 4.20c, and $\delta$ = 1/100. Results are displayed in Fig. 4.20d. Comparison with the semi-Lagrangian strain spectrum (Fig. 4.19c) shows disagreement over all wavenumbers. This could result from finestructure strain variance being much less than the finestructure shear variance. This would imply that the Eulerian strain spectrum should also show less contamination. The similarities between the Eulerian strain and shear spectral shapes tend to contradict this argument, although absolute energy levels must also be considered. This can be further clarified by investigating relationships between shear and strain, and comparing with predictions from linear internal wave theory.

## 4.12   Consistency Tests of Linear Theory

Linear internal wave theory predicts that the shear and strain variance should be related by (App. C):

$$\Psi(\omega) \equiv \frac{N^2 \eta_z^2}{U_z^2} = \frac{(\omega^2 - f^2)}{(\omega^2 + f^2)} \frac{N^2}{(N^2 - \omega^2)}, \qquad (4.10)$$

where $U_z^2$ = $(\partial u / \partial z)^2 + (\partial v / \partial z)^2$ = vertical shear variance. Let $\Phi(\omega, m)$ equal the measured ratio of $N^2 \eta_z^2 / U_z^2$, such that $\Phi / \Psi$ indicates how well the observed field agrees with linear theory. Estimates were computed over the same frequency bands as in Fig. 4.15, and averaged over eight different wavenumber bands. Results are shown

in Fig. 4.21, using both $U_z$ with and without modeled noise removed. It is seen that at low wavenumbers (>100 m scales) there is fair agreement with linear theory. $\eta_z$ slightly overestimates the amount of strain expected by linear theory in the near-inertial band over all wavenumbers, while underestimating at all other frequenci s at higher wavenumbers. This underestimation indicates that the observed motions have less strain per unit shear than linear theory predicts. For linear theory to be correct, this implies that the high-frequency waves observed include lower fre-quency waves (or perhaps vortical mode) that have been advected past the sensor by the large scale field. If range-aliasing has attenuated the observed shear vari-ance by 40%, then the true strain/shear ratios will be 40% lower than shown in Fig. 4.21, and disagreement with linear theory is even greater.

Another consistency test is to compare clockwise(cw) and counterclockwise(ccw) variances from the rotary spectra. Linear internal wave theory predicts (c.f. Muller et al.(78)):

$$\frac{ccw}{cw} = \left[ \frac{\omega - f}{\omega + f} \right]^2. \tag{4.11}$$

Measured values are shown in Fig. 4.22, where it is seen that at high wavenumber (>1/64cpm), near-inertial waves exhibit nearly a magnitude more counterclockwise variance than expected. For the ccw/cw ratio and linear internal wave theory to be correct, this would imply high-frequency waves are being Doppler-shifted to near-inertial frequencies, while near-inertial waves (which have a strong sense of rota-tion) are not Doppler-shifted to high frequencies. For this result to agree with the above $\eta_z/U_z$ measurements, the extra shear variance seen at high frequencies must come from vortical-mode contamination, while the strain seen at the inertial fre-quency at high wavenumbers must be mainly comprised of high-frequency strain Doppler-shifted to near-inertial frequencies. It is worthwhile to consider the effect of vertical advection on rotary spectral estimates.

Consider a rotary velocity field defined by M inertial waves of varying verti-cal wavenumber being observed at a fixed depth $= z_o$:

$$(u+iv)(z_o,t) = \sum_{j=1}^{M} A_j e^{i(m_j z(\overline{x}_o,t) - ft + \phi_j)} \tag{4.12}$$

where $z(\overline{x}_o)$ is the vertical advection displacement, as defined in (4.8), f $=$ Coriolis frequency, and $\phi_j$ is some random phase. It is seen that if $m_j dz/dt > f$, then the observed rotational sense will be counterclockwise instead of clockwise. (4.12) was modeled using $z(\overline{x}_o)$ averaged over 60 m in depth, $A_j$ equal for all j, and $m_j$ ranging from 1/512-1/16 cpm (M$=$64 components). This simulated time series was pro-cessed in the same manner as the actual shear data, with the modeled ccw/cw ratio shown in Fig. 4.22. Results suggest that the measured ccw/cw ratios are contam-inated at high wavenumbers by vertical advection, and therefore do not serve as a good indicator of linear theory, and should not be used as a cross-check with the strain/shear consistency test.

## 4.13    Shear Spectral Models

Given that the wavenumber-frequency spectrum of Fig. 4.15 is contaminated by smaller-scale waves Doppler-shifted to different encounter frequencies, it is

worthwhile to try to reconstruct the 'actual' spectrum. One approach is to assume that $\eta_\zeta$ is a correct representation of the strain field, and that the linear prediction $\Psi$ is accurate, allowing $U_z$ to be calculated from (4.10). This 'semi-Lagrangian equivalent' shear spectrum is shown in Fig. 4.23c, and reflects the $\eta_\zeta(\omega,m)$ spectrum. There are two faults to this approach. Since $\eta_\zeta = 0$ when $\omega = f$, the true amount of inertial shear will be underestimated, even if the spectrum of $\eta_\zeta$ is absolutely accurate. Furthermore, if the observed $\eta_\zeta$ spectrum has high-frequency strain Doppler-shifted to near-inertial frequencies, then this will mistakenly lead to an overestimate of near-inertial shear. The 'semi-Lagrangian' shear spectrum does not provide the truth, but merely an alternative view, which is hopefully less contaminated by the vertical advection of finestructure.

Another approach is to assume that the measured ratio $\Phi(\omega,m)$ can be modeled as:

$$\Phi(\omega,m) \approx \frac{N^2 \eta_z^2(\omega,m)}{U_z^2(\omega,m) + F(\omega)U_z^2(f,m)} \qquad (4.13)$$

where $F(\omega)$ is the fraction of the inertial band Doppler-shifted to frequency $\omega$. (4.13) states that the measured $\eta_z$ is correct, and that the measured $U_z$ is comprised of both the true amount of shear for $\omega$, plus an inertial component (where $\eta_z = 0$) which has been Doppler-shifted to $\omega$ by advection. Since $\eta_z(\omega)/U_z(\omega)$ can be computed from $\Psi$ (again assuming linear theory), $F(\omega)U_z^2(f)$ and $U_z^2(\omega)$ can be calculated, allowing reconstruction of the 'uncontaminated' spectrum. This technique removes the 'extra' observed shear variance from the high frequency bands and redistributes it into the near-inertial band (thus retaining the same cumulative spectrum). Results are shown in Fig. 4.23e. By assuming all 'contamination' is from near-inertial waves, Fig. 4.23e overestimates actual inertial energy, while underestimating other frequency components (which will also be Doppler-shifted). This can be viewed as the 'extreme inertial' spectrum. In actuality, the near-inertial band stays within a factor of two of the 'semi-Lagrangian' spectrum. The tidal frequency band begins to disagree at 50 m scale, with higher frequency bands deviating at even larger scales. This might be the result of the 'extreme inertial' model not redistributing energy into mid-frequency bands.

Both the 'semi-Lagrangian', and 'extreme inertial' spectra have assumed a linear relationship between $\eta_z$ and $U_z$. This will be correct for weak nonlinearities, where waves still behave linearly, although energy is being transferred to other wavenumbers and frequencies. However, this will not be the case for strongly nonlinear motion, where the relationship between strain and shear is unclear.

## 4.14 Richardson Function Estimates

An inverse Richardson Function (IRF) can now be calculated in the spirit of Munk(81) and Pinkel(85), where:

$$\text{IRF}(\omega,m) = \frac{1}{N^2} \int_0^m \int_0^\omega \phi(\omega,m) \, d\omega \, dm \qquad (4.14)$$

and $\phi(\omega,m)$ is the shear spectral density at frequency $\omega$ and vertical wavenumber $m$. IRF is simply the integrated shear variance measured over a specified frequency and

wavenumber range normalized by the Vaisala frequency. An average Vaisala frequency value of 5.3 cph was used, based on the value derived from the CTD data set. IRF was calculated across the increasing frequency bands, and plotted in Fig. 4.24 using the three different shear spectra shown in Fig. 4.23. Results show that up to 1.4 cph and 3 m scales, IRF = 0.7-0.9. Both the 'extreme inertial' and 'semi-Lagrangian' spectral models show approximately half the variance in the inertial frequency band. In contrast, the Eulerian spectrum shows high frequencies contributing most of the variance at high wavenumbers.

Since frequency estimates only go up to 1.4 cph, it is difficult to estimate the total shear variance expected over all frequencies. An imprecise estimate is attempted with the Eulerian spectrum by extrapolating the curve out to the Vaisala frequency. $d(IRF(m))/d\omega$ is linearly extrapolated out to 5.3 cph. Beyond 0.3 cpm, it is assumed that $\phi(m)$ has a $m^{-1}$ slope, such that

$$IRF(m)=\ln(m)+C_o.$$

where $C_o$ is chosen to match the value at 0.3 cpm. It is seen that $IRF(N,m) \approx 1$ at 0.2 cpm, and approaches $IRF=4$ at $m \approx 2-4$ cpm, corresponding to a vertical scale of 1/4-1/8 m. Since this extrapolation uses the shear spectrum with no noise removal, it overestimates IRF at high wavenumbers.

The extrapolated high-frequency variance corresponds to computing more inertial variance in the 'extreme inertial' model, with the end result being both spectra having the same $IRF(N,m)$ curve (simply by energy conservation being enforced upon the model). The 'semi-Lagrangian' IRF can only agree with the above if more inertial variance is added, since any other frequency would require more $\eta_c$ to have been observed in other frequencies (assuming linear theory). Both of these extrapolated models would still predict that the near-inertial shear contributes most of the total variance at fine scales.

## 4.15 Discussion

Garrett and Munk's spectral model assumes that the wavenumber spectral shape is independent of frequency. This is certainly not the case for the Eulerian spectrum, but is a more appropriate description of the 'semi-Lagrangian' spectrum for $m < 0.1$ cpm, and the 'extreme inertial' spectrum for $m < 1/50$ cpm. This is more apparent when the different wavenumber bands are viewed in frequency (Fig. 4.23b,d,f), where the semi-Lagrangian spectrum has nearly $\omega^{-2}$ slope for all wavenumber bands.

The frequency-integrated wavenumber spectrum (Fig. 4.17) agrees well with the Gargett et al.(81) model. The spectrum begins to roll off at a 15-20 m scale ($m_c \approx 0.5-0.7$ cpm), with a $m^{-1}$ to $m^{-2}$ slope at higher wavenumbers, depending upon the noise correction scheme. This compares with their estimated values of $m_c$ = 0.1 cpm, with a $m^{-1}$ high-wavenumber slope. The measured spectrum also suggests that a low-wavenumber rolloff for $m<0.01$ cpm should be included. The estimated inverse Richardson Function at the cutoff scale is $\approx 0.3$. This does not support the Gargett et al. hypothesis that $IRF(m_c)$ = 1, but is more in line with Munk's(81) prediction of $IRF(m_c)$ = 0.5. Both the Eulerian and semi-Lagrangian spectra suggest that $m_c$ is frequency-dependent, with higher frequencies cutting off at higher wavenumbers.

McComas and Muller(81) predict a shear spectral shape with a $m^{+1}$ slope out to some cutoff wavenumber, and an $\omega^{-1}$ dependence in frequency, assuming weak-

interaction theory (weak nonlinear resonant interactions). The Eulerian spectrum has an $m^{+1}$-$m^{+2}$ slope for $m < 0.01$-$0.05$ cpm, depending upon the frequency band. The frequency dependence varies between $\omega^{-2}$ and $\omega^{-1}$ for $m < 0.05$ cpm. The semi-Lagrangian and extreme-inertial spectra have a $m^{+1}$ slope only for the inertial band for $m < 0.01$ cpm. They display an $\omega^{-2}$ slope for $m < 0.01$ cpm. This might be an indication that the parametric subharmonic instability (PSI) mechanism is affecting near-inertial waves for $m < 0.01$ cpm, with stronger nonlinearities being more important at higher wavenumbers and frequencies. The PSI mechanism describes the interaction between an internal wave and two higher wavenumber waves with half the original frequency. PSI transfers energy into the high-wavenumber, near-inertial band.

It is of interest to investigate the effect of caustic zones and critical layers. A critical layer occurs when the background flow velocity equals the horizontal phase speed of the internal wave ($U(z) = \omega/k$). As a wave approaches the critical layer, refraction occurs, causing a shift to higher vertical wavenumber, a lower intrinsic frequency (the frequency as measured relative to the background flow), and a focusing of the energy.

When the background flow is from another internal wave (referred to as the 'background' wave), a 'caustic zone' is a more appropriate parameterization. A 'caustic' is a term from ray theory which describes the condition when neighboring rays cross, invalidating the slow-variation principles originally assumed. This occurs when the vertical group velocity of the 'smaller' wave ($\equiv C_g(\text{small})$) equals the vertical propagation speed of the background wave ($\equiv C_\partial(\text{large})$), with the result being amplitude intensification of the smaller wave while it is being refracted through the caustic (Broutman(86)).

Broutman(86) investigates the effects of a 'small' (high wavenumber) internal wave propagating through a large-scale background inertial wave. Broutman defines $\hat{\omega}$ as the intrinsic frequency of the small wave, as measured relative to the background velocity field. $\Omega$ is defined as the frequency measured by an observer moving at a vertical velocity $= C_\partial(\text{large})$ (so the background inertial wave appears stationary), such that $\Omega$ remains constant (the observer has no horizontal velocity). The intrinsic frequency measured along a ray is given by:

$$\hat{\omega} = \Omega - kU + mC_\partial(\text{large}) \tag{4.16}$$

where k and $m$ are the horizontal and vertical wavenumber of the small wave. $\hat{\omega}$, k, and $m$ are related to each other through the linear dispersion relationship of (4.1). For mid-frequencies ($f \ll \hat{\omega} \ll N$), $C_g(\text{small})$ is equal to $-\hat{\omega}/m$, and $\hat{\omega} = Nk/m$ (Broutman shows this is a reasonable assumption for $2f < \hat{\omega} < N/2$). The condition that $C_g(\text{small}) = C_\partial(\text{large})$ leads to the expected vertical wavenumber at the caustic ($\equiv m_{ca}$) occurring at a background velocity $U_{ca}$, where:

$$m_{ca} = (Nk/C_\partial(\text{large}))^{\frac{1}{2}}, \quad U_{ca} = \Omega/k - 2(NC_\partial(\text{large})/k)^{\frac{1}{2}} . \tag{4.17}$$

The condition that the rms velocity of the background wave $\equiv U_{rms} = \Omega/k$ insures that caustics will occur, independent of $C_\partial(\text{large})$. For no background wave present, $\Omega = \hat{\omega}$, and for mid-frequencies, $\hat{\omega}/k = N/m$. Let $m_0$ equal the vertical wavenumber before distortion by the background wave. Caustics are guaranteed of occurring when:

$$U_{rms} \geq \Omega/k = N/m_0 \quad \text{for } f \ll \Omega \ll N. \tag{4.18}$$

Let $\phi(m)$ denote the shear spectrum, so that the velocity spectrum is estimated from $\phi(m)/m^2$. The velocity variance can be calculated from:

$$U_{rms}^2(m) = \int_0^m \phi(m)/m^2 \, dm \qquad (4.19)$$

where $U_{rms}(m)$ = rms velocity associated with all scales larger than $m^{-1}$. By using the shear wavenumber spectrum from PATCHEX, Fig. 4.25 is obtained, which shows $U_{rms} \approx 6$ cm/s for $m > 1/50$ cpm. This indicates that caustics will occur for $m_o > 1/40$ cpm at N = 5.3 cph. (4.18) is the same criterion Holloway(80) used to define when strong nonlinearities are to be expected, so it is not surprising that the results agree.

As the caustic is approached, energy is amplified, such that there will be a peak at $m_{ca}$. If $m_{ca}$ is expressed in terms of the undistorted vertical wavelength $(m_o)$, (4.17) reduces to:

$$m_{ca} = (\Omega m_o / C_\partial(\text{large}))^{\frac{1}{2}} . \qquad (4.20)$$

The value of $m_{ca}$ should increase by $\Omega^{\frac{1}{2}}$ (assuming $m_o$ = is frequency independent). Using the bandwidth peak of the 2-4 hour period band of the semi-Lagrangian spectrum, peaks for the other frequencies are computed from (4.20) and plotted on Fig. 4.23c. Good agreement is seen. Broutman and Young(86) argue that, for the strength of the oceanic background velocity field, a much broader band of waves interact, and the peak will no longer be centered about $m_{ca}$. The $\omega^{\frac{1}{2}}$ response of the spectral peak therefore may not be the result of caustic interactions.

Broutman(86) indicates that wave breaking due to amplification at a caustic is not considered likely if the initial wave is not already close to breaking. Since IRF < 1 for $m < 0.2$ cpm, it is not clear what the final role caustic zones play in internal wave energy dissipation. Given a broad-band background wave field with random caustic zone locations, short wave propagation ($m > 1/40$ cpm) might best be modeled as a random-walk phenomena, similar to Cox and Johnson's(79) diffusion model caused by triad interactions. At 0(5 m) scales, where IRF approaches unity, caustics may cause enough amplification to create 'whitecapping' events, with more complete mixing occurring at smaller and smaller scales. This suggests the typical 'saturation' model, such as proposed by Munk(81), where the shear magnitude controls dissipation, and thus the total energy level of the internal wave spectrum.

## 4.16   Summary

Vertical shear data were analyzed from two different Doppler sonars covering 3-600 m vertical range. Vertical wavenumber shear spectra display band-limited energy between 10-50 m wavelengths which narrows at higher frequency bands. The shear spectrum was compared with estimates of vertical strain from CTD data covering 256 m in depth. Vertical strain was estimated from both a fixed-depth reference frame (Eulerian $\equiv \eta_z$), and a semi-Lagrangian viewpoint, where strain was estimated following isopycnals ($\equiv \eta_\ell$). The Eulerian strain spectrum exhibits the same characteristics as the shear spectrum, whereas the semi-Lagrangian spectrum is quite different.

This discrepancy led to an investigation of spectral contamination caused by advective Doppler-shifting of the signal by the low-wavenumber internal wave

field. Computer simulation of a background field with a $m^{-1}$ dependency for $m >$ 0.07 cpm, and $m^0$ slope for $m < 0.07$ cpm produced a spectral shape similar to the Eulerian spectrum at high wavenumbers. Calculations of the same spectral model contaminated only by horizontal advection estimated a spectrum which differs from the measured semi-Lagrangian strain spectrum. If this difference is due to fines- tructure strain having less variance than finestructure shear, then the Eulerian strain spectrum should also show less contamination. However, the observed spec- tral shapes of both spectra are similar.

Linear internal wave theory predicts a vertical strain/shear ratio dependent upon frequency. The estimated ratio from the measured data show more shear vari- ance than expected at high frequencies and wavenumbers. The observed motions are either not linear internal waves, or the Eulerian spectrum is contaminated by waves Doppler-shifted by the low-wavenumber internal wave field. An attempt to compare counterclockwise/clockwise shear variances was found to be unsuccessful at high wavenumbers due to vertical advection contaminating the sense of rotation in time. It remains ambiguous whether the extra high-frequency shear variance is from a Doppler-shifted inertial wave, or some high-shear, low-strain finestructure, being advected past the sensor.

Two other spectral estimates are made assuming that the linear theory's strain/shear ratio is correct, even though nonlinearities are expected at high wavenumbers. The 'extreme inertial' model assumes that the measured shear spec- trum is contaminated by inertial waves, while the $\eta_z$ spectrum is correct (since Doppler-shifted inertial waves have $\eta_z = 0$). The amount of contamination is com- puted, and added to the inertial band. This model overestimates the amount of near-inertial energy. The 'semi-Lagrangian' spectral model assumes that the $\eta_\zeta$ spec- trum is correct, and uses linear theory to estimate the shear spectrum. Since $\eta_\zeta = 0$ at the inertial frequency, the semi-Lagrangian model cannot accurately estimate the inertial shear variance. Both models incorrectly assume that none of the observed near-inertial strain is from high frequency waves Doppler-shifted to the inertial fre- quency. The two models actually agree well for the inertial band, and disagree at progressively higher wavenumbers with higher frequency. The Eulerian, semi- Lagrangian, and extreme-inertial spectra provide three different perspectives cf the vertical wavenumber shear spectrum, with each view suffering from its own set of deficiencies.

Estimates of an Inverse Richardson Function(IRF) based on the semi- Lagrangian spectral model show half of the shear variance is from near-inertial waves, even at high wavenumbers. This would enable low Richardson number regions to persist for inertial period time scales, possibly leading to mixing patches which show activity over inertial time periods, as observed by Gregg et al.(86). A simplistic extrapolation of IRF out to the Vaisala frequency and high wavenumbers suggest Ri = 1/4 on a 1/4-1/8 m vertical scale.

The frequency-integrated wavenumber spectrum compares well with the Gargett et al.(81) model. It is white out to 16 m scale, and then rolls off with a $m^{-1}$ to $m^{-2}$ slope, depending upon how noise and finestructure contamination are modeled. However, the cutoff wavenumber (1/16 cpm) occurs at a IRF $\approx 0.3$, not 1, as suggested by Gargett et al.(81), implying that the Richardson number is not the deciding factor on where the spectrum begins to roll off.

Investigation of caustic zones indicate that caustics should occur for $m$ $> 1/40$ cpm scales. The semi-Lagrangian shear spectrum demonstrates an $\omega^{1/2}$ spec- tral peak dependence. Broutman's(86) formula for the caustic wavenumber also has

a $\omega^{\frac{1}{2}}$ dependence. This may be purely coincidental, since Broutman and Young(86) argue that the formula is not valid for the typical strength of the oceanic velocity field.
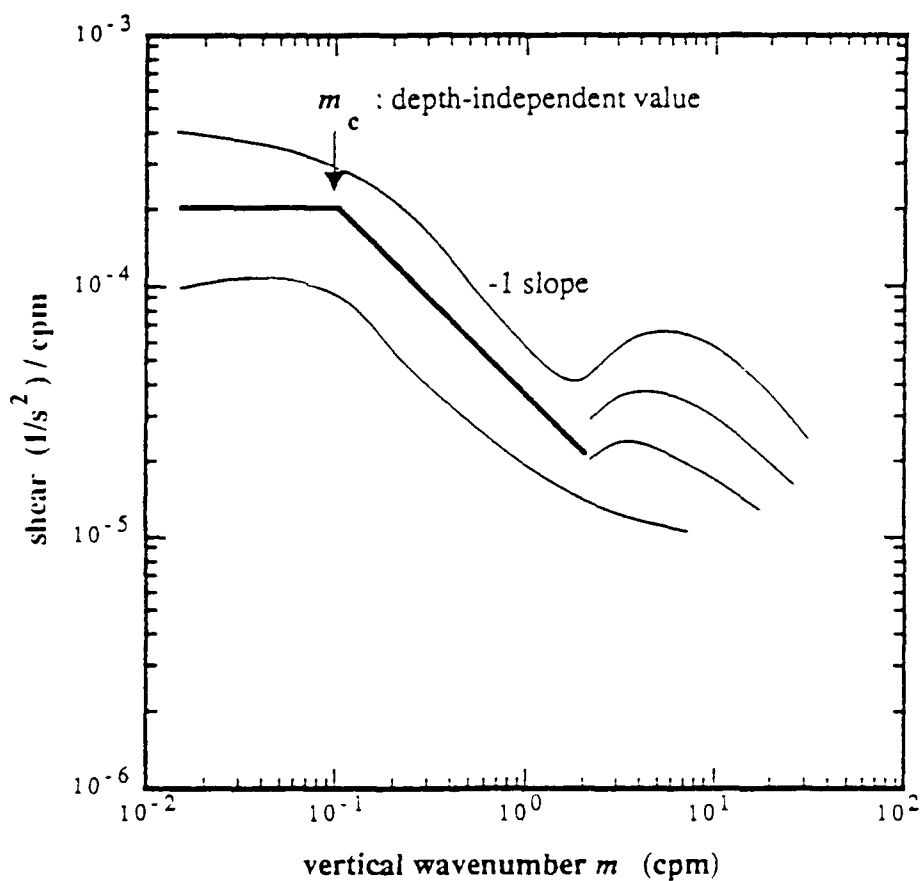
**Figure 4.1.** Gargett et al.(81) based a universal shear spectral model on measurements from the FAME experiment. The $m^0$ slope at low wavenumbers has its energy level scale in a WKB fashion as $N^2$. The break in slope at $m_c \approx 0.1$ cpm is thought to be a depth-independent parameter occurring when IRF($m_c$) = 1. The $m^{-1}$ slope is then followed by an intermittent high-wavenumber region, dependent upon mixing events.
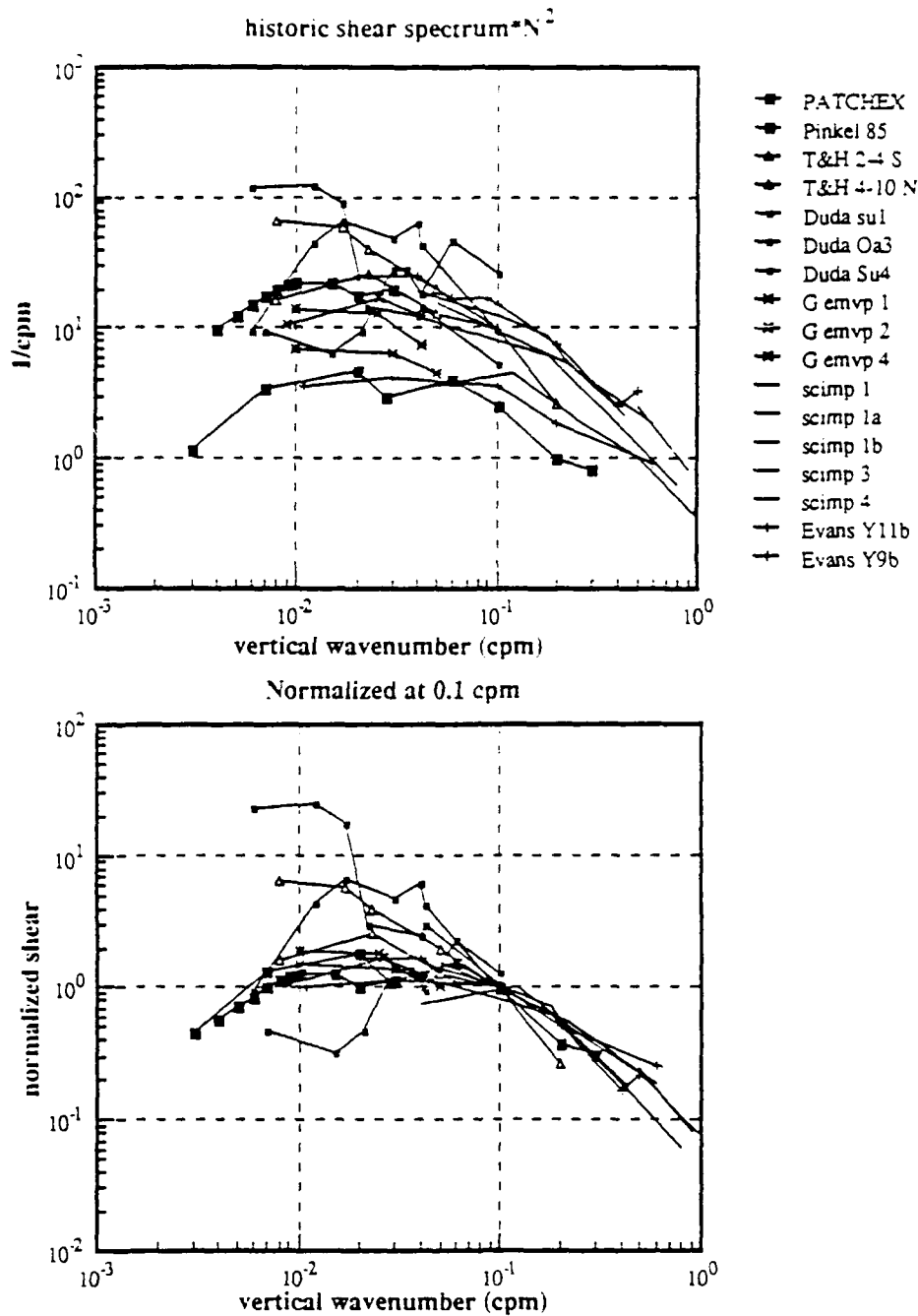
**Figure 4.2.** a) is a composite of available shear spectra from the literature. Included is Gargett et al.(81) original data set from the FAME cruise. Toole and Hayes(84) measurements are near-equatorial. Evans(82) is also from the FAME cruise. Pinkel(85) is from the same location as the PATCHEX cruise. Duda's(86) measurements are from three different locations off the Southern California coast. PATCHEX marks the results outlined in this chapter. Data has been normalized by the given Vaisala frequency for each site. b) is the same data set, now arbitrarily normalized so that the energy level is the same for all spectra at 0.1 cpm.
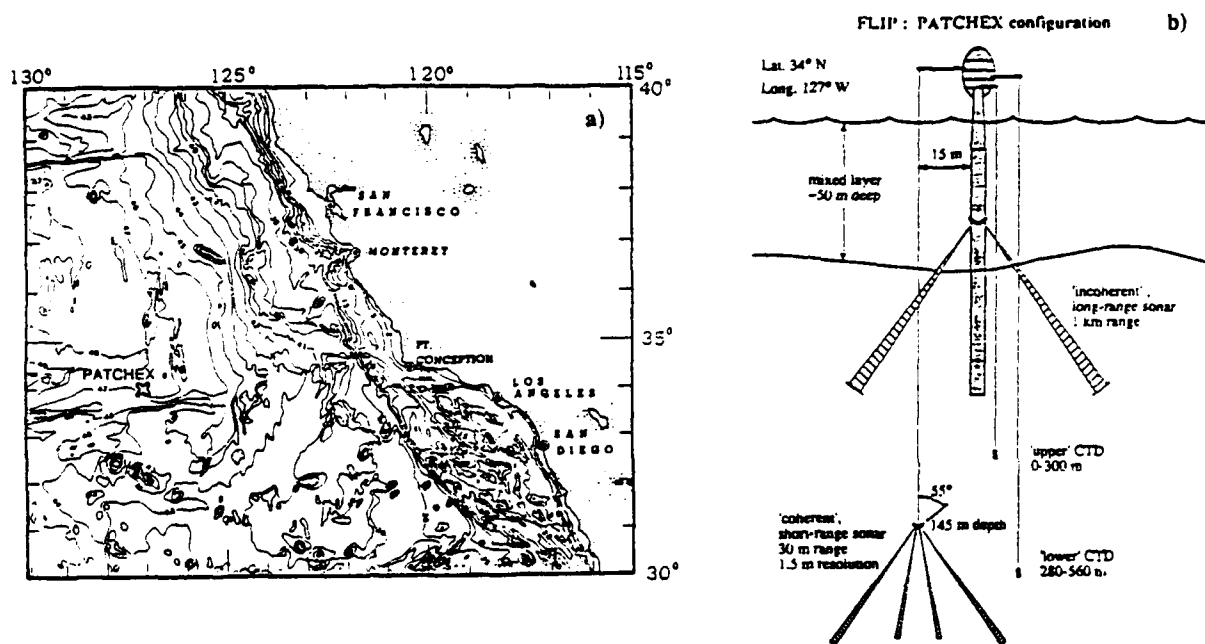
**Figure 4.3.** a) The PATCHEX 1986 cruise was located at 34° N, 127° W. b) FLIP was config-ured with two rapid profiling CTD's, a Janus-configured long-range incoherent sonar, a Janus-configured short-range coherent sonar, and two surface wave/mixed layer sonars (not shown).
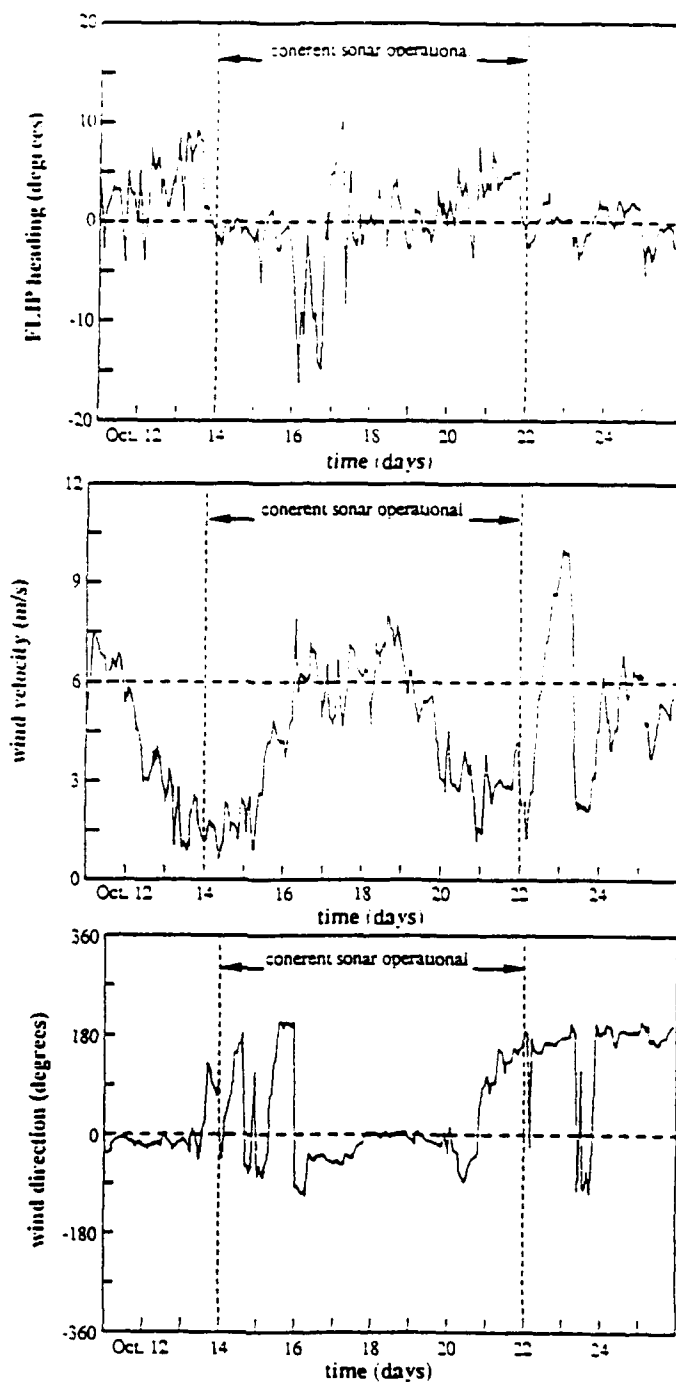
**Figure 4.4.** FLIP's heading, wind speed, and wind direction are shown for the PATCHEX cruise. Highlighted are the 7.5 days when the short-range (coherent) sonar was operational. Figures are courtesy of Chuck Lumbardo of University of Washington.
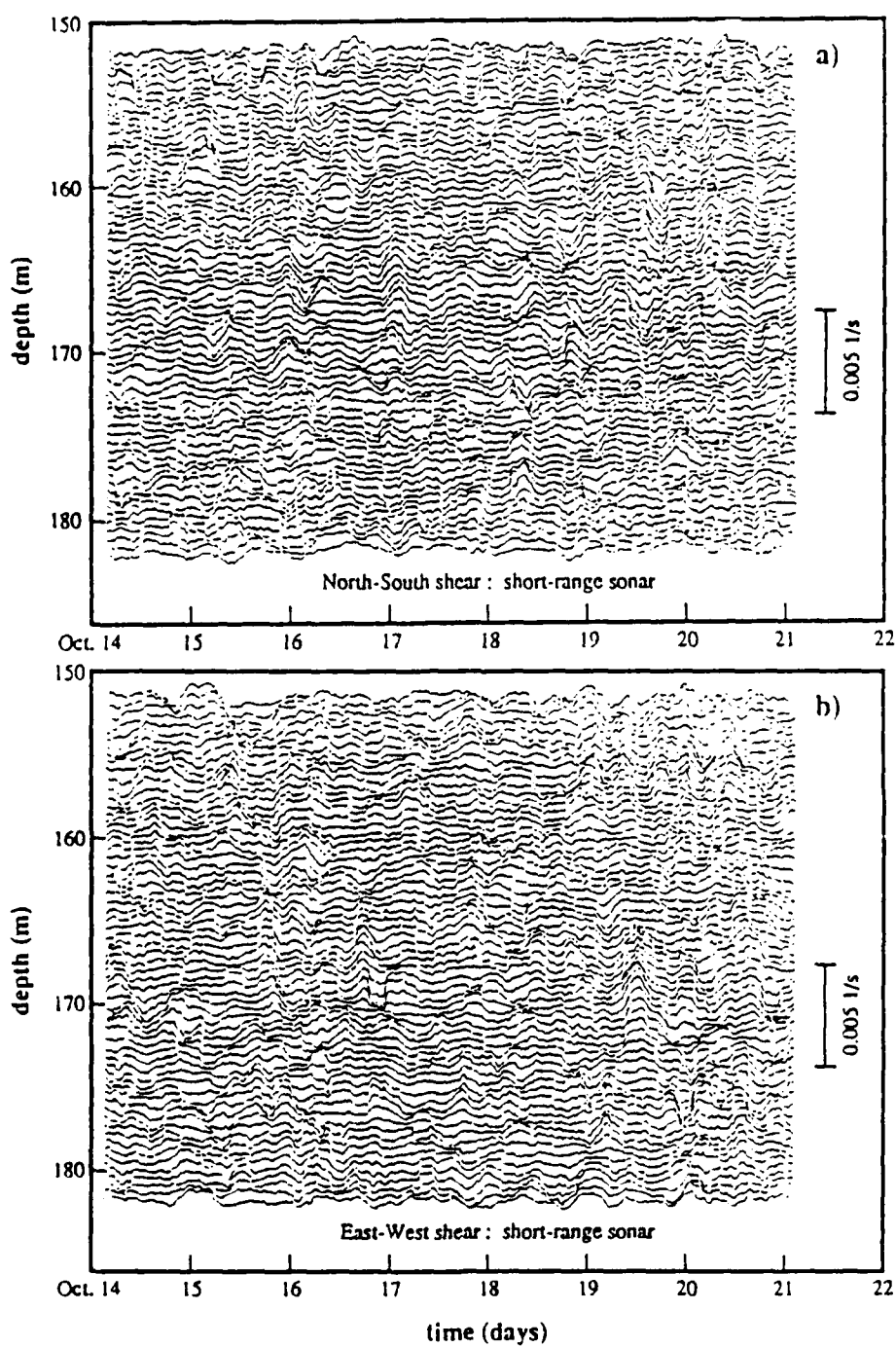
**Figure 4.5.** Shear estimates from the short-range sonar were recorded for a 7.5 day period. The plotted data set has a running-mean-filter of 4 hours applied. a) is the shear component in the N-S direction, and b) is the E-W component.
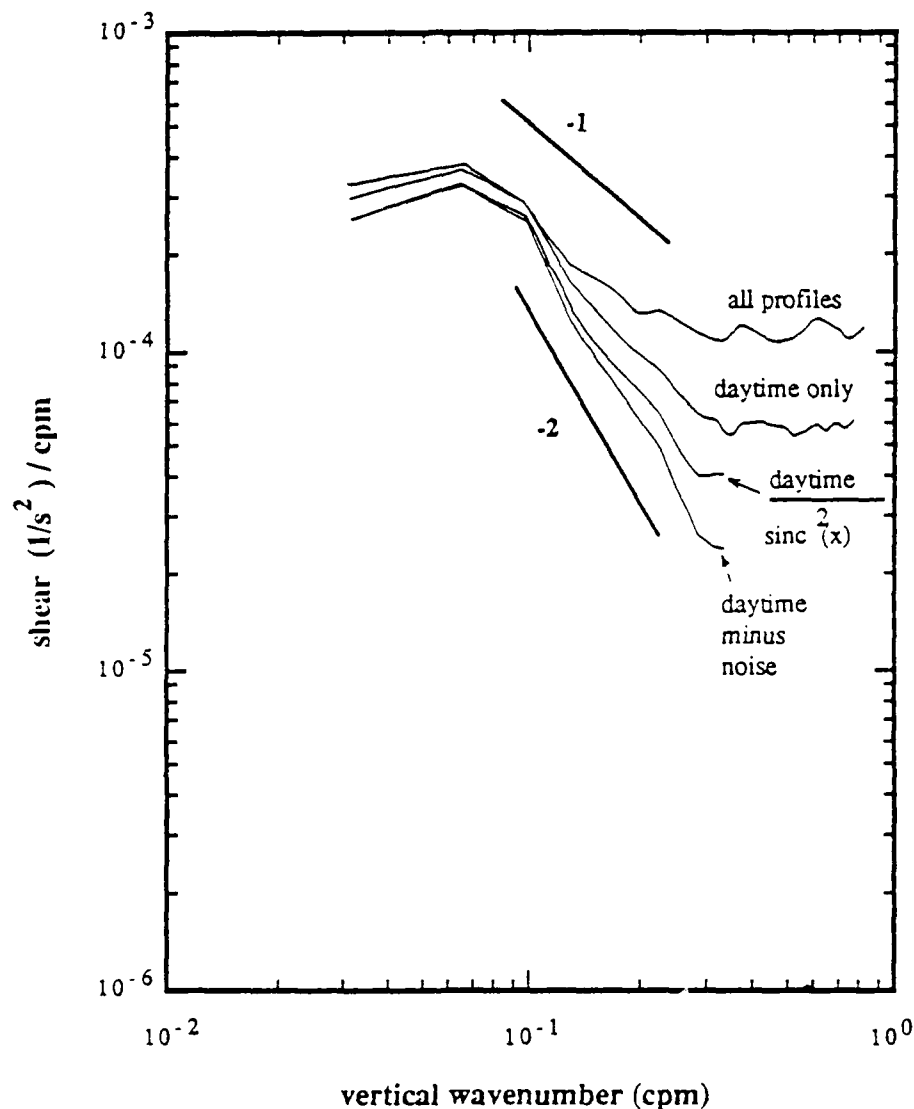
**Figure 4.6.** Vertical wavenumber spectral estimates are computed from the short-range sonar. The 'all profiles' curve is computed from all 512 profiles during the 7.5 day time period. 'Daytime profiles' is comprised of the daytime-only profiles, between the day/night migration times. 'Daytime minus noise' is based on the daytime curve minus a modeled white-noise floor level. This has been further corrected for vertical advection by applying a boxcar filter of width 1.2 m (1.2 m = rms vertical displacement on a 20 minute time scale), represented by the 'daytime/$\sigma^2_{inc}(x)$' line.
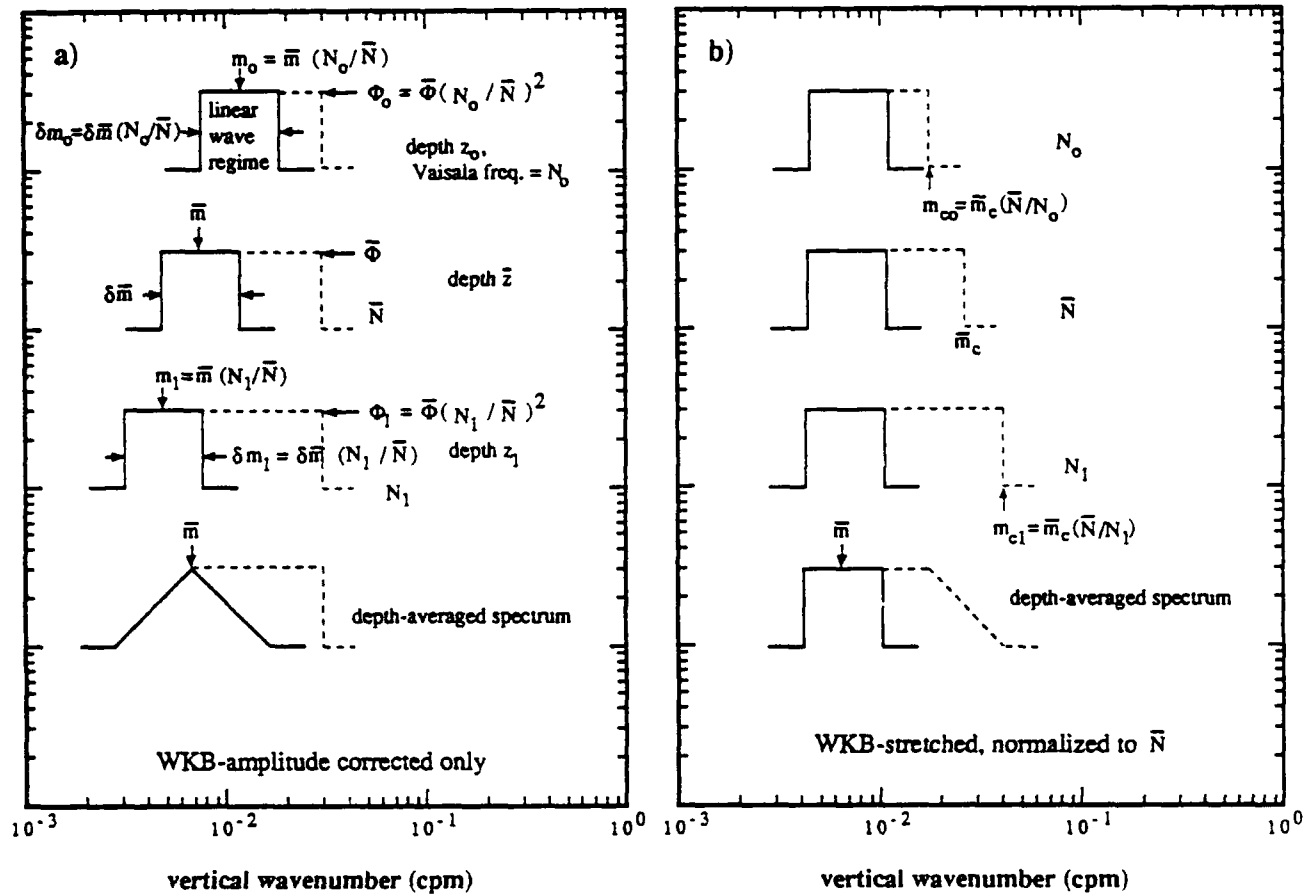
**Figure 4.7.** a) The vertical wavenumber shear spectrum is comprised of both a linear (solid line) and nonlinear regime (dashed line). Gargett et al. hypothesize that the high-wavenumber cutoff is depth-independent, with the nonlinear regime's spectral density scaling as $N^2$. The long-range sonar's 0.03 cpm low-pass filter forces this to be the case. The linear regime has a spectral energy level that varies as $N^2$, and wavenumber that scales as N. As N decreases, the linear band moves to lower wavenumbers. The depth-average spectrum has the linear band centered at the average N wavenumber value, and accurately depicts the high wavenumber cutoff. The linear band's shape has been distorted. b) If the spectra in a) are WKB-stretched, so that the linear regime has the same bandwidth and center wavenumber at all depths, then the high-wavenumber cutoff becomes variable. The depth-average spectrum accurately estimates the linear band, but has now distorted the high-wavenumber cutoff.
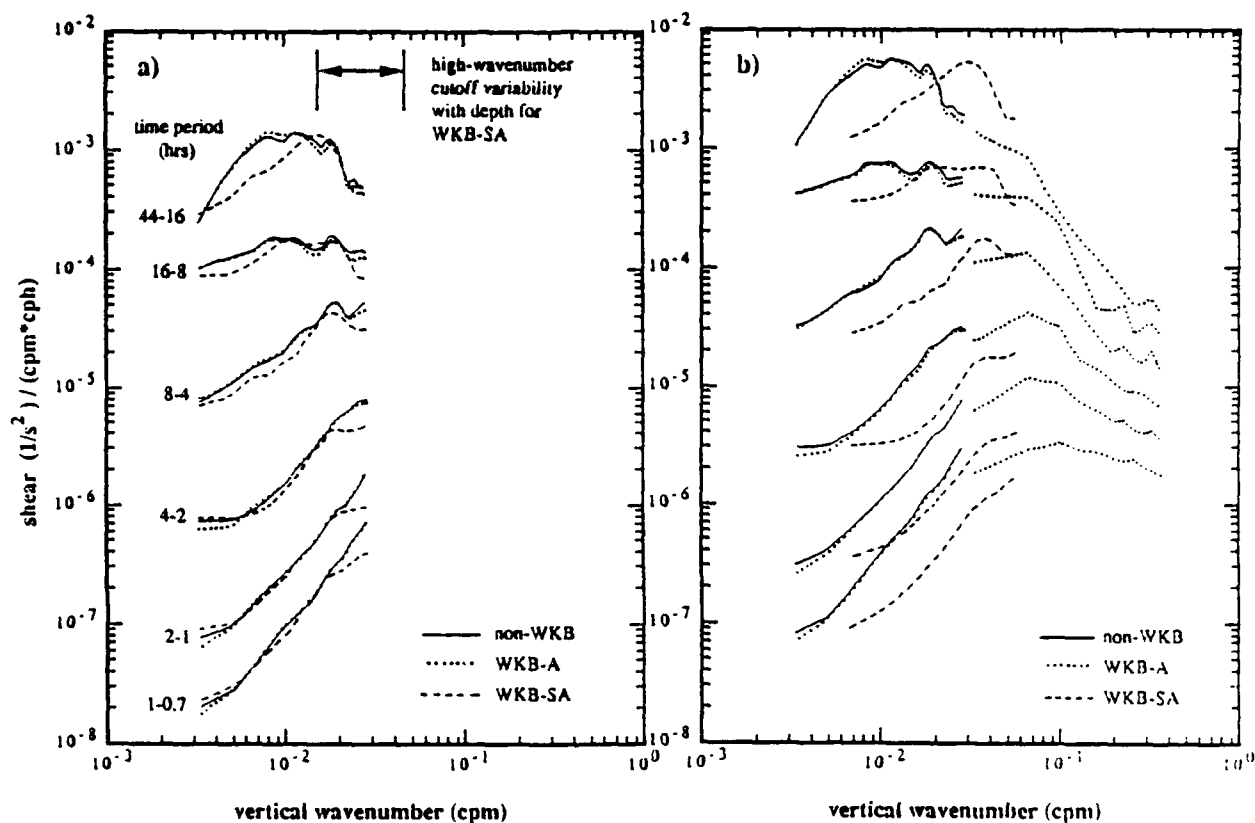
**Figure 4.8.** a) Three versions of the long-range data set (WKB-SA, WKB-A, and non-WKB, as defined in text) were Fourier transformed in both space and time. Frequency spectral estimates were averaged into different time-period bands. As in Fig 4.7, the WKB-stretched data set (WKB-SA) has distorted the high-wavenumber cutoff. Each frequency band has been offset by a factor of 2 for easier comparison. b) The spectra in a) are computed for an average Vaisala frequency of 2.6 cph. To adjust to the depth of the short-range sonar (N = 5.3 cph), WKB theory conjectures that both energy levels must rise, and wavenumbers be increased. The Gargett et al. model suggest that only energy levels should increase. Both hypotheses are shown in b). Also shown is the spectrum as computed from the short-range sonar.
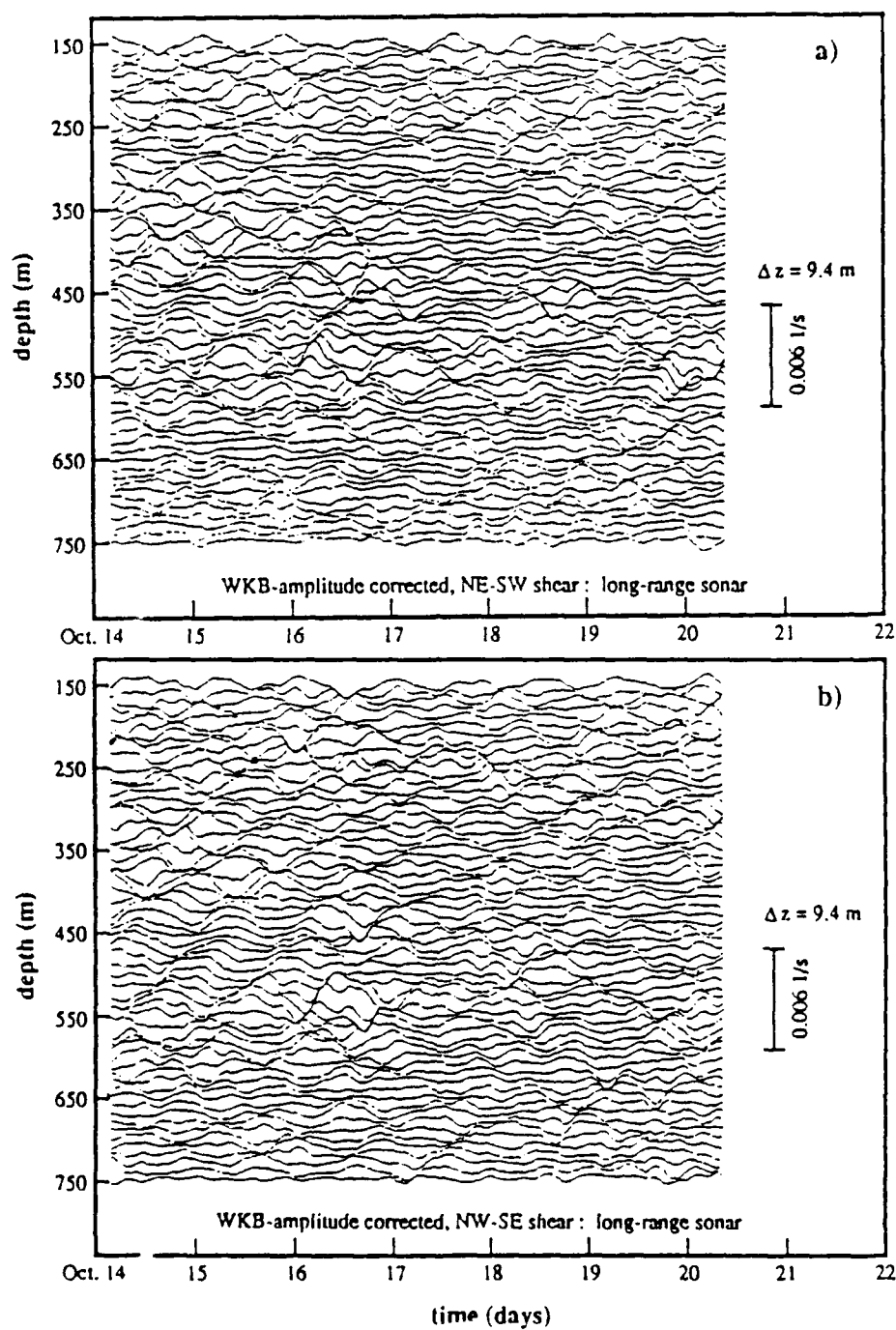
**Figure 4.9.** a) and b) are time series for both components of shear as estimated from the long-range sonars. Amplitudes are WKB-corrected in depth. A four hour running-mean-filter has been applied in time.
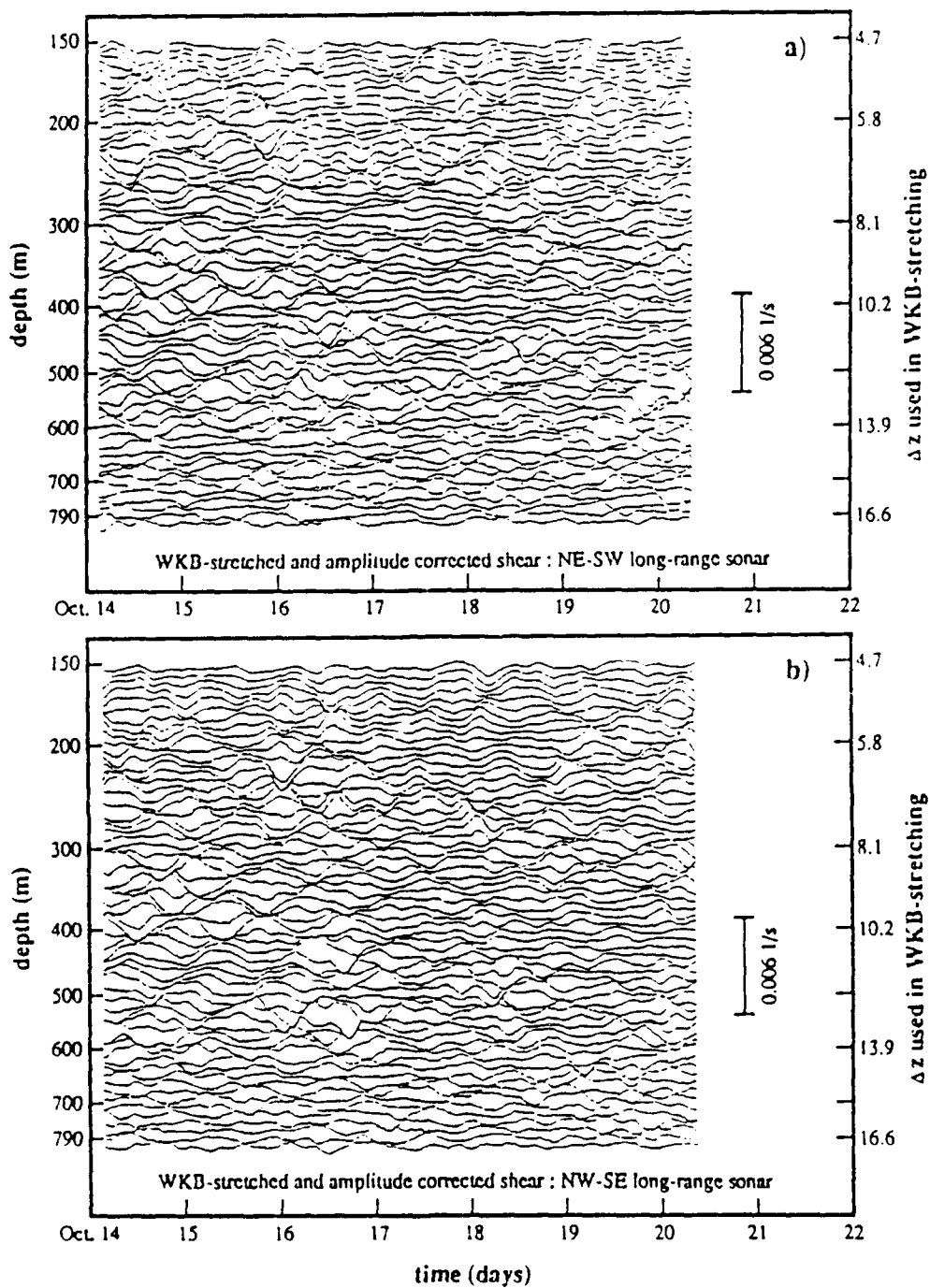
**Figure 4.10.** a) and b) is the same data set as in Fig. 4.9, but now WKB-stretched in depth. A four hour running-mean-filter has been applied in time.
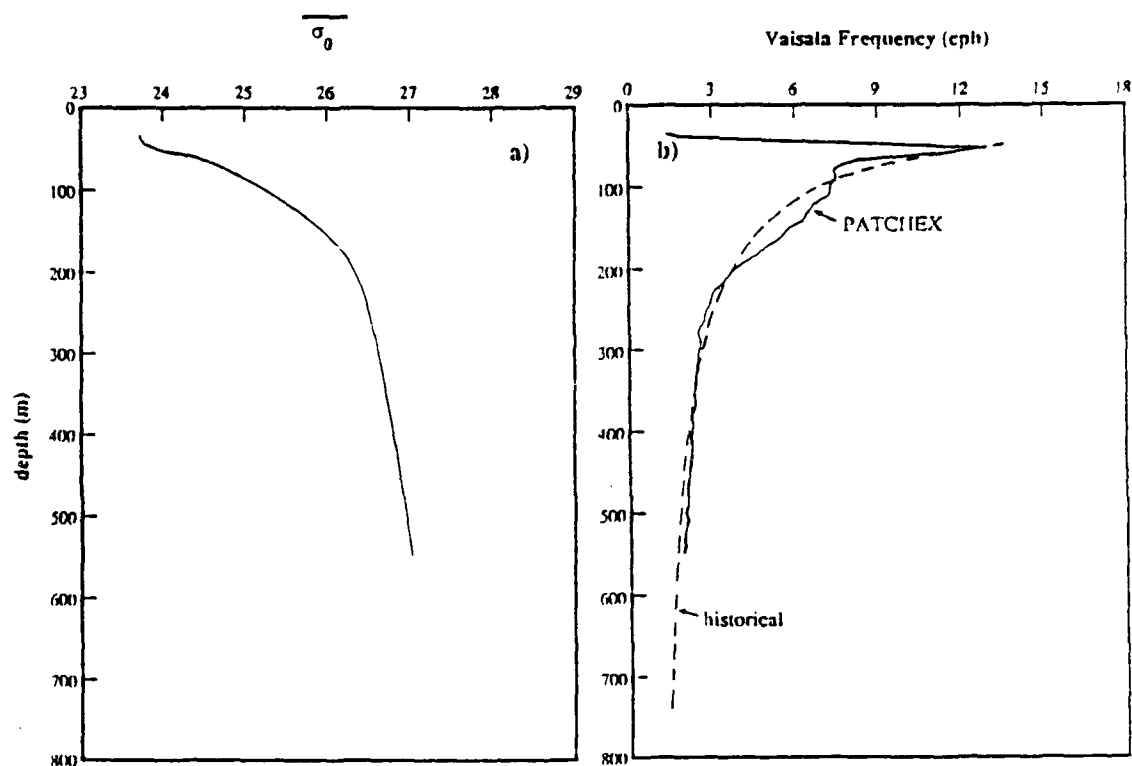
$$\overline{\sigma_0}$$

Vaisala Frequency (cph)



**Figure 4.11.** a) 7.5 day mean $\sigma_t$ profile from CTD data is plotted, along with b) the average Vaisala frequency profile. Also shown in b) is the curve fit to the historical data set. per Williams(85).
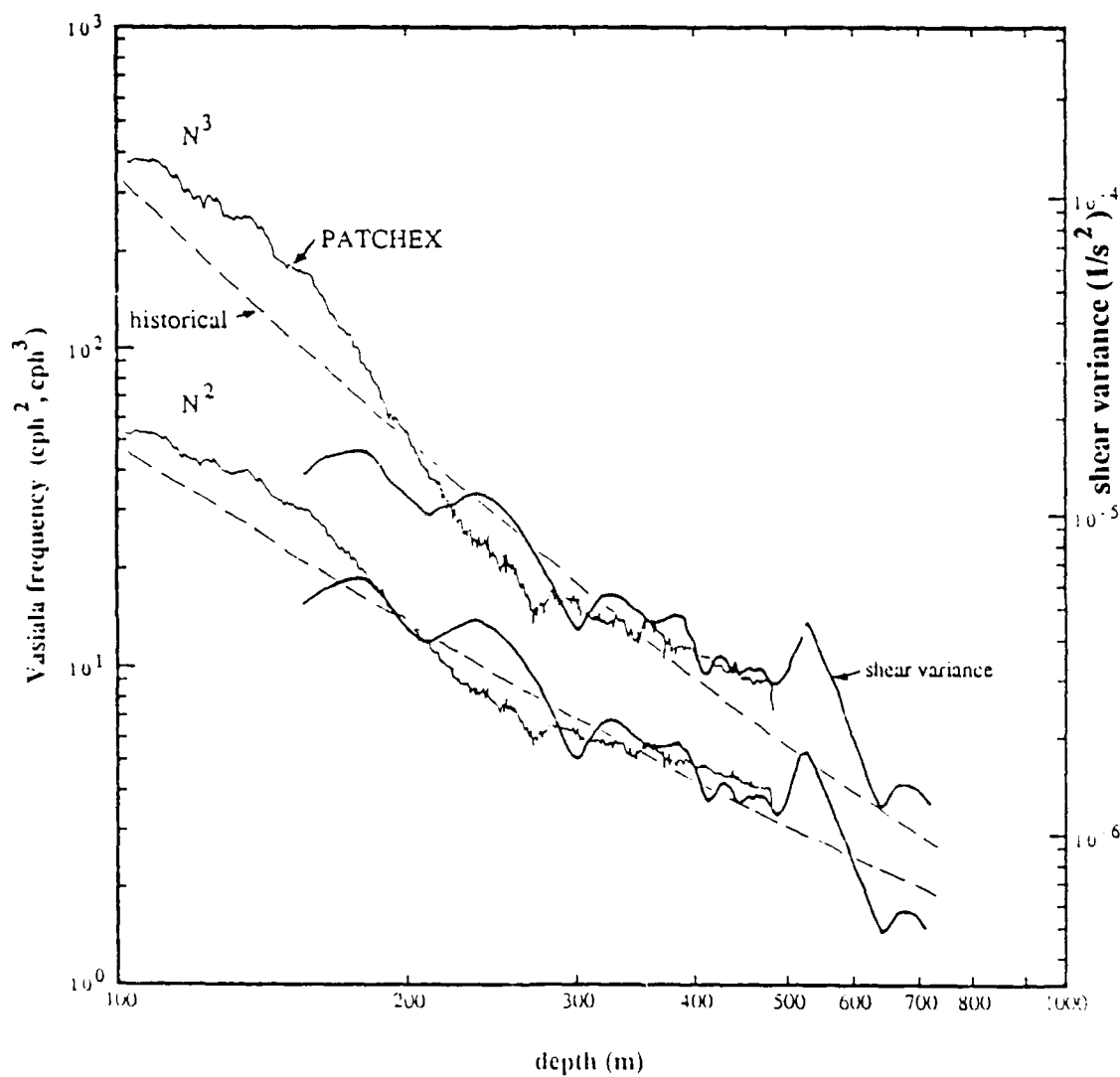
**Figure 4.12.** The $N^2$ and $N^3$ values of Fig. 4.11b are plotted versus depth. Also shown is the long-range sonar's average shear variance with depth. WKB theory predicts shear variance should scale as $N^3$, while Gargett et al.(81) claim shear scales with $N^2$.
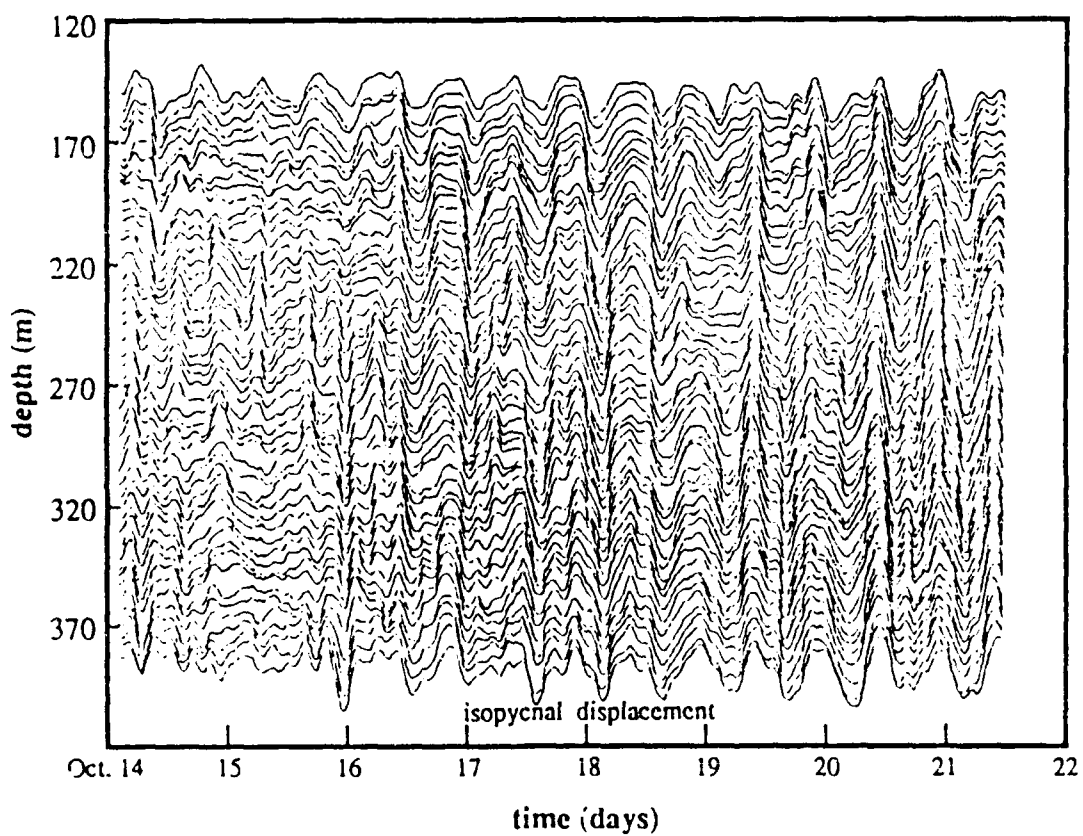
**Figure 4.13.** Isopycnal displacement time series (with a 2 hour running-mean-filter applied) displays a dominant low-modal tidal frequency.
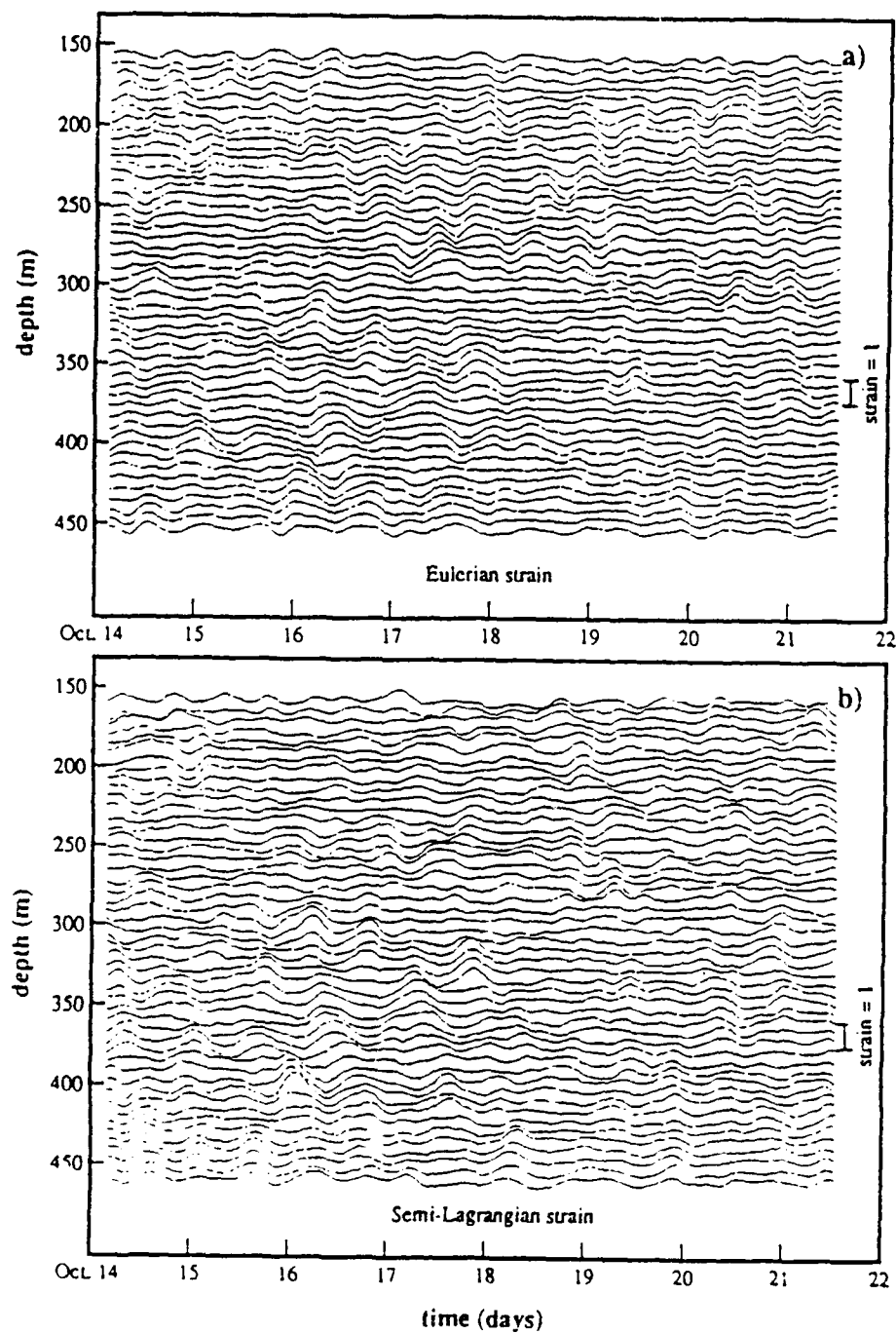
**Figure 4.14.** The Eulerian (a) and semi-Lagrangian (b) strain time series have a running-mean-filter of 4 hours in time and 20 m in depth applied.
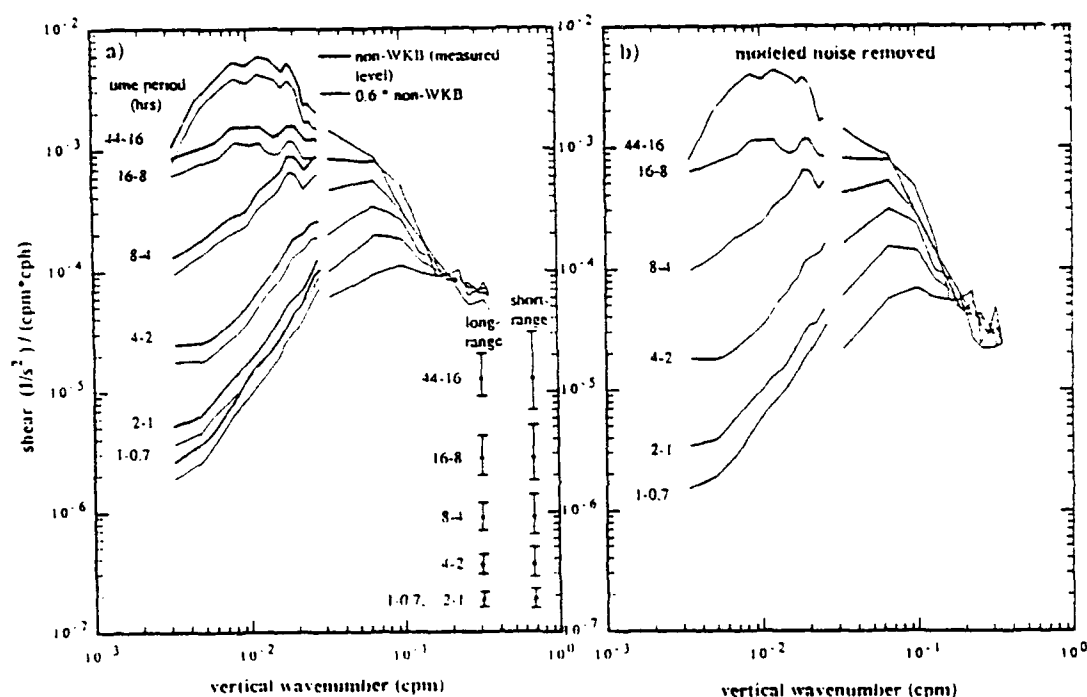
**Figure 4.15.** The composite wavenumber-frequency spectrum includes both the long-range and short-range sonar estimates. Average spectral density levels are shown for six bands : 44-16, 16-8, 8-4, 4-2, 2-1, and 1-0.7 hour periods. Long-range data is averaged over 3 wavenumber estimates, incre. ng its spectral precision as compared to the short-range sonar. a) shows the long-range sonar's non-WKB spectrum and the short-range sonar spectrum, with energy levels as estimated (dark lines). The light lines are the non-WKB spectral levels reduced by 40%, giving the best fit to the short-r ige data. b) is the resulting spectrum when noise floor estimates are removed ($m^{+2}$ slope for long-range sonar, $m^0$ slope for short-range sonar).
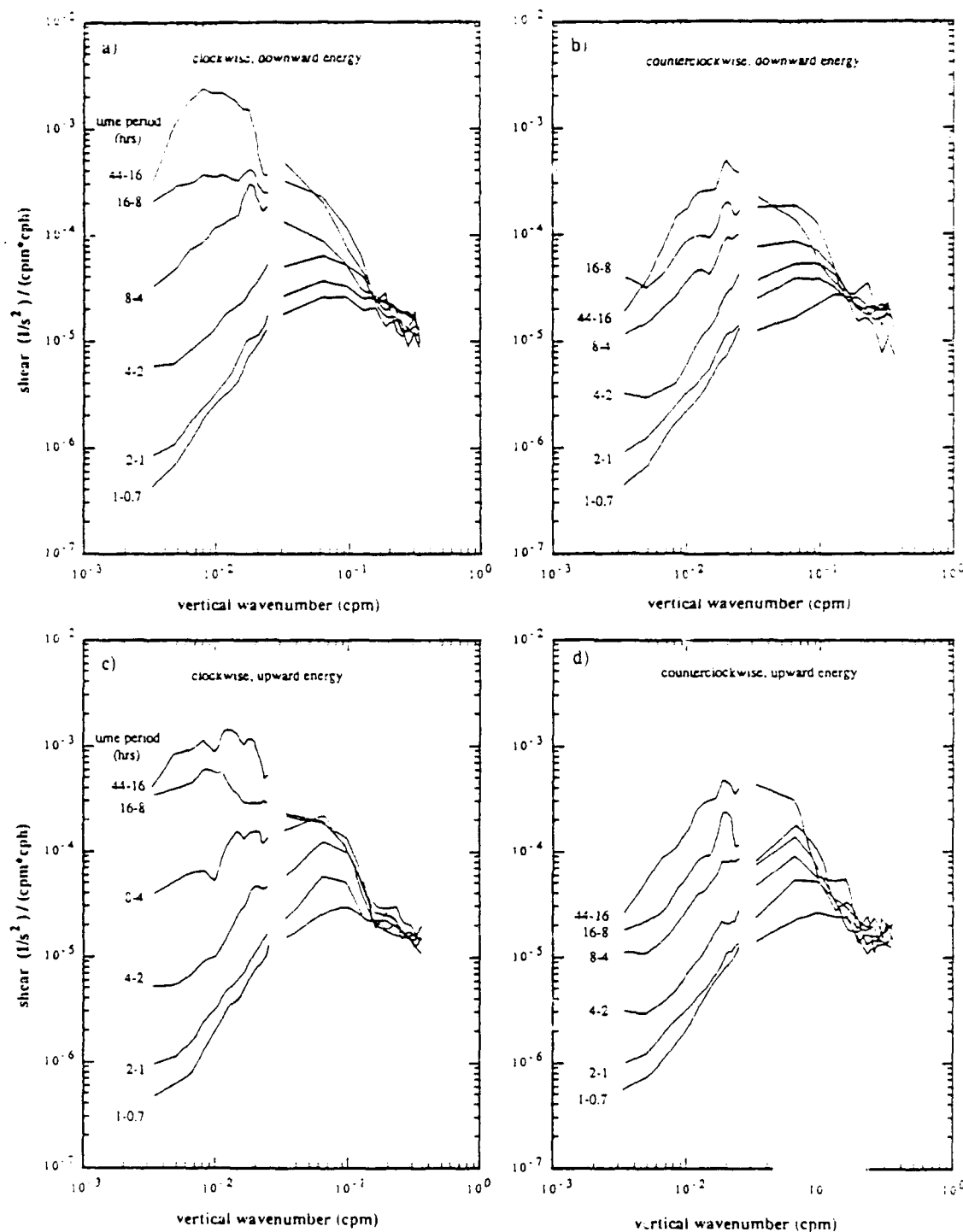
**Figure 4.16.** Rotary spectral estimates are displayed for a)clockwise, downward energy propagation (upward phase propagation), b) counterclockwise, downward energy, c) clockwise, upward energy, and d) counterclockwise, upward energy.

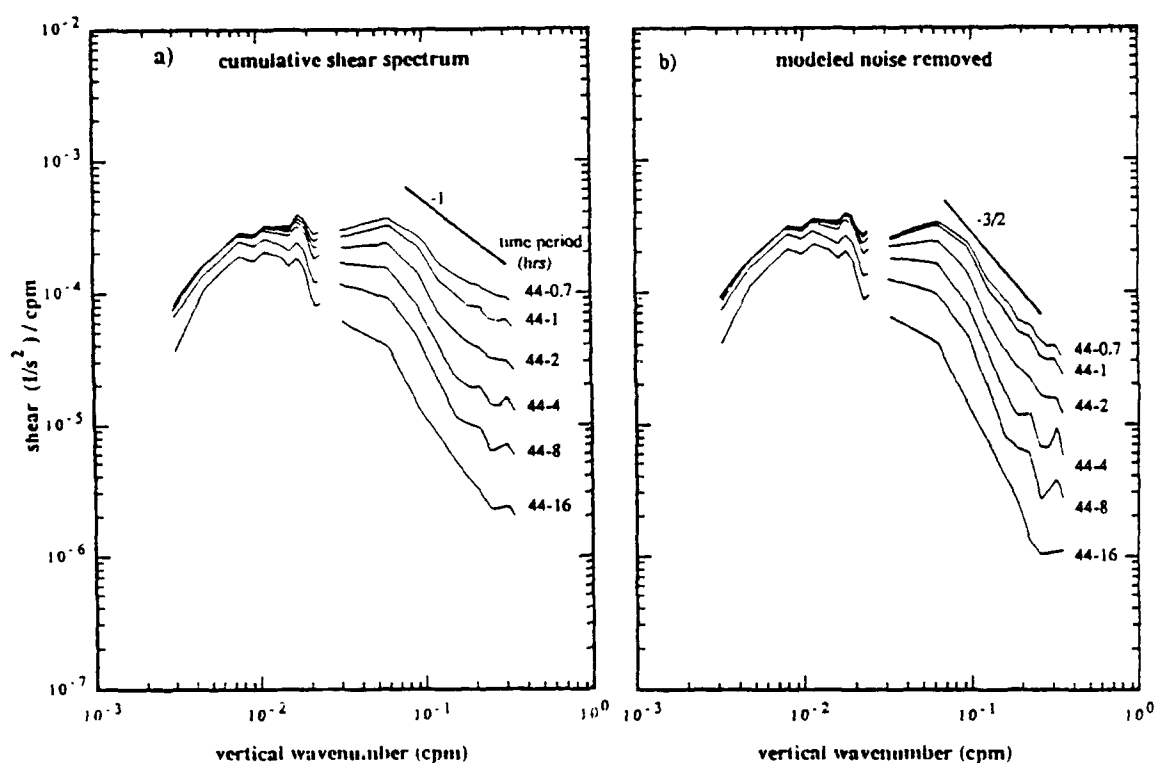**Figure 4.17.** Integration of energy across frequency bands yields a cumulative vertical-wavenumber spectrum, with the top curve representing total variance between 0.7-44 hour time periods. a) includes noise, while b) has modeled noise removed.
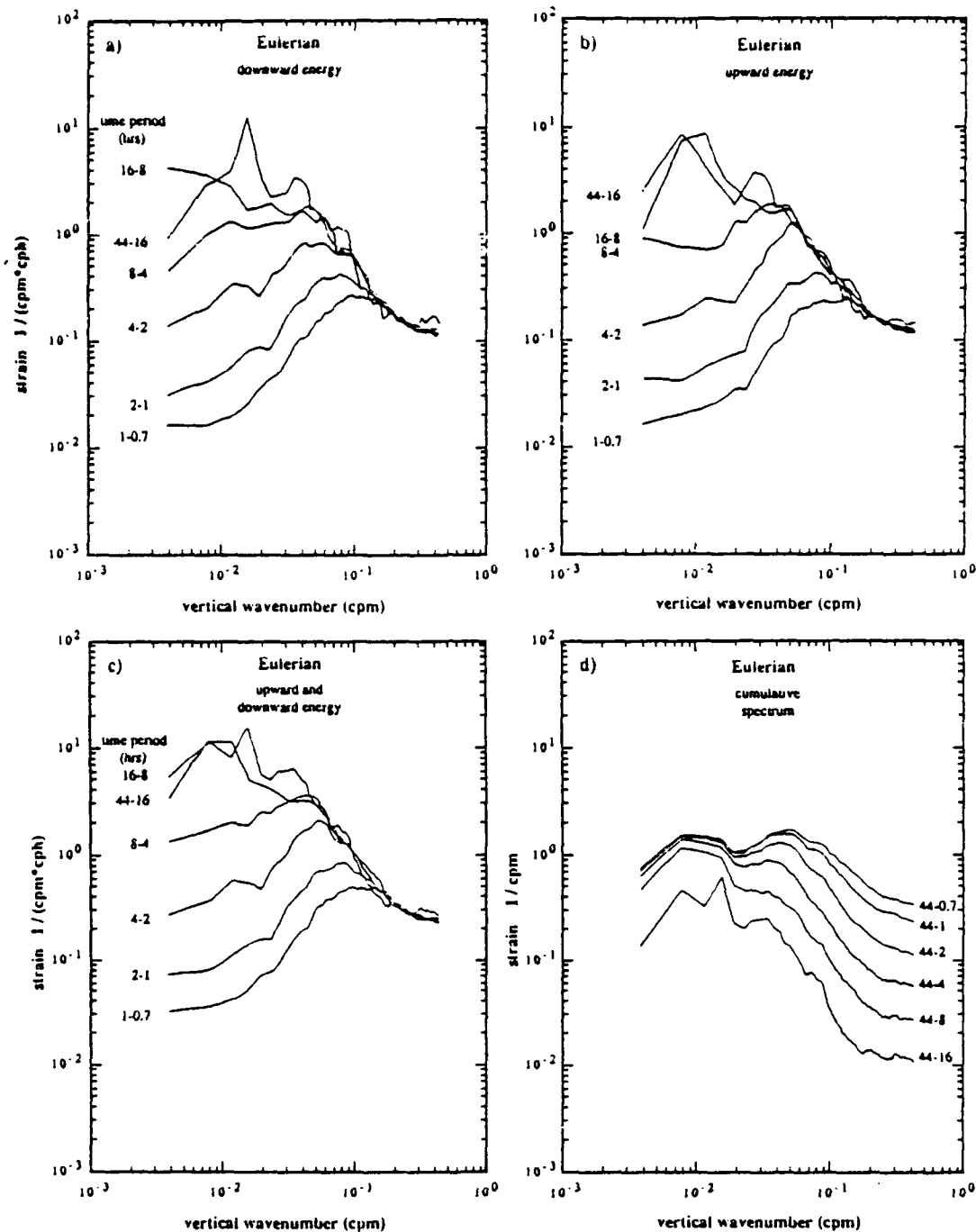
**Figure 4.18.** a) downward, b) upward, c) and combined ($m,\omega$) spectra based on fixed-depth (Eulerian) strain are shown with the same frequency bands as described in Fig. 4.15. d) is the integrated variance over frequency. Spectral estimates have been logarithmically-smoothed in $m$, with a bandwidth equal to $\delta m = \pm 0.1 m$.
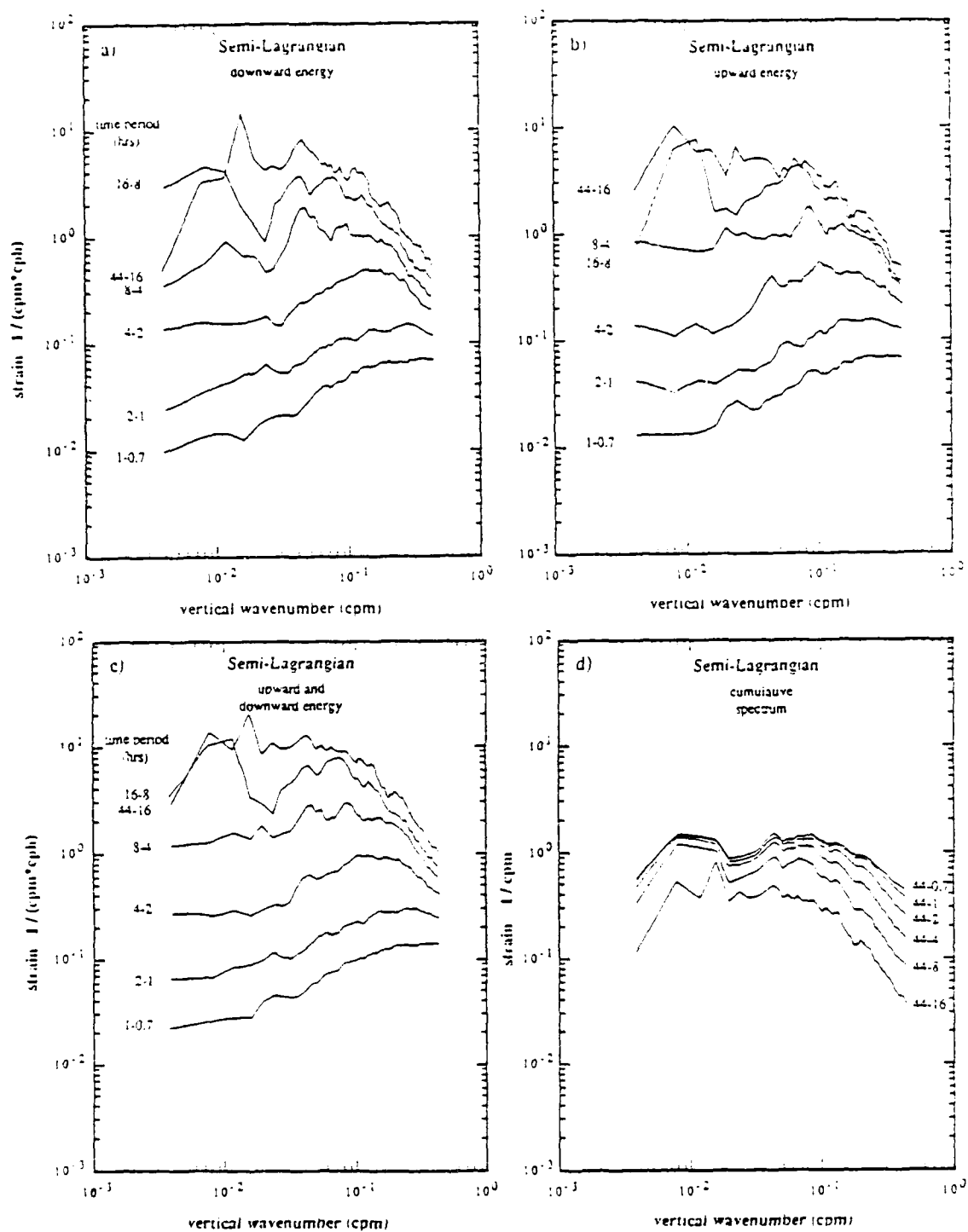
**Figure 4.19.** Same as Fig. 4.18, but based on semi-Lagrangian strain estimates.
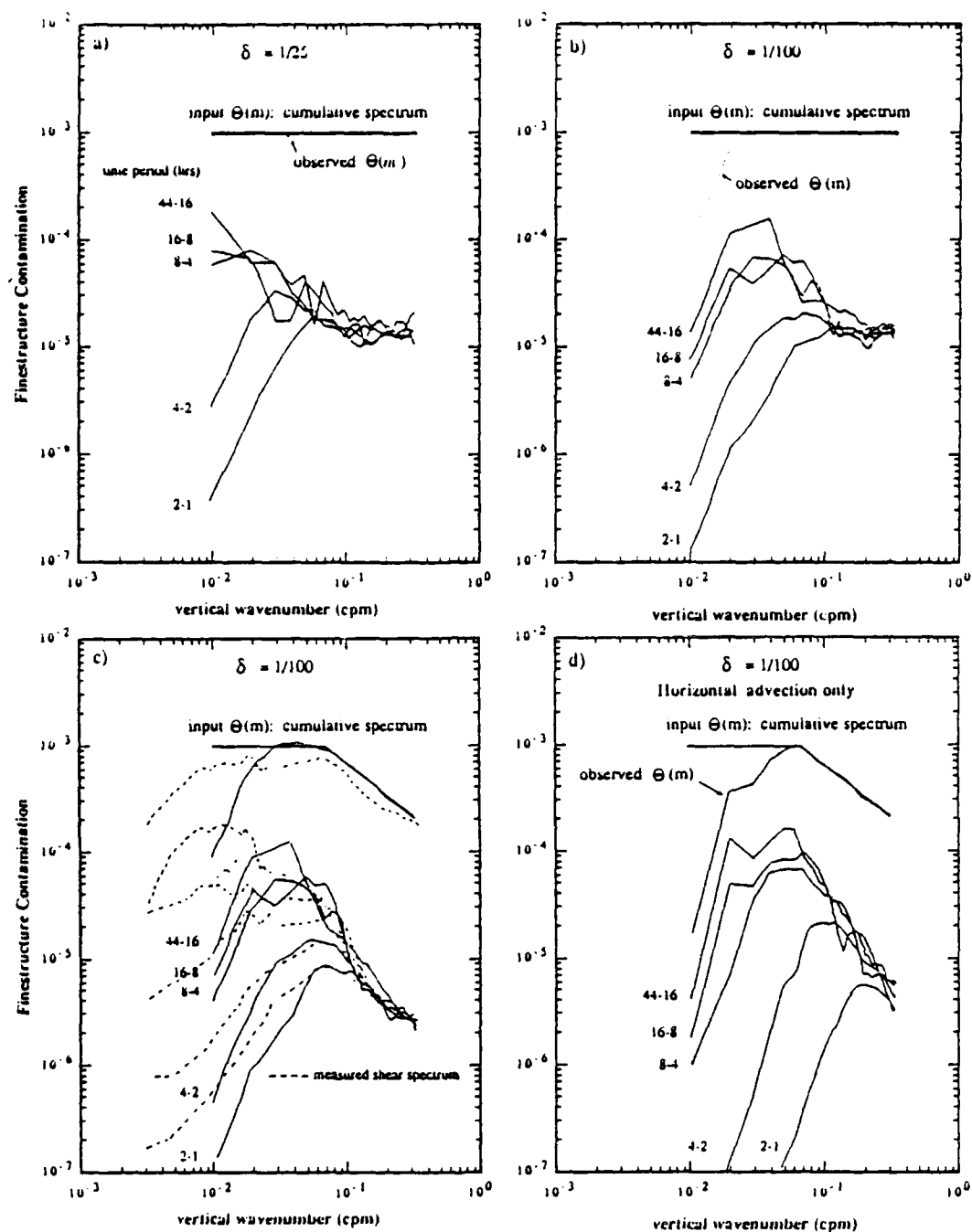
**Figure 4.20.** $(m,\omega)$ spectra are computed based on a background field 'white' in wavenumber being advected past a fixed sensor by the internal wave field. The 'cumulative' lines are the frequency-integrated (1-44 hour periods) wavenumber spectra. They have been offset for easier visual display. a) has $\delta = 1/25$, b) $\delta = 1/100$, and c) $\delta = 1/100$, with the background field having a $m^0$ slope for $m < 0.07$ cpm, and a $m^{-1}$ slope for $m > 0.07$ cpm. The dashed lines are the measured shear spectra, as per Fig. 4.15a. d) The same background field in c) is now only horizontally advected, to simulate what the semi-Lagrangian strain field might see.
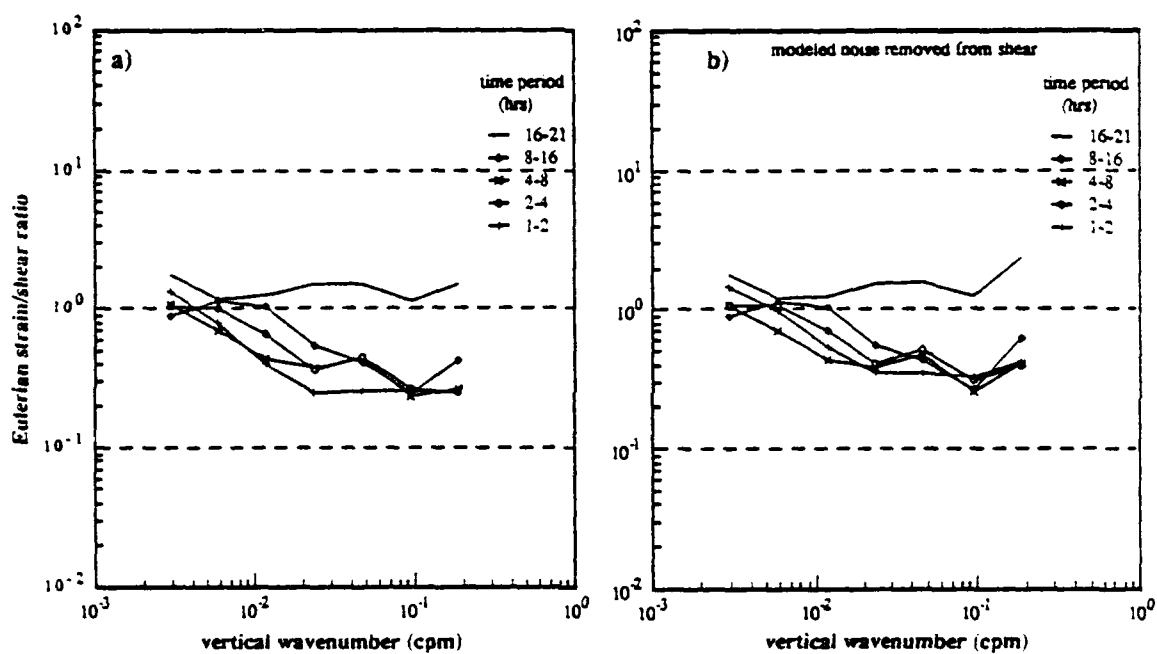
**Figure 4.21.** The measured ratio of strain/shear variance is divided by the ratio predicted by linear theory. Therefore a value of 1 means perfect agreement, >1 too much strain, <1 too little strain to agree with linear theory. Estimates are averaged over wavenumber bands to provide better precision. In b), the shear variance has estimated noise levels removed.
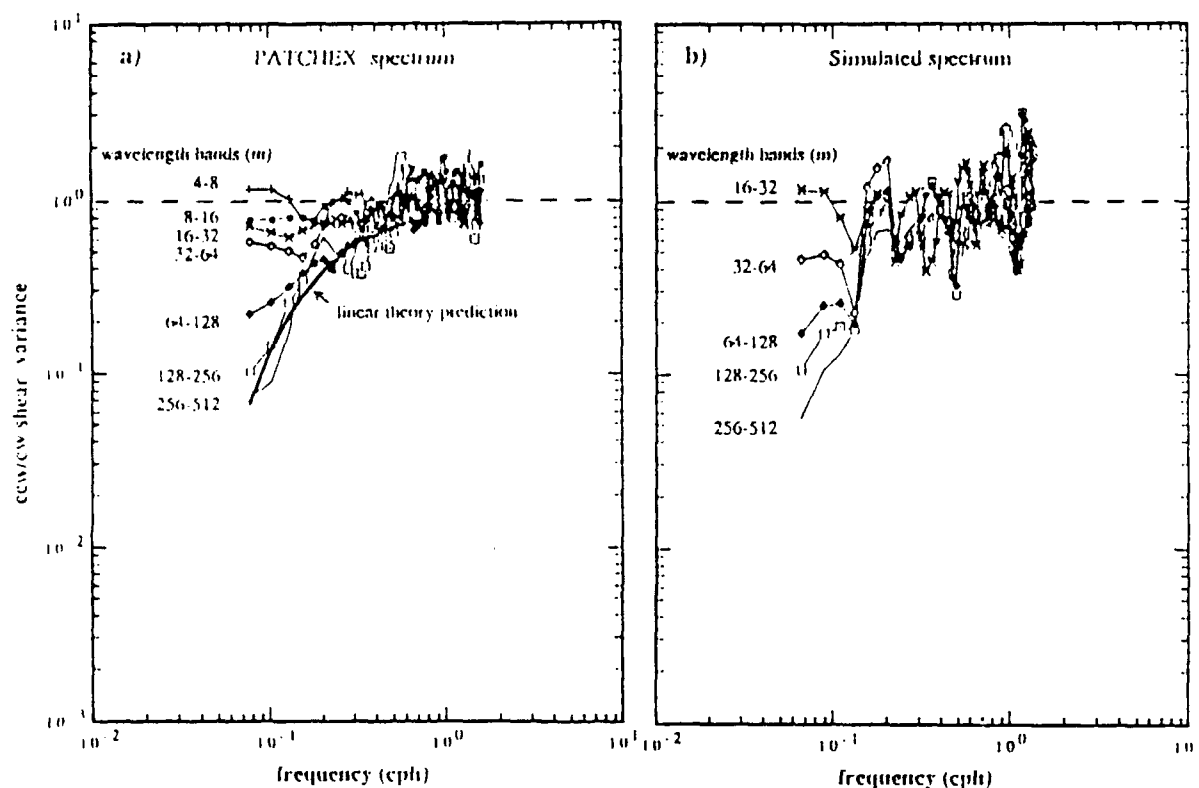
**Figure 4.22.** a) measured counterclockwise/clockwise shear variance ratio, with the solid curve being the prediction from linear theory. Values have been averaged over various wavenumber bands, and shows disagreement with linear theory at high wavenumbers. b) A purely inertial shear field, with equal energy distributed between 512-16 m vertical wavelengths, is vertically advected past a fixed sensor by the measured low-wavenumber isopycnal displacement time series. The estimated ccw/cw ratio is displayed from this simulated data set, showing that the vertical advection has contaminated the sense of measured rotation. Disagreement in a) from linear theory can therefore be explained by vertical advection contamination.

83
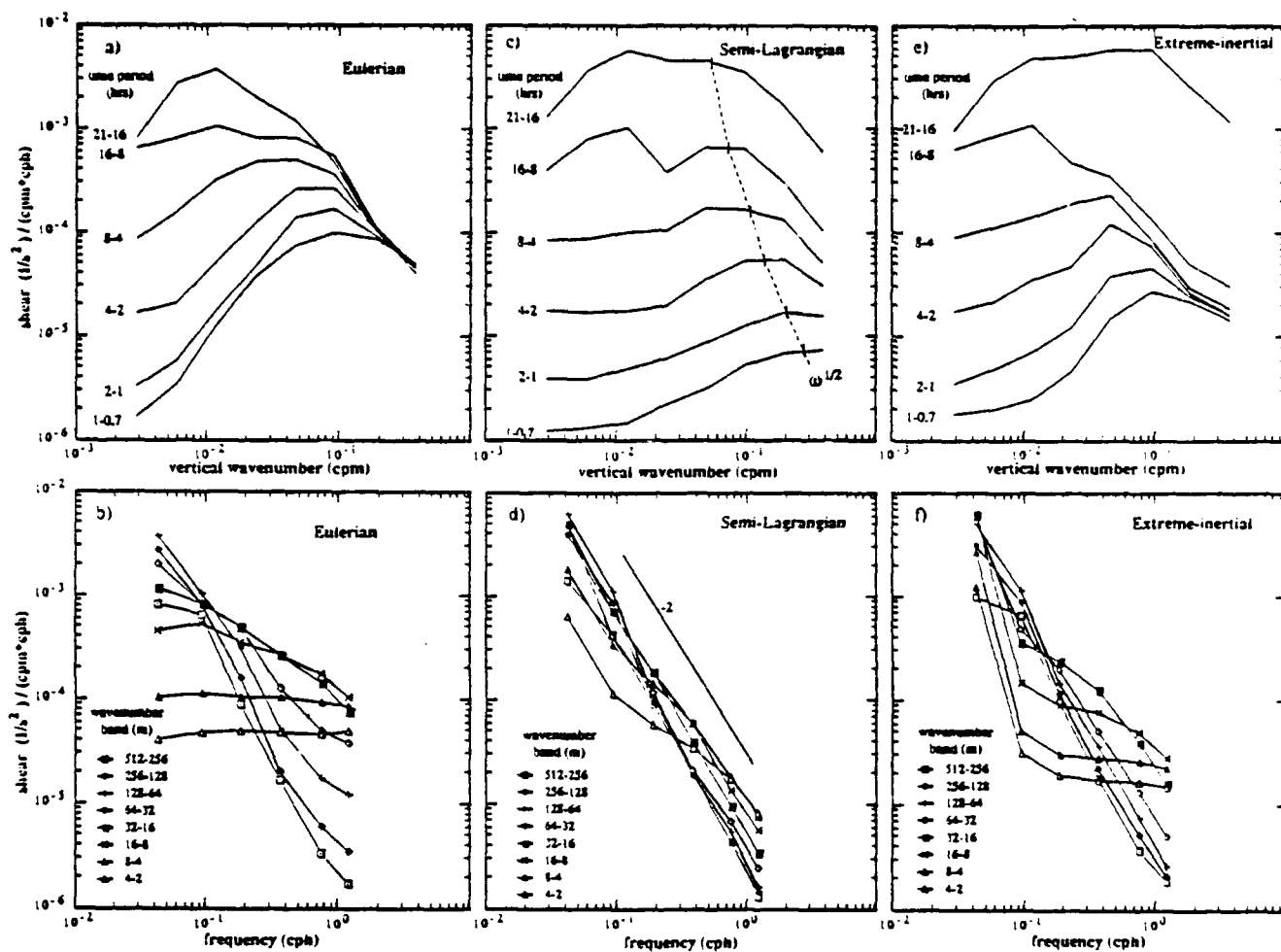
**Figure 4.23.** Shear $(m,\omega)$ spectra are averaged into eight different wavenumber bands(512-256,256-128,....,4-2 m wavelengths). a) is the Eulerian spectrum based on Fig. 4.15a. c) is computed from the 'semi-Lagrangian' model, and e) is from the 'extreme inertial' model. b), d), and f) are the same spectra, but now viewed with frequency on the x axis.
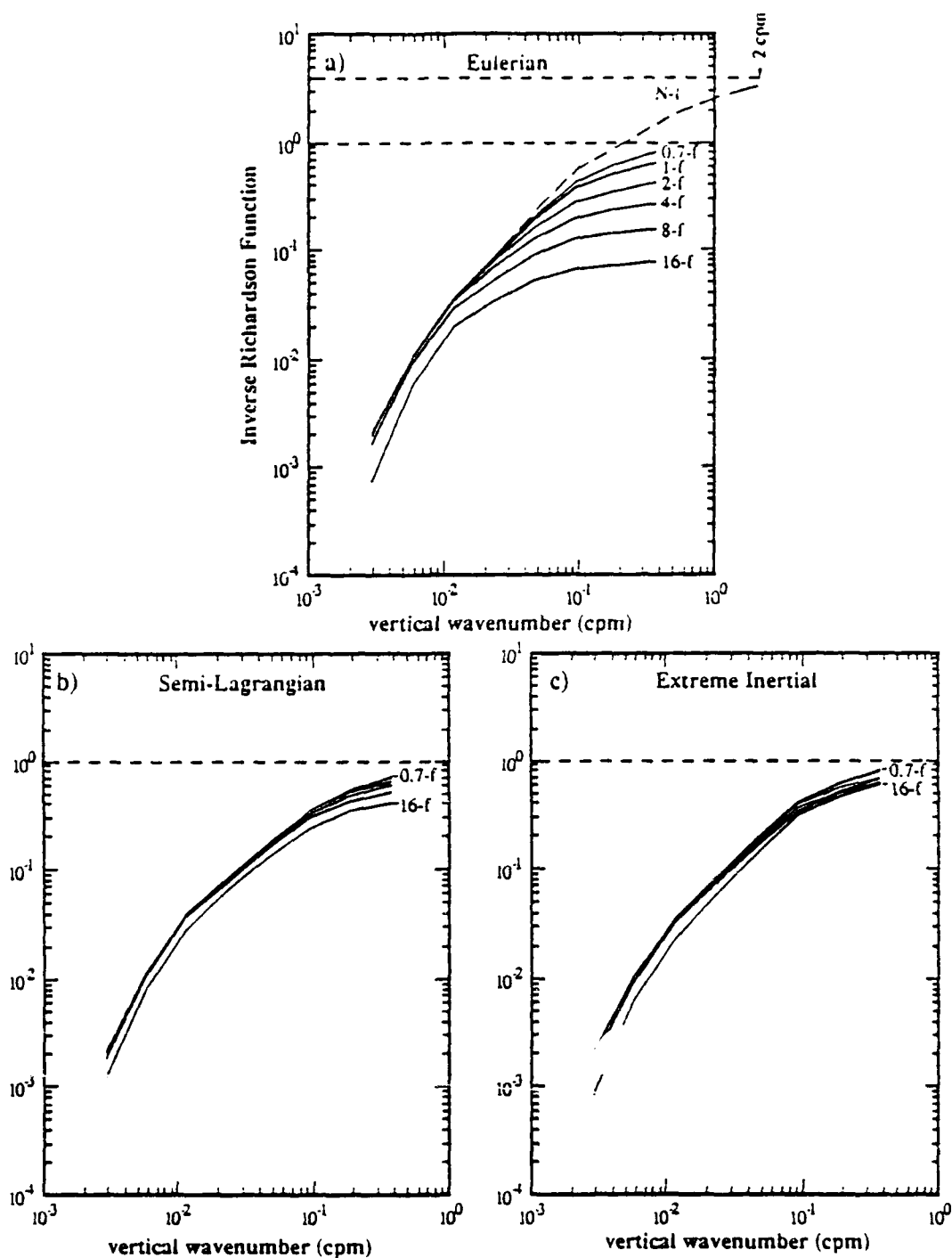
**Figure 4.24.** Estimates are shown of the Inverse Richardson Function, based on Fig. 4.23. a) uses the Eulerian spectrum, and also displays an extrapolated curve out to the Vaisala frequency. b) is derived from the 'semi-Lagrangian' spectral model, while c) is from the 'extreme inertial' spectrum.
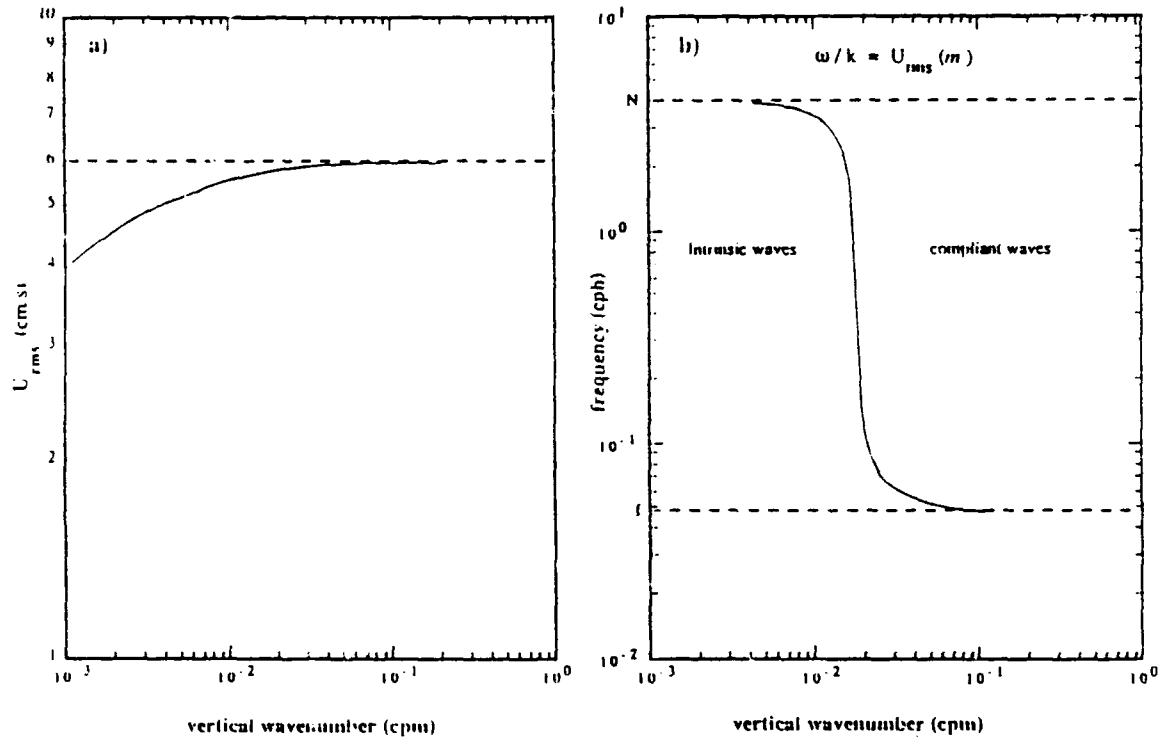
**Figure 4.25.** a) Rms horizontal velocity is estimated, with energy integrated up ·o wavenumber $m$. b) Given $U_{rms}(m)$, $\omega(m)$ is calculated such that the horizontal phase speed $(\omega/k) = U_{rms}$. For internal waves with $(\omega,m)$ to the right of this line (Munk's(81) compliant region) caustics are highly probable, while waves with $(\omega,m)$ to the left (Munk's intrinsic region) should move fast enough to avoid caustics.

## APPENDIX A

## Technical Description of the MPL Coherent Sonar

### A.1 Hardware

The MPL coherent sonar was developed to investigate fine-scale shear in the upper ocean from the research platform FLIP. An illustration of the instrument is shown in Fig. A1. The instrument is configured as a four beam Janus system, with each beam oriented downwards at a 55° angle from the azimuth. Each beam consists of a transmit and receive transducer pair (both of identical design) oriented in a 'T' configuration. Each transducer has a 1° x 3° main lobe. The 'T' geometry gives a composite beam pattern of 1° x 1°. Pertinent dimensions are given in Table A1.

The instrument is suspended from a 0.8" diameter electro-mechanical cable such that its depth can be adjusted to the desired level. Deployment is from a boom mounted on FLIP approximately 10 m above the water (geometry is shown in Fig. A2). Although the sonar was built to go to 1 km, the system is presently constrained by the length of cable, giving it a maximum depth of 145 m. To avoid side lobe interference from FLIP (which draws 90 m in its vertical position), the instrument is typically deployed near its 145 m maximum.

The sonar transducers are mounted to a pressure case which contains the receiver pre-amp electronics (which amplify the signal by approximately 60 dB), and the positional sensor electronics. Positional sensors include a compass, two accelerometers, a pressure sensor, and temperature sensor. Receiver pre-amps are required to eliminate noise pickup problems between the instrument and electronics located in the lab on FLIP. The instrument package does no processing, allowing easy debugging of the system from topside.

Located in the lab are the transmit electronics, the receive amplifiers (giving another 30 dB of gain), mixers (to remove the carrier frequency), low pass filters, A/D converters, and processing computer. Processing is done on a Motorola VME system 1000, with graphics display and backup recording on a HP 217 system. A block diagram of a generic Doppler sonar system is shown in Fig. A3.

### A.2 Instrument Motion Estimates

FLIP's motions create both horizontal and vertical movements of the package. FLIP has a broadband response to wind, currents, and waves, resulting in angular and translational motions. The coherent sonar package has its own response characteristics to the dynamics of FLIP, which varies with the sonar's depth and environmental conditions.

Instrument motion causes Doppler shifting of the return signal. The bandwidth associated with this instrument motion must be estimated to calculate the overall velocity variance. The MPL Doppler sonar first-differences velocity in range once every two seconds, and then averages these estimates. This removes instrument motion with periods greater than two seconds, limiting the bandwidth to frequencies greater than 0.5 Hz.

Instrument motion bandwidth is estimated from a 38 minute data set of the positional sensors. The data was recorded at a 10 Hz sampling rate, with sea

conditions representative of the PATCHEX data cruise. Spectral analysis is employed to obtain information of what frequency motions are dominant, and to estimate the amount of total variance above 0.5 Hz. Variance is also calculated over two second time periods, and averaged over the 38 minute data set. The difference between the two variance estimators is due to the spectral integration leaving out all low frequency information, and thus underestimating the actual variance.

Vertical motions can be derived from the pressure sensor. The pressure signal due to surface waves experiences an exponential rolloff with depth, with the e-folding distance being a function of wave period. At 145 m depth, a 20 second period wave has its pressure attenuated to 25% of its value at the surface, a 10 second period to 0.36%, 8 second period to 0.04%, etc. High-frequency pressure fluctuations at 145 m depth represent the true vertical displacement of the instrument package. This signal can be first-differenced in time to produce vertical velocity estimates. Spectra of both vertical displacement and velocity are shown in Fig. A4. Also shown are plots of the integrated variance between a given frequency and the Nyquist sampling frequency ($\approx$ 5 Hz). The narrow-band high frequency sources (above 1 Hz) are probably due to cable strumming. Fig. A4 shows a vertical velocity standard deviation of 1.6 cm/s for all frequencies greater than 1/2 Hz. This agrees with the value of 1.6 cm/s obtained from the variance calculated over the two-second time periods. The dominant 26 second period energy peak corresponds well to Rudnick's(64) computed vertical resonance period of 27 seconds.

Estimating horizontal motions from accelerometer data is more complicated. The accelerometer signal is comprised of instrument acceleration plus the tilt angle of the sonar. For high-frequency motions, where tilt angles are small compared to accelerations, the signal can be interpreted as pure acceleration. At low frequencies, where accelerations are quite low, the signal can be interpreted as pure tilt. Worse case values can be obtained for both tilt and acceleration by assuming that the accelerometer signal is comprised entirely of one or the other. Acceleration estimates can be integrated to give values of horizontal velocities. Spectra, and integration of spectra, are given for both tilt and velocities for both accelerometers in Figs. A5 and A6. The worse case tilt values are extremely low (.05° rms). Horizontal velocity estimates give 0.55 cm/s rms for both x and y accelerometers combined. The velocity standard deviation for frequencies>0.5 Hz decreases to 0.14 cm/s. Since much of the variance comes from frequencies just lower than 1/2 Hz, the estimated standard deviation from two-second time blocks is increased to 0.3 cm/s.

Analysis of compass data shows motions dominated by low frequency oscillations, with less than 0.1° rms rotation for frequencies above 1/2 Hz (Fig. A7). Standard deviation based on the two-second time period give an rms rotation of 0.3°. For a 1° beam angle, this implies thirty percent signal decorrelation every two seconds due to instrument rotation.

Due to the deployment cable being constructed with a double-armored opposite-lay stainless steel outer wire, the instrument experiences very little long-term rotation. This is seen in the complete time series of the PATCHEX cruise(Fig. A8f), where compass direction varies by less than ± 15° over the 7.5 day time span. Also shown are the time-series records for the rest of the positional sensors. Instrument depth varies by less than 25 cm, most probably due to FLIP tilting from wind and ocean currents. The temperature sensor reflects the internal tide signature. The low frequency tilting of the instrument is of order 0.1°, with possible causes being 'dragged' through the water by FLIP drifting on her two-point moor, and by currents acting on the deployment cable.

Total velocity variance along the beam due to instrument motion will be equal to:

$$\sigma_I^2 = (\sigma_{vert}\sin(\phi))^2 + (\sigma_{horiz}\cos(\phi))^2$$

where $\phi$ = angle of the sonar with respect to the azimuth = 55°. Substitution gives $\sigma_I$ = 1.3 cm/s. The major contributer is from vertical motions, which the pressure spectrum (Fig. A4) suggests comes from FLIP tilting in response to surface waves, plus possible cable strumming at higher frequencies.

| MPL Coherent Sonar Specifications | |
|---|---|
| **Instrument Dimensions** | |
| Height (top of cage) ................ | 1.5 m |
| Maximum width ...................... | 1.8 m |
| Weight (in air) ........................ | 272 kg |
| **Transducer Panels Information** | |
| height ...................................... | 56 cm |
| width ...................................... | 20 cm |
| beam width ............................. | 1 x 3 degrees |
| (composite transmit/receive .... | 1 x 1 degrees ) |
| Angle of panels wrt vertical .... | 55 degrees |
| **PATCHEX Transmission Information** | |
| Transmission frequency ........ | 164 kHz |
| Pulse duration ........................ | 1 ms |
| Instantaneous power/beam .... | 300 watts |
| $\Delta$ = repetition period ............. | 60 ms |
| **Sampling Information** | |
| sampling rate ............................ | 1 kHz |
| Number of ranges sampled ...... | 60 |
| Ambiguity Velocity value ...... | 3.8 cm/s |

**Table A1.** The MPL coherent sonar specifications are given for its configuration during the PATCHEX experiment.
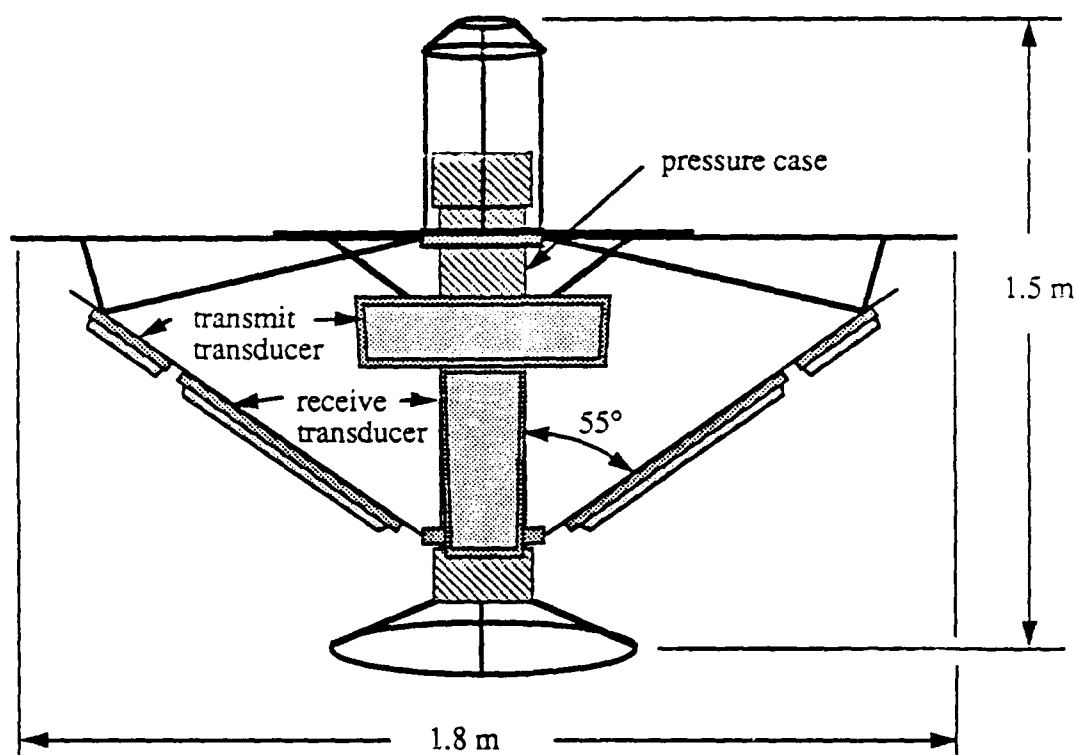
**Figure A1.** The MPL coherent sonar is shown in its four beam JANUS configuration. Beams are pointed downwards at a 55° angle. Each beam consists of a transmit and receive transducer, arranged in a 'T' configuration. The fourth beam (which faces into the page) is hidden from view by the beam facing out of the page.

# FLIP : PATCHEX configuration

Lat. 34° N
Long. 127° W

15 m

mixed layer
~50 m deep

'incoherent',
long-range sonar
1 km range

'upper' CTD
0-300 m

55°

145 m depth

'coherent',
short-range sonar
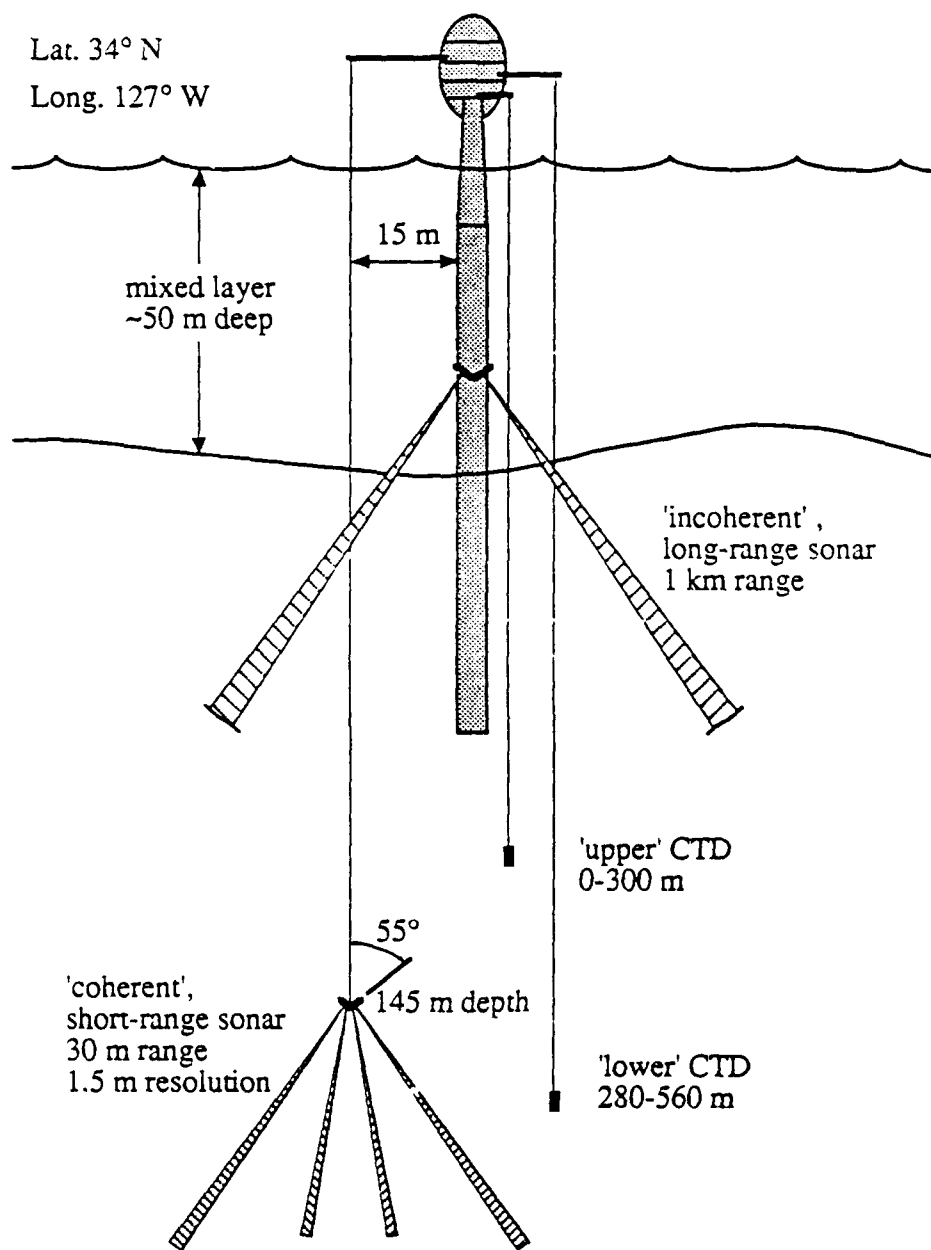30 m range
1.5 m resolution

'lower' CTD
280-560 m

**Figure A2.** The coherent sonar is deployed from a boom off the research platform FLIP, typically at a 145 depth. Shown is the configuration of FLIP during PATCHEX.
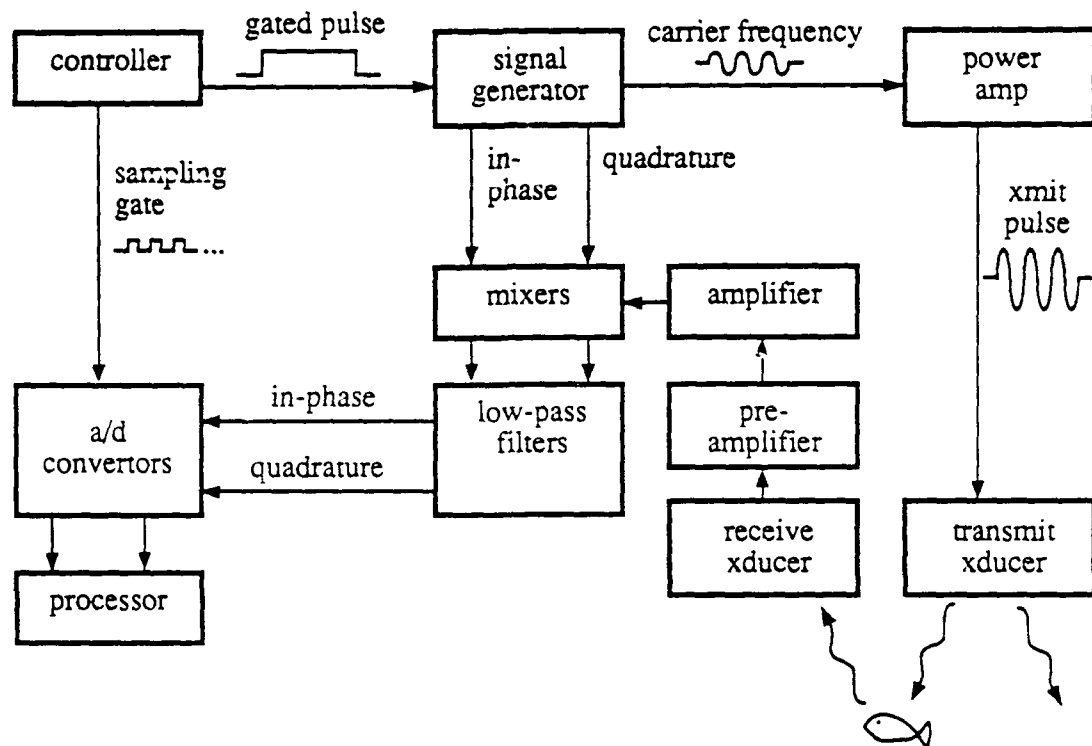
**Figure A3.** A typical sonar system operates in the following fashion: A master timing device (the controller) provides the synchronization needed for the various system components, controlling the transmission of the sonar pulse, and the sampling of the receive signal. A signal generator forms the transmission wave form, and provides the in-phase and quadrature reference signals for heterodyning the return signal. The power amplifier boosts the transmission signal to the required energy level for the sonar. This pulse propagates through the ocean, undergoing spreading and absorption losses, while also scattering off of particles along the way. This backscattering, or volume reverberation, propagates back to the receiver, where the signal is boosted through the pre-amplifier before making its way to the mixers. The mixers, using the waveform from the signal generator, remove the transmission frequency by heterodyning, leaving just the complex Doppler-shifted signal. This signal goes through low-pass filters to remove out-of-band noise, and is then sampled by an analog-to-digital converter, where it can finally be processed by the computer using the chosen algorithms.
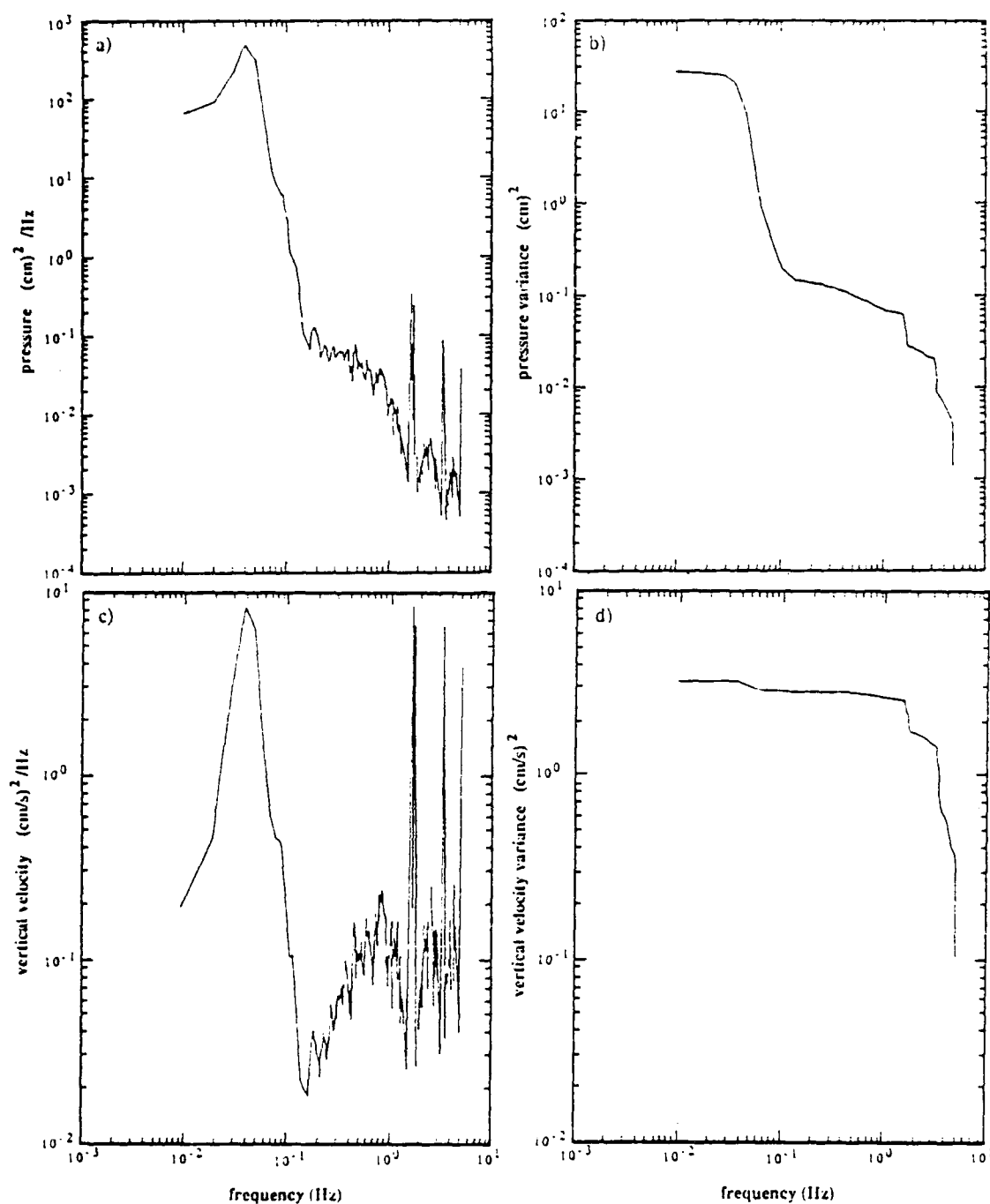
**Figure A4.** a) The pressure spectrum shows possible cable strumming at high frequency, along with a lower frequency (1/26 Hz) response, which is characteristic of FLIP's resonant response. b) The integrated variance values shows the sonar moving up and down ⁻5 cm rms over the thirty-eight minute time span, with the sonar only moving ⁻0.25 cm rms for frequencies above 1/2 Hz. c) The pressure signal was first-differenced in time to give vertical velocity estimates. This spectrum shows that cable strumming now contributes most of the velocity signal. d) Integrated variance shows ⁻1.6 cm/s rms vertical velocities from motions above 1/2 Hz.
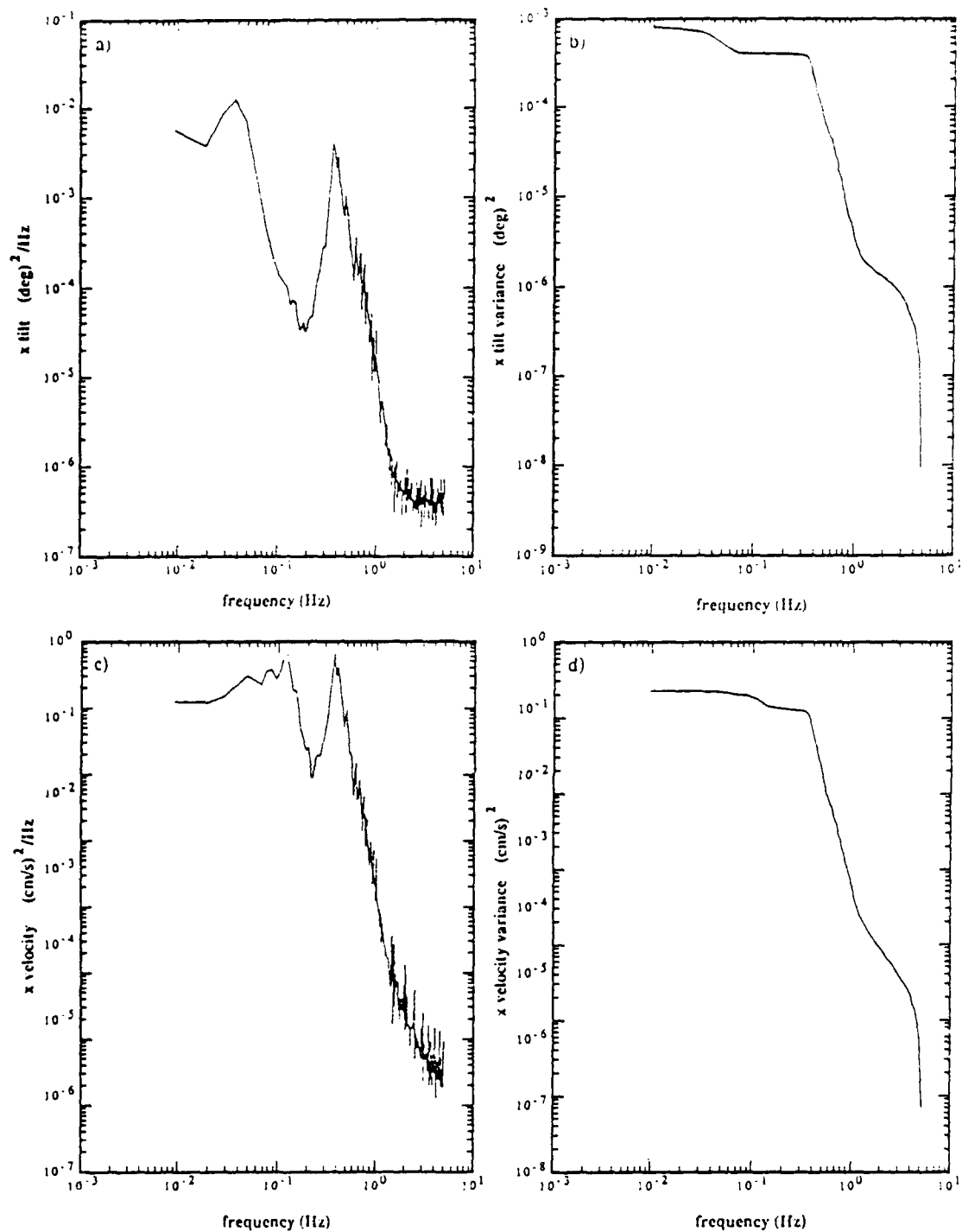
**Figure A5.** The x (E-W direction) accelerometer is interpreted as both pure tilt(a) and pure acceleration. Accelerations can be integrated to give horizontal velocities(c). b) and d) show that rms tilt values are less than 0.04°, while rms velocity = 0.49 cm/s for all frequencies, and 0.12 cm/s for frequencies above 1/2 Hz.
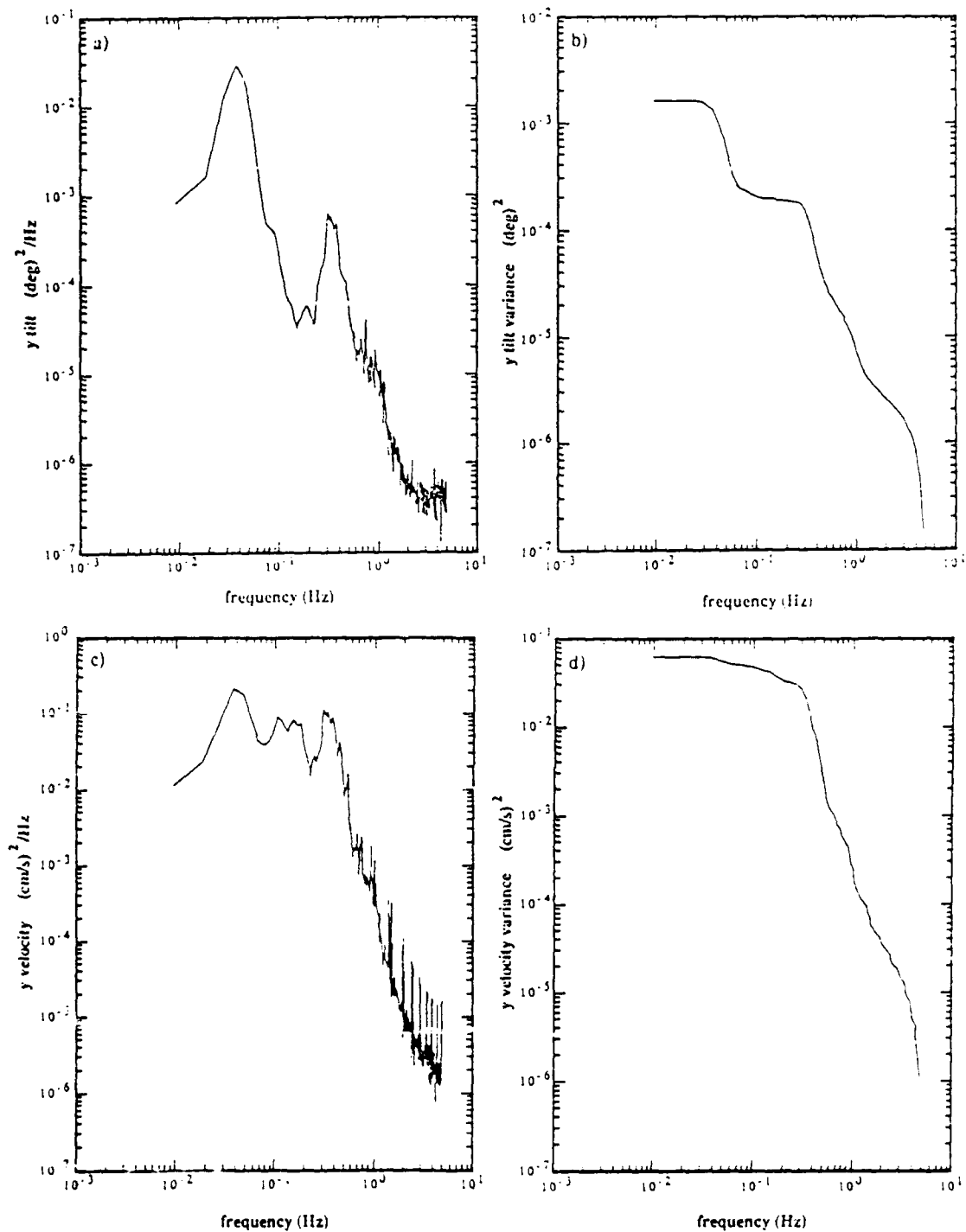
**Figure A6.** The same as Fig. A5, but now for the y (N-S direction) accelerometer. Rms velocity estimates are lower than the x axis, giving 0.25 cm/s for all frequencies, and 0.06 cm/s for frequencies above 1/2 Hz.
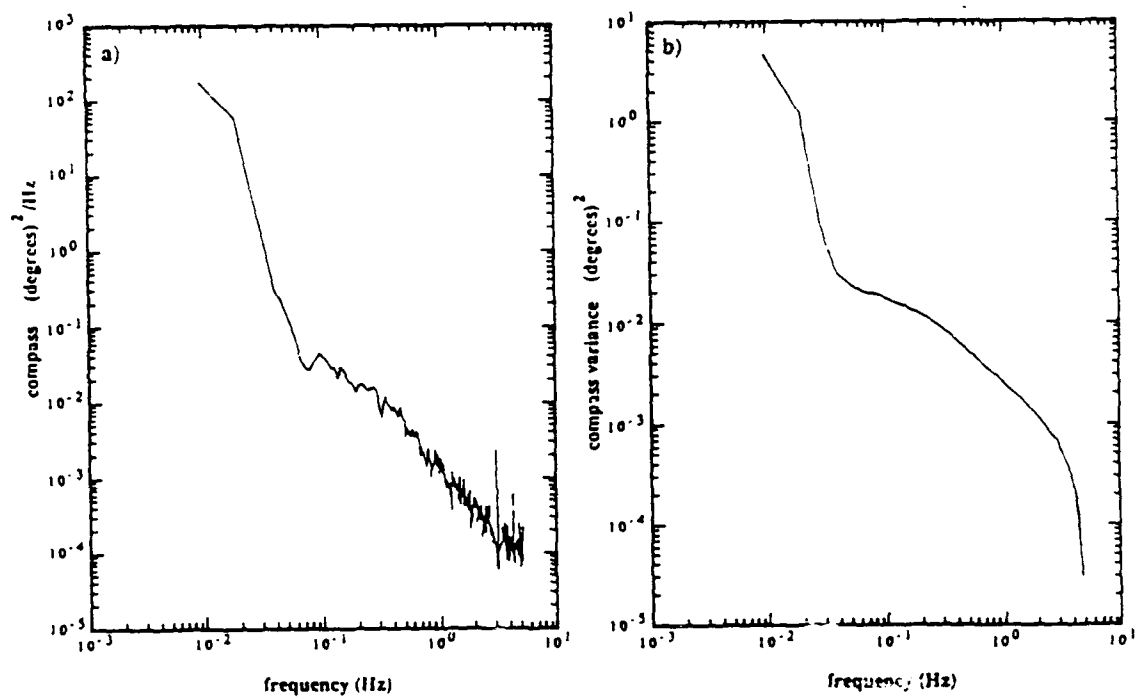
**Figure A7.** The compass spectrum is dominated by low-frequency motions, which correspond to ⁻7° rms over the thirty-eight minute time span.

**Figure A8.** Time series for all sensors is shown for the 7.5 day PATCHEX data run. Each point corresponds to a forty minute average, with 256 total points plotted. FLIP was two-point moored, and the major (10°) heading changes seen in e) reflect re-tensioning of the mooring lines.

## APPENDIX B

### The Effect of Scatterer Distribution on the

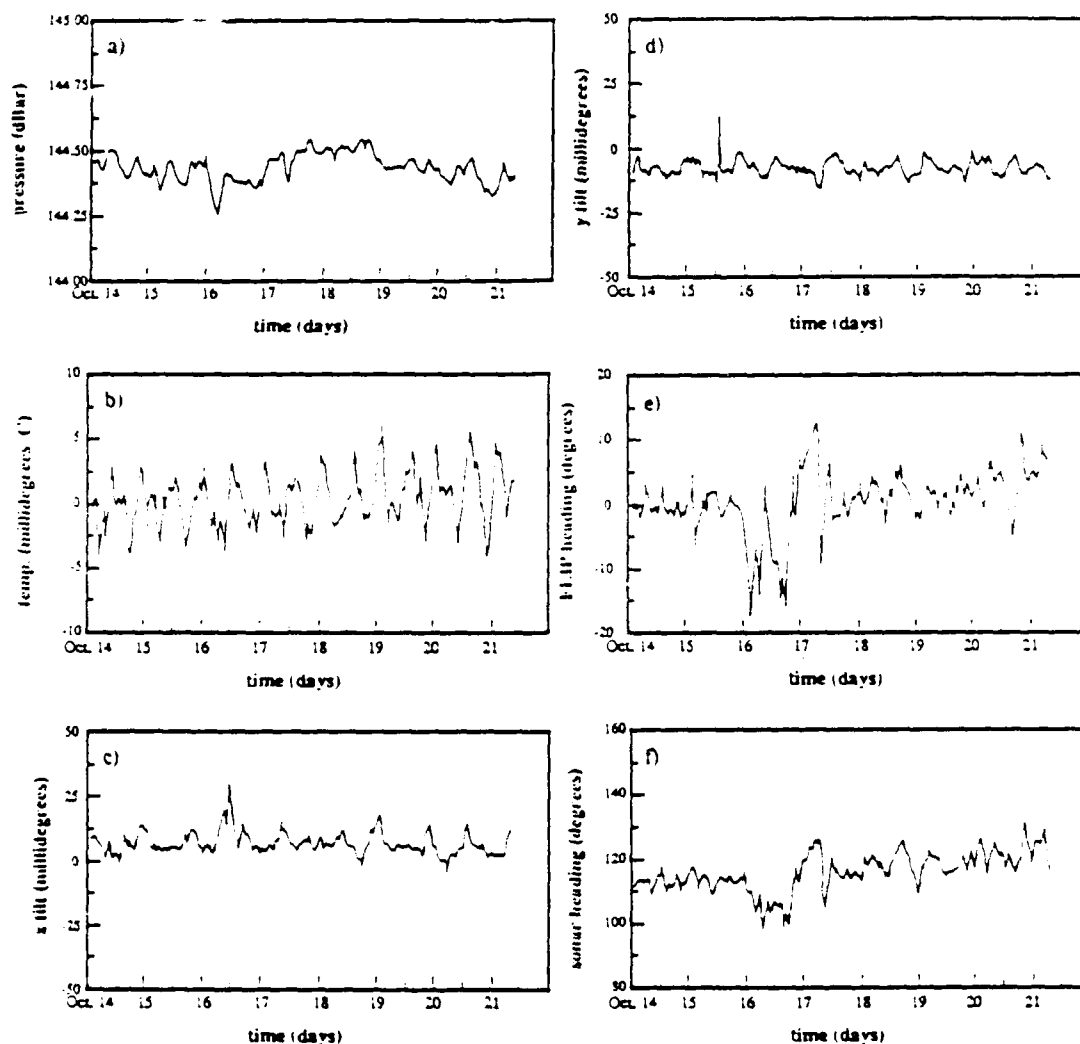### Precision of the Rummler Autocovariance Estimator

By heterodyning the return signal of (3.4), the carrier frequency can be removed, thus giving:

$$R(t) = \sum_{j=1}^{N}\sigma_b(a_j)e^{i\phi_j(t)} \equiv R_o(t)e^{i\theta(t)} \tag{B.1}$$

where N = number of individuals in the ensonified volume, with a size distribution such that the $j^{th}$ organism has radius $a_j$ and backscattering strength $\sigma_b(a_j)$. The phase information $\phi_j$ can be divided into three components:

$$\phi_j(t) = 2\kappa(x_{oj} + \bar{v}t + v_j'(t)) \tag{B.2}$$

where $\kappa$ is the wavenumber of the transmission frequency, $x_{oj}$ is the individual's initial location, $\bar{v}$ represents the mean velocity of all scatterers within the volume, and $v_j'(t)$ is the organism's time-dependent variance from $\bar{v}$. $\theta(t)$ represents a weighted average of all $\phi_j$, and is the phase available at the processing end to estimate the Doppler shift ($d\theta/dt$).

The Rummler autocovariance method estimates $d\theta/dt$ by computing the complex autocovariance

$$C(\Delta) = <R^*(t)R(t+\Delta)> \tag{B.3}$$

where $\Delta$ is the time lag (= sampling period for an incoherent sonar, or the transmission repetition period for a coherent sonar), and * denotes the conjugate. The velocity estimate is obtained from

$$\hat{v} = \frac{\lambda}{4\pi\Delta}\arg[ C(\Delta) ] \tag{B.4}$$

The effect of a finite number of scatterers on $\hat{v}$ can now be investigated. It is instructive to begin by assuming $\sigma_b(a_j)=1$, and $\bar{v}=v_j'=0$ for all j ( all scatterers are of equal size with no mean velocity or variance). The estimate of $C(\Delta)$ for a single time lag sample is:

$$C(\Delta) = \sum_{j=1}^{N}\sum_{k=1}^{N}e^{i2\kappa(x_{ok}-x_{oj})} \tag{B.5}$$

Note for each $e^{i2\kappa(x_{ok}-x_{oj})}$ there exists its complex conjugate pair $e^{i2\kappa(x_{oj}-x_{ok})}$. Thus the summation of (B.5) has no imaginary component, and $\hat{v} = 0$, as expected. The result is independent of N.

The next step is to assign each particle some normally distributed velocity. Let the volume-averaged velocity $\bar{v} = 0$, although each scatterer is moving at $v_j'$. This is even further simplified if it is assumed that $v_j' \neq v_j(t)$. That is, for the time involved in estimating $C(\Delta)$, each particle's velocity can be assumed to be constant. For instance, this would be appropriate for describing a steady-state shear flow through the ensonified volume. (B.3) then becomes:

$$C(\Delta) = \sum_{j=1}^{N} \sum_{k=1}^{N} e^{i2\kappa(x_{ok}-x_{oj})} e^{i2\kappa(v_k'(t+\Delta)-v_j't)} \tag{B.6}$$

$$= \sum_{j=1}^{N} e^{i2\kappa\Delta v_j'} + \sum_{j=1}^{N} \sum_{k \neq j}^{N} e^{i2\kappa(x_{ok}-x_{oj})} e^{i2\kappa(v_k'-v_j')t} e^{i2\kappa v_k'\Delta}$$

The first term (when $j=k$) is the self-correlated component of the signal. The first term consists of the sum of N normally distributed phases, and on average will be equal to $Ne^{-(\sigma\Delta)^2/2}$, where $\sigma^2 =$ velocity variance. The second term represents cross-products between scatterers. Due to the ($e^{i2\kappa v_k'\Delta}$) component of the second term, a complex conjugate pair no longer exists. The second term consists of a N(N-1) summation of randomly distributed phases, giving it an average amplitude of $(N(N-1))^{\frac{1}{2}}$ with some random phase orientation. The second term can be viewed as the noise component due to uncorrelated cross-product terms, while the first term is the desired signal. Therefore a signal-to-noise ratio can be defined as:

$$SNR = \frac{N}{N-1} e^{-(\sigma\Delta)^2} = \frac{N}{N-1} \text{ for } \sigma\Delta \ll 1. \tag{B.7}$$

The implication is that that it is marginally better to have fewer individuals present, with the limiting case being one scatterer giving perfect correlation. If $v_j'$ is time-varying, the second term obviously still stays uncorrelated, while the first term will be degraded in value even more. However, the N/(N-1) relation will still be correct.

The last step is to substitute the modeled values of N and $a_j$ from Chapter 3 into (B.1), assign each particle a random value of $x_{oj}$ and a normally distributed value of $v_j'$, and do computer simulations of $C(\Delta)$ and $\hat{v}$ Fig. 3.6b shows standard deviation estimates for varying values of total biomass present, which corresponds to varying N from 10 to 870. The number of 'significant scatterers' present and the percent return from the largest individual are given in Fig. 3.4. Estimated standard deviation values are within 30% of the expected value, and average 10% higher in value. No trend is apparent with varying N.

In summary, the Rummler autocovariance technique shows no strong preference to how many scatterers are present, and reasonably estimates the simulated variances input to the model.

# APPENDIX C

## Review of Linear Internal Wave Theory

### C.1    Equations of Motion

For an incompressible, inviscid fluid, the equations of motion are:

$$u_t + uu_x + vu_y + wu_z - fv = -\partial_x \bar{p}/\bar{\rho} \qquad \text{(C.1)}$$

$$v_t + uv_x + vv_y + wv_z + fu = -\partial_y \bar{p}/\bar{\rho}$$

$$w_t + uw_x + vw_y + ww_z + \rho g/\bar{\rho} = -\partial_z \bar{p}/\bar{\rho}$$

$$\rho_t + u\rho_x + v\rho_y + w\rho_z = w\bar{\rho}N^2/g$$

$$u_x + v_y + w_z = 0 .$$

Subscripts refer to differentiation ($u_t \equiv du/dt$), f = Coriolis force, N = Vaisala frequency, $\bar{\rho}$ = mean density, and $\rho$ and p are the density and pressure perturbations from their mean values. The equations are linearized by assuming that the products of the zeroth order terms are small compared to the terms themselves, and therefore negligible, reducing (C.1) to:

$$u_t - fv = -\partial_x \bar{p}/\bar{\rho} \qquad \text{(C.2)}$$

$$v_t + fu = -\partial_y \bar{p}/\bar{\rho}$$

$$w_t + \rho g/\bar{\rho} = -\partial_z \bar{p}/\bar{\rho}$$

$$\rho_t = w\bar{\rho}N^2/g$$

$$u_x + v_y + w_z = 0.$$

(C.2) has a solution of form:

$$\begin{bmatrix} u \\ v \\ w \\ \rho \\ p \end{bmatrix} = \text{Real} \left\{ \begin{bmatrix} u_o \\ v_o \\ w_o \\ \rho_o \\ \partial_o \end{bmatrix} e^{i(\alpha x + \beta y + mz - \omega t)} \right\} \qquad \text{(C.3)}$$

which satisfies the linear dispersion relation:

$$\frac{m}{k} = \pm \left[\frac{N^2-\omega^2}{\omega^2-f^2}\right]^{\frac{1}{2}}$$  (C.4)

where $\alpha^2+\beta^2 = k^2$. The relations between components are given by:

$$u_o = \frac{-mw_o}{k^2}(\alpha+i\beta f/\omega)$$  (C.5)

$$v_o = \frac{-mw_o}{k^2}(\beta-i\alpha f/\omega)$$

$$\rho_o = \frac{i\overline{\rho}N^2 w_o}{g\omega}$$

and

$$\partial_o = \frac{-\overline{\rho}(N^2-\omega^2)w_o}{m\omega}.$$

Let $\eta$ be defined as $d\eta/dt \equiv w$, such that $\eta = iw/\omega$, and $\eta_z = -mw/\omega$. The Vaisala frequency is related to the mean density gradient ($\equiv \overline{\rho_z}$) by $N^2 = g\overline{\rho_z}/\overline{\rho}$. Using (C.5), $\rho$ can also be expressed as:

$$\rho = \frac{iw}{\omega}\overline{\rho_z} = \eta\,\overline{\rho_z}.$$

Differentiating $\rho$ with respect to z gives:

$$\rho_z = \eta_z\,\overline{\rho_z} + \eta\,\overline{\rho_{zz}}$$

If a smooth density profile is assumed, such that $\overline{\rho_{zz}} << \overline{\rho_z}$, then $\eta_z$ is related to $\rho_z$ by:

$$\eta_z = \rho_z/\overline{\rho_z}.$$  (C.6)

This allows for an estimate of $\eta_z$ from density gradient perturbations at a fixed depth.

The expected ratio of (strain variance)/(shear variance) can now be calculated from (C.5) and (C.5). The ratio, for a single sinusoidal solution (normalized by $N^2$), is:

$$\Psi(\omega) \equiv \frac{N^2<\eta_z^*\eta_z>}{<u_z^*u_z + v_z^*v_z>} = \frac{(\omega^2-f^2)}{(\omega^2+f^2)}\frac{N^2}{(N^2-\omega^2)}$$  (C.7)

where * denotes complex conjugate, and <> signifies temporal averaging. $\Psi$ can be compared with measured values as a consistency test for linearity.

The linear solutions can be substituted back into (C.1) to estimate when nonlinearities are no longer negligible. This will occur when the advective terms

become the same order as the time derivative components:

$$u_t = uu_x + vu_y + wu_z \cdots \text{ etc. for rest of (C.1)} \tag{C.8}$$

For simplicity it will be assumed that:

$$u_o = v_o = (u_o^* u_o + v_o^* v_o)^{\frac{1}{2}} = \frac{mw_o}{k\omega}(\omega^2 + f^2)^{\frac{1}{2}} = mw_o/k \text{ for } \omega >> f. \tag{C.9}$$

(C.9) gives $uu_x \tilde{\ } uwm$, and $wu_z \tilde{\ } uwm$, such that the nonlinear contributions in (C.8) from both horizontal and vertical advection are of the same order. These terms will equal $u_t$ when:

$$u_t = u\omega = uwm \rightarrow 1 = mw/\omega = \eta_z. \tag{C.10}$$

The nonlinear terms are of the same magnitude as the linear components when $\eta_z \approx 1$.

## C.2    Eulerian vs. Semi-Lagrangian Strain

Fig. C.1 is a schematic of an isopycnal field passing by a fixed-depth sensor. It is assumed that the mean density profile is linear ($\overline{\rho}(z) = \rho_o - \overline{\rho_z}z$). Let $\rho(\varsigma)$ define an isopycnal with mean depth $\varsigma$, and density $\rho = \rho_o - \overline{\rho_z}\varsigma$. Its displacement at time $t$ from $\varsigma$ is defined here as $\eta(\varsigma,t)$. The depth of $\rho(\varsigma)$ is given by:

$$Z(\varsigma,t) = \varsigma + \eta(\varsigma,t) .$$

Two adjacent isopycnals have a mean separation equal to $\delta\varsigma$. At any instance in time they will be separated by $\delta z = \delta\varsigma + \delta\epsilon(t)$. The semi-Lagrangian strain is estimated from:

$$\eta_\varsigma(\varsigma) \equiv \frac{\eta(\varsigma+\delta\varsigma) - \eta(\varsigma)}{\delta\varsigma} = \frac{\delta\epsilon}{\delta\varsigma}. \tag{C.13}$$

The density gradient fluctuation from its mean value can be estimated at a fixed sensor from:

$$\rho_z = \frac{[\rho(\varsigma+\delta\varsigma) - \rho(\varsigma)] - [\overline{\rho}(z+\delta z/2) - \overline{\rho}(z-\delta z/2)]}{\delta z} \tag{C.14}$$

which reduces to:

$$\rho_z = \frac{-\overline{\rho_z}\delta\varsigma + \overline{\rho_z}\delta z}{\delta z} = \frac{\overline{\rho_z}\delta\epsilon}{\delta z}.$$

Using (C.6), the Eulerian strain can be written as:

$$\eta_z = \frac{\delta\epsilon}{\delta z} = \frac{\delta\epsilon}{\delta\varsigma+\delta\epsilon} \tag{C.15}$$

which, dividing the top and bottom by $\delta\varsigma$ gives

$$\eta_z = \frac{\eta_\varsigma}{1+\eta_\varsigma} \tag{C.16}$$

or equivalently,

$$\eta_\varsigma = \frac{\eta_z}{1-\eta_z}$$

For small strain, $\eta_z \approx \eta_\varsigma$ as expected. If isopycnals are closer together than average ($\delta\epsilon<0,\eta_\varsigma<0$), then $|\eta_z| > |\eta_\varsigma|$, while, if farther apart, then $\eta_\varsigma>0$, and $\eta_z<\eta_\varsigma$.

(C.13) and (C.14) are valid approximations of a derivative in the limit ($\delta\epsilon,\delta\varsigma)\rightarrow0$. This is equivalent to assuming that $\eta_{zz}<<\eta_z$ (gradients remain nearly constant across length scales $\delta\epsilon,\delta\varsigma$). This must also hold true for $\bar{\rho}(z)$, implying (C.16) is also inappropriate if a 'sheet and layer' density field is present.
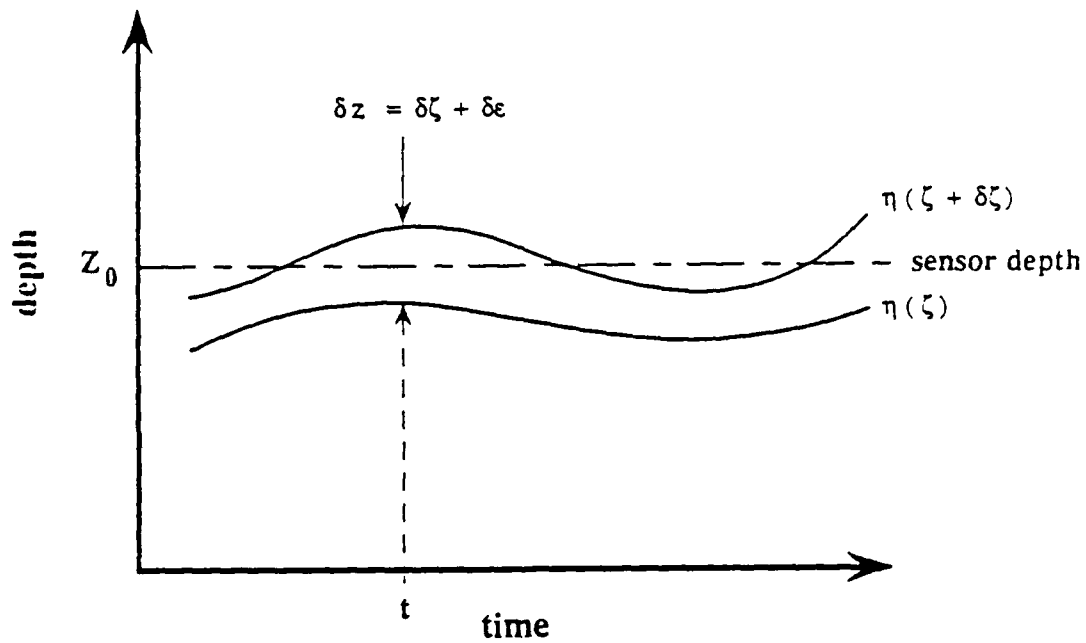
**Figure C1.** A schematic is shown of two isopycnals moving past a sensor at a fixed depth = $Z_o$. At time t, the isopycnals are separated by a distance $\delta z = \delta\epsilon(t) + \delta\varsigma$, where $\delta\varsigma$ is their mean separation. The estimation of the density gradient perturbation at $Z_o$ assumes that the mean density profile is linear : $\bar{\rho}(z) = -\overline{\rho_z}z + \rho_o$.

## APPENDIX D

## CTD Data Analysis

### D.1 Processing of the CTD Data

Vertical strain is computed from density gradient estimates, which in turn are based on conductivity (C), temperature (T), and pressure (P) measurements from the CTD instrument. C,T, and P are substituted into the equations of state (Fofonoff and Millard(83)) to estimate salinity (S), potential temperature (Θ), and potential density ($\rho_\theta$). Due to the conductivity and temperature sensors having different time response characteristics, and being spatially separated on the CTD package, the measured values of C and T have different frequency responses in both amplitude and phase. This mismatch will lead to salinity spiking and erroneous $\rho_\theta$ estimates.

The measured values of C and T are related to the true oceanic values through transfer functions, which depend upon the sensor response to the signal, and how this response is processed. The transfer function is comprised of both a gain and phase response. The 'true' and measured data are related in Fourier space by:

$$X_m(f) = X(f)G(f)e^{i\phi(f)}$$

where f = frequency, G = gain response, $\phi$ = phase response, and $X_m$ = measured Fourier transform.

Sea-Bird Electronics (SBE) CTD instruments were deployed during the PATCHEX cruise. The SBE unit averages measurements over 1/12 second periods, automatically causing temporal smoothing of the data. The temperature sensor deployed was model SBE 3-01/F, having a resolution of $5x10^{-4}$°C at the 12 Hz sample rate. It's transfer function can best be modeled as a double-pole filter (Pederson and Gregg(79)), which, combined with the temporal smoothing effect, gives a gain response function:

$$G_T(f) = \frac{\sin(\pi f/12)}{(\pi f/12)(1 + (2\pi f\tau_T)^2 )} \tag{D.1}$$

where f = frequency (Hz), and $\tau_T$ = time response ≈ 70 milliseconds.

For the conductivity sensor, Model SBE 4-01 was deployed, having a $5x10^{-4}$ mmho/cm resolution, with it's gain response approximated by a single-pole filter:

$$G_C(f) = \frac{\sin(\pi f/12)}{(\pi f/12)[1 + (2\pi f\tau_c)^2 ]^{1/2}} \cdot \tag{D.2}$$

The time response $\tau_c$ largely depends upon the flushing rate of the sensor. At the 3.8 m/s drop rate for the PATCHEX cruise, $\tau_c$ ≈ 110 ms.

If the instrument drop rate is assumed constant, then the frequency dependence of (D.1) and (D.2) can be transformed into vertical wavenumber $m$, where 1 cpm = 3.8 Hz. Fig. D1a demonstrates that, although $\tau_c > \tau_T$, the single-pole response has a gentler rolloff, so that the conductivity sensor responds better at higher frequencies (wavenumbers). It is also seen that for a 2 Hz (0.5 cpm) input signal, the measured temperature will be approximately half the true amplitude. In Fig. D1b,

the ratio $G_T/G_C$ is compared with the estimates based on the first fifty profiles of PATCHEX, showing that the above modeling of $G_T$ and $G_C$ appears to be appropriate.

Two approaches can be taken to correct C and T. The expected gain and phase response functions can be modeled (as done with the gain above) and directly applied to the measured data. However, any errors in the model (for instance, unaccounted-for time response characteristics of the electronics) will result in inaccurate estimates. Another approach is to take the cross-spectrum between conductivity and temperature, giving the measured relative phase and gain difference between C and T, and then applying this correction to the data set. This insures that C and T are correctly matched to each other. However, they will still be 'incorrect' in an absolute sense (high wavenumbers will be attenuated, and will have some associated phase lag). The cross-spectral method is best suited for removing salinity spiking, and is employed in the present study.

From the equations of state, the change of conductivity with depth can be approximated from:

$$dC/dz = \alpha dT/dz + \beta dS/dz \tag{D.3}$$

where $\alpha \approx 0.9$ (mmho/cm)/°C, and $\beta \approx 1$ (mmho/cm)/(ppt) for T = 10°C, and S = 34.7 ppt (part-per-thousand). (D.3) can be Fourier transformed in depth to give:

$$c(m) = \alpha t(m) + \beta s(m) . \tag{D.4}$$

The cross-spectral estimate with respect to temperature is:

$$<c^*t> = \alpha<t^*t> + \beta<s^*t> . \tag{D.5}$$

The phase response between conductivity and temperature is given by:

$$\theta(m) = \arctan\left[\frac{\mathrm{imag}(\beta<s^*t>)}{\alpha<t^*t> + \mathrm{real}(\beta<s^*t>)}\right] \tag{D.6}$$

where imag(), real() denote the imaginary and real components of (). Fourier transforms of the measured temperature and conductivity are related to the true values by:

$$t_m(m) = t(m)G_T(m)e^{i\psi(m)} \tag{D.7}$$

$$c_m(m) = c(m)G_C(m)e^{i\phi(m)} \tag{D.8... }$$

where $\psi, \phi$ are the phase response functions for the temperature and conductivity sensors respectively, and the subscript m denotes the measured quantity. The measured cross spectrum will now be:

$$<c_m^*t_m> = <c^*t>e^{i(\psi-\phi)}G_TG_C. \tag{D.8}$$

The needed phase information $(\psi-\phi)$ will only be recovered if $<c^*t>$ is real. This will occur if $<s^*t>$ is either very small compared to $<t^*t>$ and/or s and t are always in phase. Since the estimated value of s is dependent upon c, it is impossible to know

the true value of $<s't>$, making it difficult to assess the accuracy of the transfer function. The best recourse of action is to choose a low salinity-gradient region where few intrusions are present, such that variations in dC/dz are mainly due to dT/dz. For instance, for depths > 200 m, the PATCHEX salinity and temperature profiles are nearly linear (see Fig. D2), with S varying by (33.98-34.16) ppt, and T varying by 4.97-7.6°C. These values predict that $\alpha dT/dz \approx 10\beta dS/dz$.

During PATCHEX two CTD's profiled between 0-300 m and 260-560 m in depth once every three minutes. Data were recorded over a three week period (>10,000 profiles for each CTD). Estimates of $<c't>$ were computed for both CTD's at depths with low salinity gradient (>200 m). A subset of 2700 profiles interspersed throughout the entire cruise was used to compute $<c't>$. Gain and phase response functions between C and 1 were calculated, and then modeled with a cubic fit (c.f. Fig D3).

Conductivity and temperature gains can be matched by either attenuating C at high wavenumbers, or amplifying T. Since amplification also increases noise levels, it was decided to attenuate C, resulting in an underestimation of high wavenumber amplitude. To further remove noise at high wavenumbers, both T and C were low-pass filtered with the filter shown in Fig. D4, effectively removing signal and noise above 0.5 cpm. Fig. D3 shows that at 0.5 cpm the gain correction is $\approx 0.9$, and phase correction is $\approx 5°$, thus no large corrections have been made in amplitude or phase.

The data were processed in the following manner: Average C and T values were computed between 20-40 m depth (in the mixed layer). dC/dz, and dT/dz were Fourier transformed ($\equiv c(m)$, $t(m)$), the gain and phase matching were applied to $c(m)$, and both $c(m)$ and $t(m)$ were low-pass filtered before being inverse Fourier transformed. C and T profiles were re-integrated, with the average C and T values between 20-40 m depth matched to the pre-processed values. Salinity, $\Theta$, and $\rho_\theta$ were then computed (with reference depth = 0 m ). A sample of pre- and post-processed salinity profiles is given in Fig. D5.

## D.2    Error Analysis

The low-pass filtering of Fig. D4 removes instrument noise between the Nyquist wavenumber ( Nyquist frequency = 6 Hz = 1.58 cpm) and 0.5 cpm, lowering the noise variance to $\approx 25$ % of it's original value (increasing the precision by two). The dependency of $\rho_\theta$ on C and T can be approximated from the equations of state ( using the same mean S and T as in (D.4)):

$$\Delta\rho_\theta(gm/cm^3) = 0.72 \times 10^{-3}\Delta T(°C) + 0.78 \times 10^{-3}\Delta C(mmho/cm). \tag{D.9}$$

The expected precision of $\rho_\theta$ is $\approx 2^{1/2}(.8 \times 10^{-3} * 2.5 \times 10^{-4}) = 3 \times 10^{-7}$ gm/cm³. This assumes that C and T have been properly phase-matched.

The strain can be estimated from (c.f. (C.6)):

$$\eta_z = \frac{g}{\bar{\rho}N^2}d\rho_\theta/dz \tag{D.10}$$

where N = Vaisala frequency, and $\bar{\rho}$ = mean density. The precision of $\eta_z$ ranges from 0.16 at N = 2.4 cph (~560 m depth) to 0.01 at N = 10 cph for a vertical wavenumber $m$ = 0.5 cpm (dz = 1 m). Estimates of $\eta_z$ have also been averaged over twenty-one

minute periods (seven profiles), which increases the precision to 0.06-0.004 at $N=2.4$-10 cph for $m = 0.5$ cpm.

If noise appears white in wavenumber for $\rho_\theta$, corresponding to a +2 slope for $\eta_z$, then an input of pure noise which has been low-pass filtered using Fig. D4 will have the spectral response as shown in Fig. D6. This is compared with the measured vertical wavenumber spectrum, which appears well above the noise.

Effects of pressure fluctuations have so far been ignored. Fluctuations cause an inaccurate measure of $\Delta z$, adding another source of error to $\eta_z$. More importantly, if fluctuations are truly due to a variable instrument drop rate (versus water turbulence at the sensor), then the assumption that the sensor's frequency response is directly related to wavenumber is incorrect, and the phase and amplitude matching in wavenumber is inappropriate. Fig. D7 shows a typical profile drop rate, along with it's associated wavenumber spectrum. Pressure fluctuations are comprised of two wavenumber regions. A peak is seen at low wavenumber, which corresponds to the surface wave frequency band. Due to the signal's lack of attenuation with depth, it is assumed that these fluctuations are due to the response of the boom to surface waves acting on FLIP, causing 5-10% variation in drop rate over 20-50 m vertical scales. This corresponds to 5-10% distortion between wavenumber and frequency. Due to the smoothness of the gain and phase response functions, this is not viewed as a significant problem.

dP/dz fluctuations increase at high wavenumbers (frequencies), presumably due to instrument-induced water turbulence at the pressure sensor. These fluctuations have been low-pass filtered below 0.2 cpm, resulting in the smooth profile of Fig. D7a. To minimize error propagation, all pressure profiles were low-pass filtered before any calculations involving P were performed. $\eta_z$ is calculated at $\Delta z = 0.32$ m intervals. Since $\Delta P$ fluctuations have been low-passed at 0.2 cpm, errors in estimating $\Delta z$ are minimal.

If these high-wavenumber pressure fluctuations are a measure of turbulence at the sensor, it is only fair to assume that both C and T are affected in a similar manner. The +1 slope seen at high wavenumbers in the dP/dz spectrum (Fig. D7b) implies that the turbulent signal appears with a -1 slope in P (as compared with 0 slope for white noise). Since the dP/dz spectrum does not change to a +2 slope at the highest wavenumbers, this suggests that the instrument-induced turbulence dominates the electronics noise. Such a turbulent-noise source (based on the +1 slope) is modeled in Fig. D6. It is displayed with an arbitrary energy level, since no direct measurement exists for instrument-induced turbulent noise for C and T. The flattening of the spectrum at high wavenumbers may be due to the instrument-induced noise level, indicating low signal-to-noise levels.
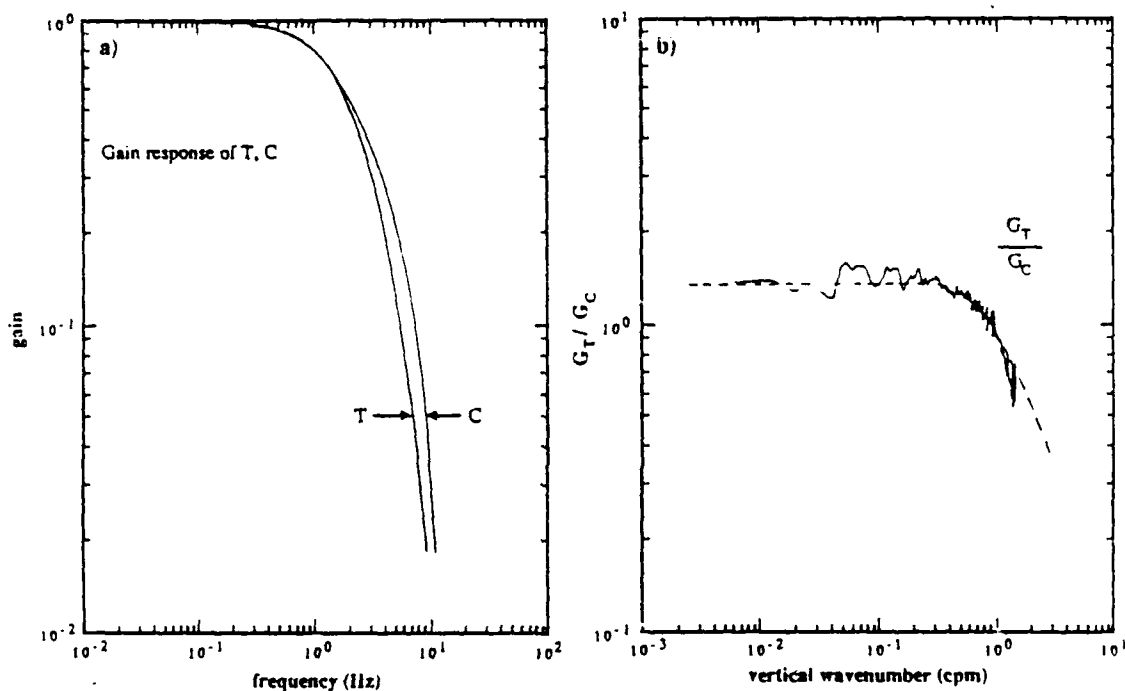
**Figure D1.** a) Temperature (T) exhibits a double-pole filter gain response with a time constant ≈ 70 ms, while conductivity (C) has a single-pole response with a time constant ≈ 110 ms. b) The ratio of the temperature gain/conductivity gain from a) is compared with the average from 50 measured profiles from the CTD.
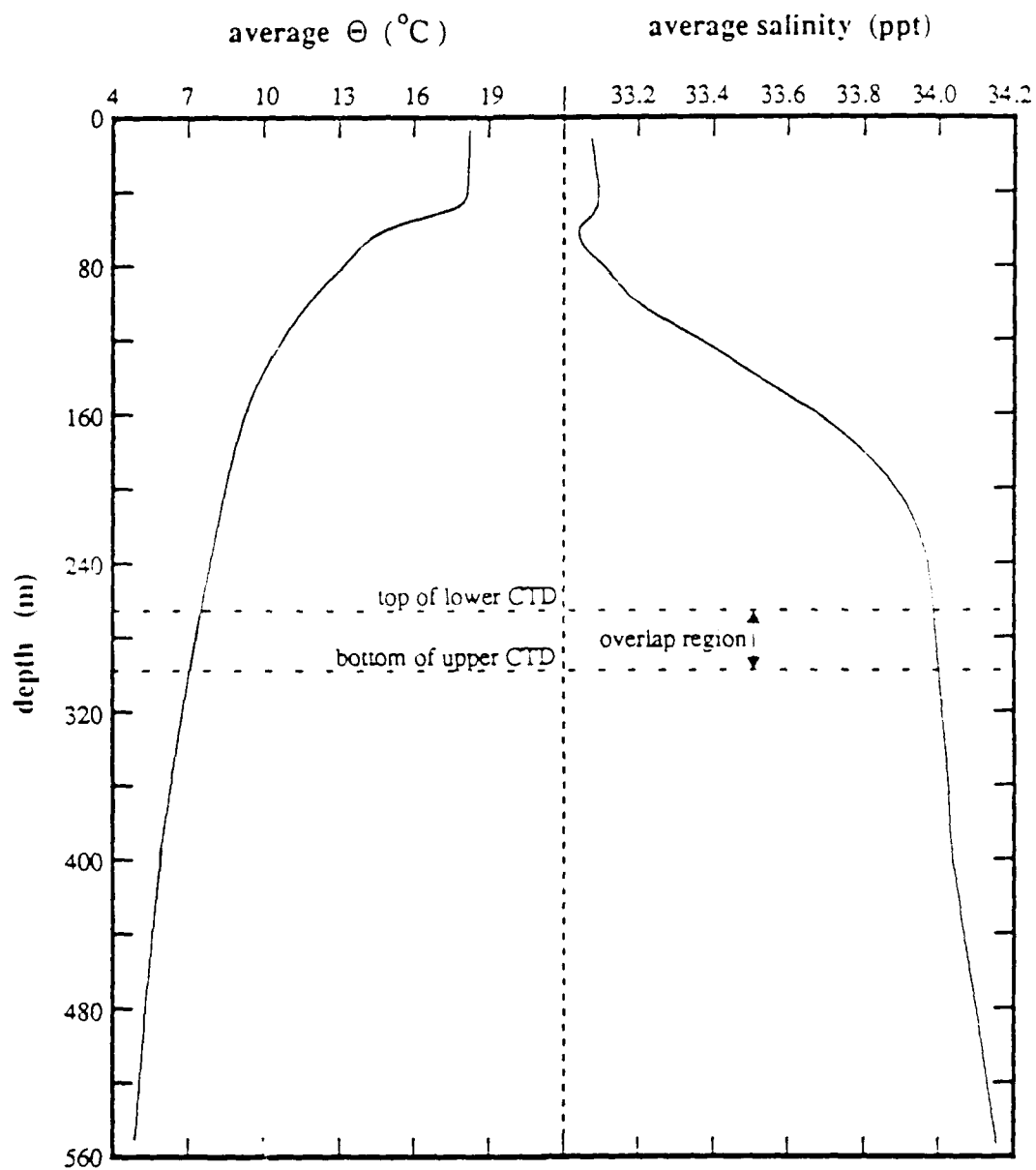
**Figure D2.** The three-week average salinity and potential temperature profiles for the PATCHEX cruise are shown for the upper and lower CTD's. The low salinity gradient below 200 m allows gain and phase response functions to be estimated between the conductivity and temperature sensors.
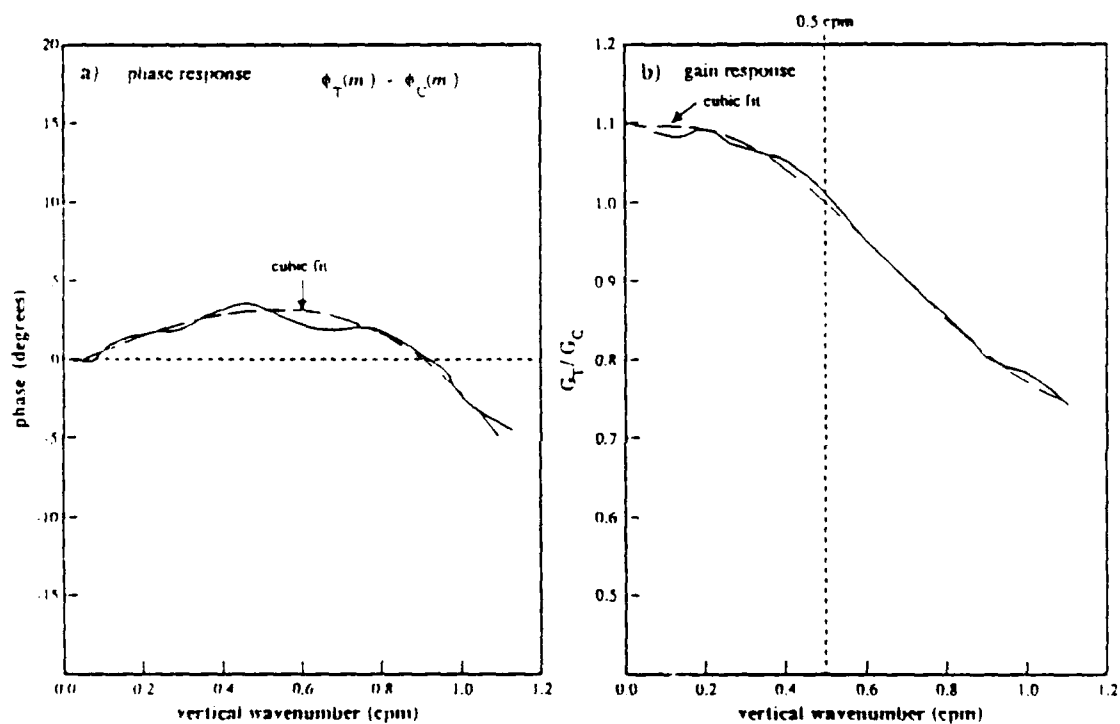
**Figure D3.** The a) phase and b) gain response functions are shown for the upper CTD between the temperature and conductivity gradients. The temperature and conductivity sensors have different gain at low wavenumbers due to the sensitivity of each sensor. The gain response correction is therefore renormalized such that at low wavenumbers the gain function = 1.
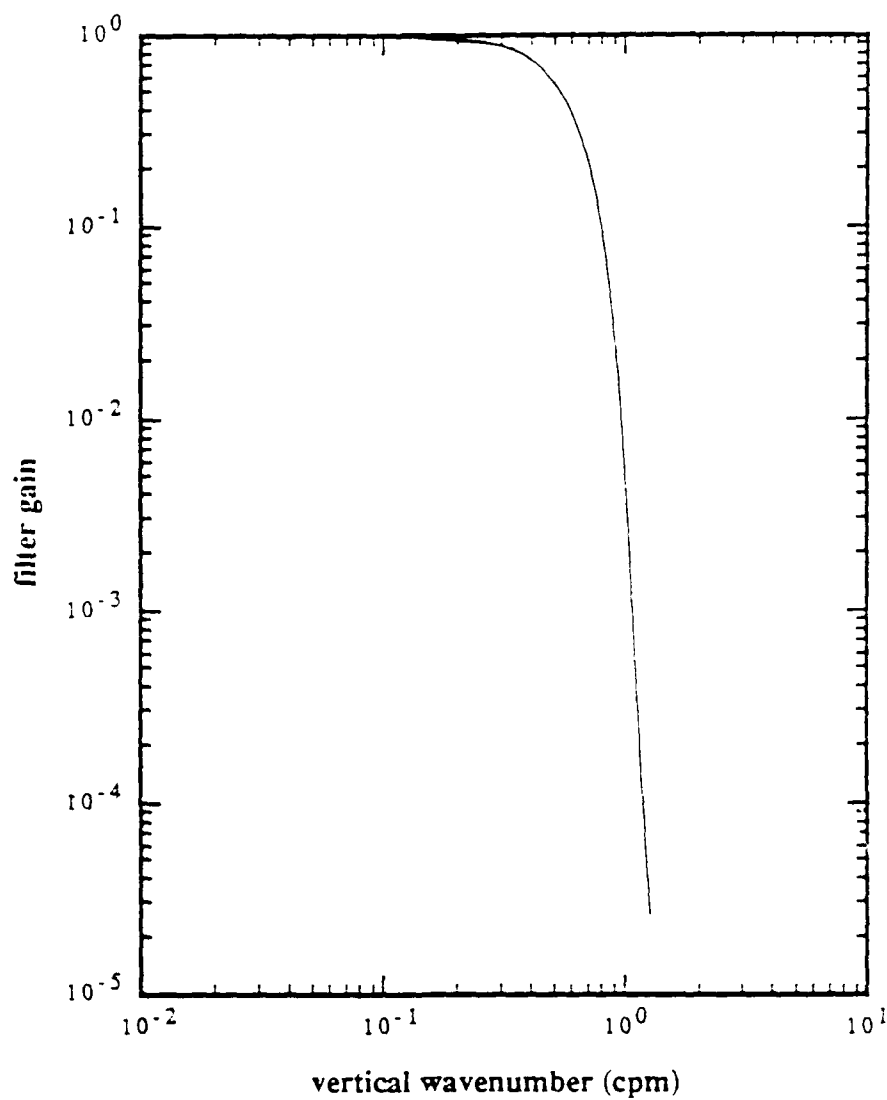
**Figure D4.** The low-pass filter applied to both conductivity and temperature is equal to

$$G(m) = \frac{1}{(1+(m/m_1)^4)[1+(m/m_2)^8]^4}$$

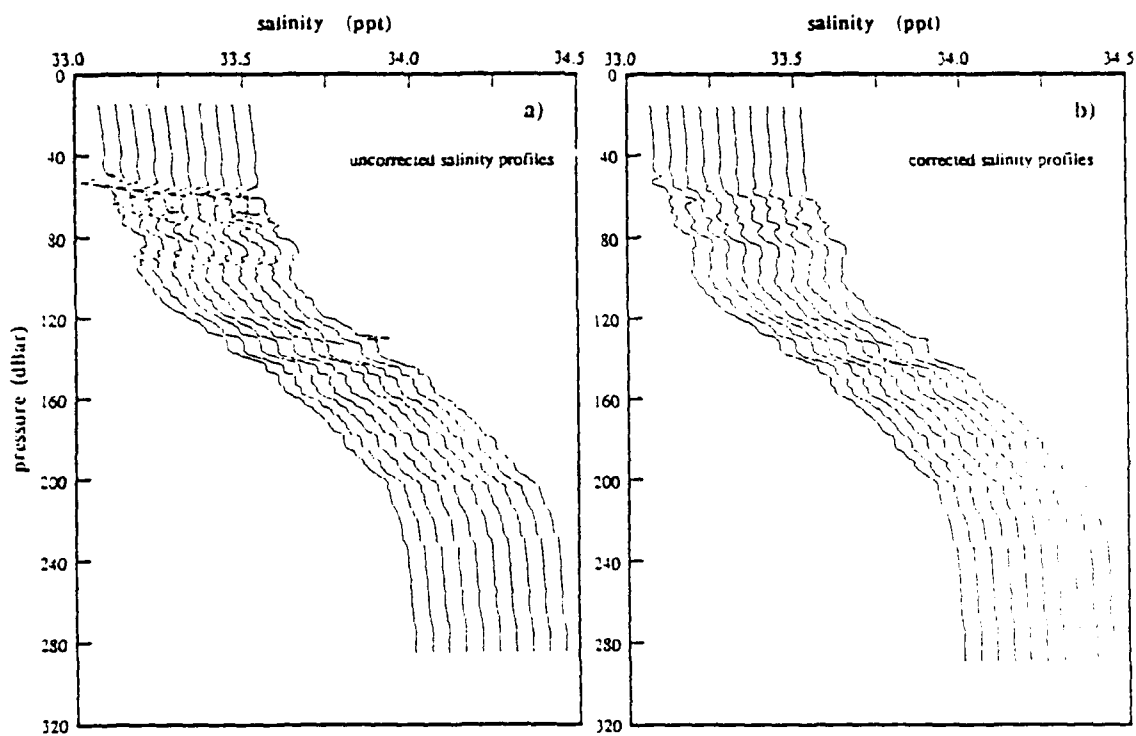with $m_1 = 0.55$ cpm, and $m_2 = 1$ cpm.

**Figure D5.** a) Ten salinity profiles (each separated by 3 minutes in time) are calculated from C and T as measured from the CTD. b) The same ten profiles are computed using C and T which have been gain and phase-matched, plus low-pass filtered.
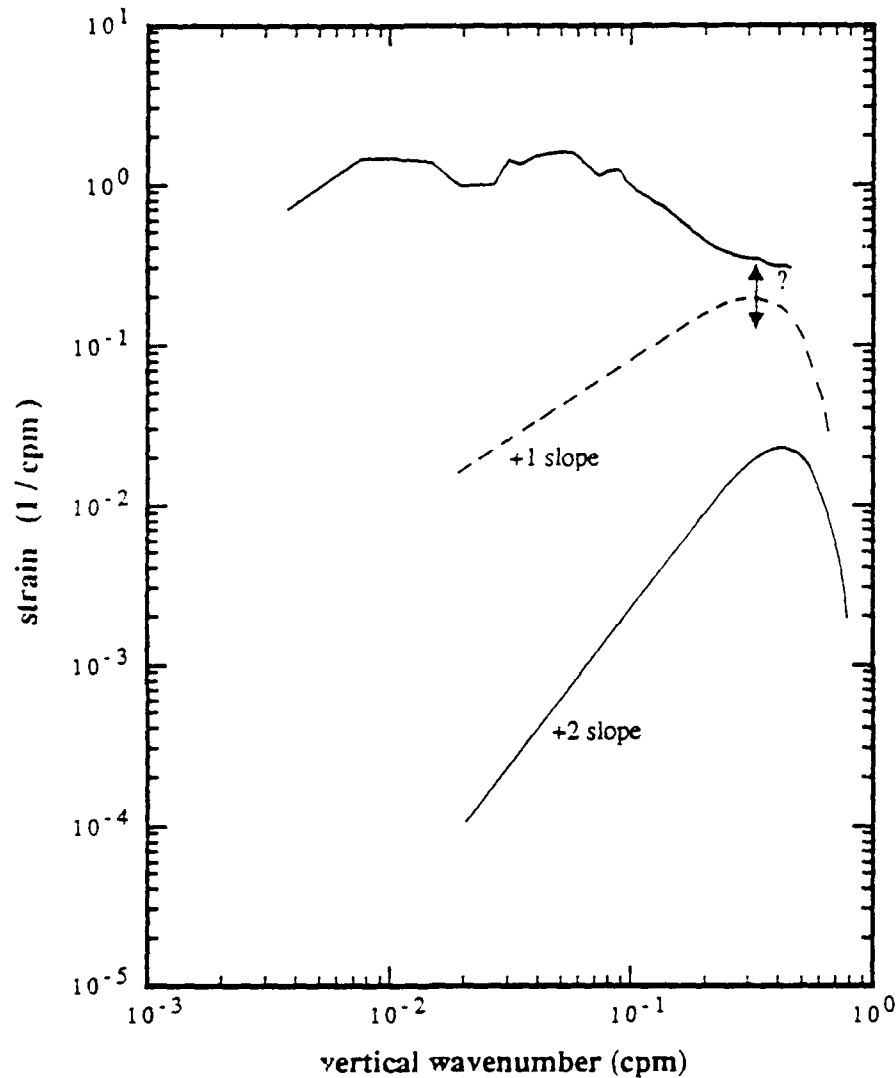
**Figure D6.** The measured strain spectrum is compared with the estimated white noise spectrum (processed through Fig. D4's filter, showing the +2 slope at low wavenumber). Also shown is the instrument-induced water turbulence spectrum, as seen from the pressure sensor data (Fig. D7), with a +1 slope. The energy level of the turbulence noise is not known, such that it's vertical position cannot be estimated. However, the flattening of the measured spectrum at high wavenumbers could be due the turbulence noise becoming significant.
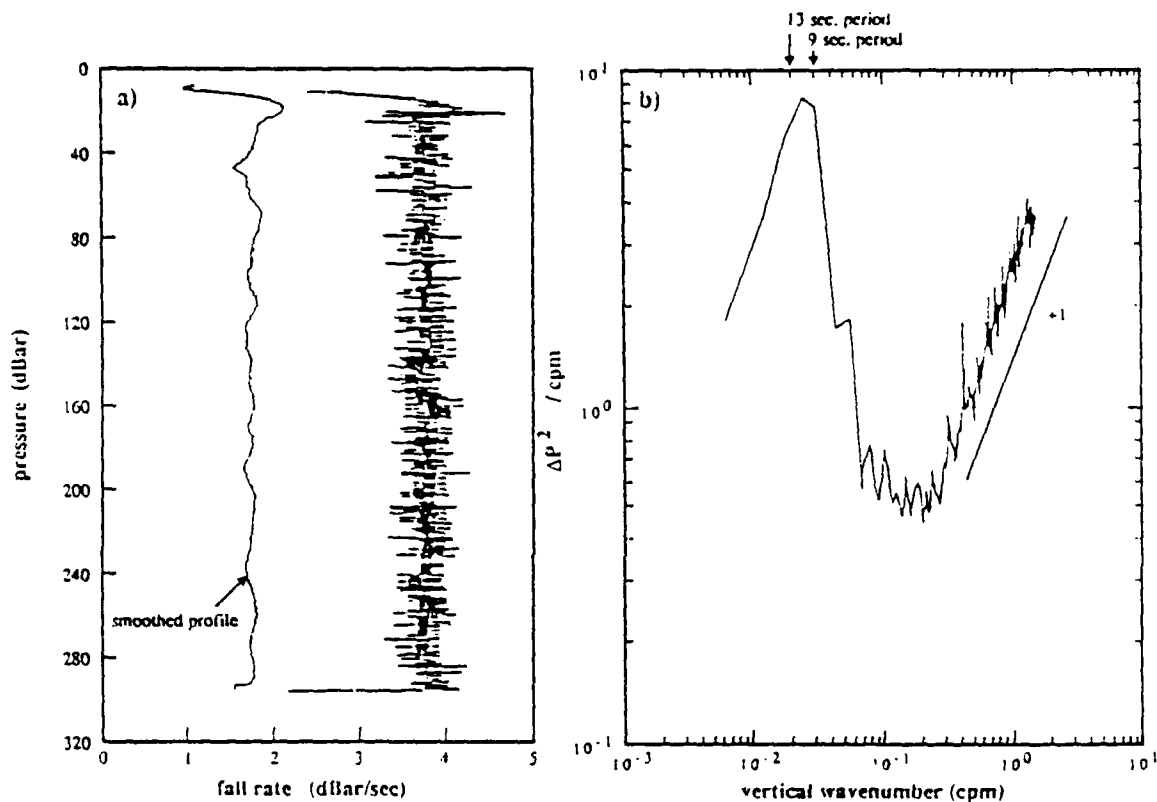
**Figure D7.** a) Measured instrument drop rate from one CTD profile is estimated from the pressure sensor data. Offset by 2 decibars/sec is the same profile with a 17 point (≈ 5 m in depth) running-mean-filter applied. b) The spectrum of the first-differenced pressure signal (averaged over 100 profiles) shows a low wavenumber component which corresponds to the surface wave frequency band, plus a high-wavenumber +1 slope region, thought to be due to instrument-induced water turbulence.

# References

Anderson, V. C., 1950: Sound scattering from a fluid sphere. *J. Acoust. Soc. Am.*, **22**, 426-431.

Broutman, D., 1986: On internal wave caustics. *J. Phys. Oceanogr.*, **16**, 1625-1635.

Broutman, D. and W. R. Young, 1986: On the interaction of small-scale oceanic internal waves with near-inertial waves. *J. Fluid Mech.*, **166**, 341-358.

Brumley, B. H., P. R. Heuchling, R. L. Koehler, and E. A. Terray, 1987: Coded pulse-coherent Doppler sonar. *Proc. OCEANS '87*, Halifax, Canada, 89-92.

Cabrera, R., K. Deines, B. Brumley, and E. Terray, 1987: Development of a practical coherent acoustic Doppler current profiler. *Proc. OCEANS '87*, Halifax, Canada, 93-97.

Cox, C. S. and C. L. Johnson, 1979: Inter-relations of micro processes, internal waves and large scale ocean features. *unpublished manuscript.*

Desaubies, Y. and M. Gregg, 1981: Reversible and irreversible finestructure. *J. Phys. Oceanogr.*, **11**, 541-556.

Desaubies, Y. and W. K. Smith, 1982: Statistics of Richardson number and instability in oceanic internal waves. *J. Phys. Oceanogr.*, **12**, 1245-1259.

Duda, T. F., 1986: Observations of horizontal flow, vertical shear and microstructure in the upper ocean. *Ph.D. dissertaion*, Univ. of California, San Diego.

Evans, D. L., 1982: Observations of small-scale shear and density structure in the ocean. *Deep-Sea Res.*, **29**, 581-595.

Fofonoff, N. P., 1969: Spectral characteristics of internal waves in the oceans. *Deep-Sea Res.*, **16(Suppl.)**, 58-71.

Fofonoff, N.P. and R. C. Millard, Jr., 1983: Algorithms for computation of fundamental properties of seawater. *UNESCO Tech. Pap. in Mar. Sci.*, No. 44, 53 pp..

Gargett, A. E., P. J. Hendricks, T. B. Sanford, T. R. Osborn, and A. J. Williams, 1981: A composite spectrum of vertical shear in the upper ocean. *J. Phys. Oceanogr.*, **11**, 1258-1271.

Garrett, C. J. R. and W. H. Munk, 1971: Internal wave spectra in the presence of fine-structure. *J. Phys. Oceanogr.*, **1**, 196-202.

Garrett, C. J. R. and W. H. Munk, 1972: Space-time scales of internal waves. *Geophys. Fluid Dyn.*, **2**, 225-264.

Greenblatt, P., 1980: Observation of zooplankton patchiness using a high frequency sonar and a multiple sample plankton net. *Ph.D. dissertation*, Univ. of California,

San Diego.

Gregg, M. C., 1977: Variations in the intensity of small-scale mixing in the main thermocline. *J. Phys. Oceanogr.*, **7**, 436-454.

Gregg, M. C., E. A. D'Asaro, T. J. Shay, and N. Larson, 1986: Observations of persistent mixing and near-inertial internal waves. *J. Phys. Oceanogr.*, **16**, 856-885.

Hansen, D. S., 1985: Asymptotic performance of a pulse-to-pulse incoherent Doppler sonar in an oceanic environment. *IEEE J. Ocean. Eng.*, **OE-10**, No. 2, 144-158.

Holloway, G., 1980: Oceanic internal waves are not weak waves. *J. Phys. Oceanogr.*, **10**, 906-914.

Johnson, R. K., 1977: Sound scattering from a fluid sphere revisited. *J. Acoust. Soc. Am.*, **61**, No. 2, 375-377.

Lhermitte, R., 1981: Observations of water flow with high resolution Doppler sonar. *Geophys. Res. Lett.*, **8**, No. 2, 155-158.

Lhermitte, R., 1983: Doppler sonar observation of tidal flow. *J. Geophys. Res.*, **88**, No. C1, 725-742.

Lhermitte, R. and R. Serafin, 1984: Pulse-to-pulse coherent Doppler sonar signal processing techniques. *J. Atmos. Ocean. Technol.*, **1**, No. 4, 293-308.

McComas, C. H. and P. Muller, 1981: The dynamic balance of internal waves. *J. Phys. Oceanogr.*, **11**, 970-987.

McKean, R. S., 1974: Interpretation of internal wave measurements in the presence of finestructure. *J. Phys. Oceanogr.*, **4**, 200-213.

Miller, K. S. and M. M. Rochwarger, 1970: On estimating spectral moments in the presence of colored noise. *IEEE Trans. Inf. Theory*, **IT-16**, No. 3, 303-309.

Miller, K. S. and M. M. Rochwarger, 1972: A covariance approach to spectral moment estimation. *IEEE Trans. Inf. Theory*, **IT-18**, No. 5, 588-596.

Muller, P., D. J. Olbers, and J. Willebrand, 1978: The IWEX spectrum. *J. Geophys. Res.*, **83**, No. C1, 479-500.

Muller, P., R. Lien, and R. Williams, 1988: Estimates of potential vorticity at small scales in the ocean. *J. Phys. Oceanogr.*, **18**, 401-416.

Munk, W. H., 1981: Internal waves and small scale processes. *Evolution of Physical Oceanography*, B. Warren and C. Wunsch, Ed., The MIT Press, 264-291.

Omori, M. and T. Ikeda, 1984: *Methods in Marine Zooplankton Ecology.* Wiley, New York,

Phillips, O. M., 1971: On spectra measured in an undulating layered medium. *J. Phys. Oceanogr.*, **1**, No. 1, 1-6.

Pinkel, R., 1979: Observations of a strongly nonlinear internal motion in the open sea using a range-gated Doppler sonar. *J. Phys. Oceanogr.*, **9**, No. 4, 675-686.

Pinkel, R., 1980: Acoustic Doppler techniques. *Air-Sea Interaction*, F. Dobson, L. Hasse, R. Davis, Ed., Plenum Press, New York, 171-199.

Pinkel, R., 1985: A wavenumber-frequency spectrum of upper ocean shear. *J. Phys. Oceanogr.*, **15**, No. 11, 1453-1469.

Pinkel, R., A. Plueddemann, and R. Williams, 1987: Internal wave observations from FLIP in MILDEX. *J. Phys. Oceanogr.*, **17**, No. 10, 1737-1757.

Platt, T., 1985: Structure of the marine ecosystem: Its allometric basis. *Ecosystem theory for biological oceanography*, Can. Bull. Fish Aquat. Sci., Ottawa, Canada, 55-64.

Plueddemann, A. J., 1987: Observations of the upper ocean using a multi-beam Doppler sonar. *Ph.D. dissertation*, Univ. of California, San Diego.

Rodriguez, J. and M. M. Mullin, 1986a: Relation between biomass and body weight of plankton in a steady state oceanic ecosystem. *Limnol. Oceanogr.*, **31**, 361-370.

Rodriguez, J. and M. M. Mullin, 1986b: Diel and interannual variation of size-distribution of oceanic zooplanktonic biomass. *Ecology*, **67**, 215-222.

Rudnick, P., 1964: FLIP: An oceanographic buoy. *Science*, **146**, 1268-1273.

Rummler, W. D., 1968: Introduction of a new estimator for velocity spectral parameters. *Tech. Memo MM-68-4121-5*, Bell Telephone Laboratories, Whippany, N.J..

Sirmans, D. and B. Bumgarner, 1975: Numerical comparison of five mean frequency estimators. *J. Appl. Meteor.*, **14**, 991-1003.

Theriault, K.B., 1986: Incoherent multibeam Doppler current profiler performance: Part I - Estimate variance. *IEEE J. Ocean. Eng.*, **OE-11**, No. 11, 7-15.

Toole, J. M. and S. P. Hayes, 1984: Finescale velocity-density characteristics and Richardson number statistics of the Eastern Equatorial Pacific. *J. Phys. Oceanogr.*, **14**, 712-726.

Urick, R. J., 1983: *Principles of Underwater Sound*, McGraw-Hill, New York, 423 pp..

Wiebe, P. H., S. Boyd, and J. L. Cox, 1975: Relationships between zooplankton displacement volume, wet volume, dry weight and carbon. *Fish. Bull*, **73**, 777-786.

Williams, R. G., 1985: The internal tide off Southern California. *Ph.D. thesis*, Univ. of California, San Diego.

Woodward, W. E. and G. F. Appell, 1986: Current velocity measurements using acoustic Doppler backscatter: A review. *IEEE J. Ocean. Eng.*, **OE-11**, No. 1, 3-6.